KU LEUVEN

FACULTY OF SCIENCES

Exploring the Efficiency of RaF^- Production at ISOLDE

Kathryn HOLLOWAY

Supervisor: Prof. Gerda Neyens
KU Leuven

Cosupervisor: Prof. Jérôme Loreau
KU Leuven

Mentors: Justus Berbalk
KU Leuven and CERN

Carlos Mario Fajardo Zambrano
KU Leuven and CERN

Master thesis submitted in fulfillment of the requirements for the degree in Master of Science in Chemistry

Academic year 2024-2025

Acknowledgments

A large team was always behind me for this project, and this thesis would not be complete without thanking them. I would like express my gratitude to Prof. Gerda Neyens for giving me such a unique project I could only dream of for my thesis and for the support throughout. Prof. Jérôme Loreau provided immense knowledge on how to approach what seemed to be a daunting task. He was always bridging the gap between the two departments, and such a collaboration would not be possible without him.

To my mentors Justus and Carlos, thank you so much for always being on call for me. Even when I first expressed interest over a year ago, Justus was eager to answer any of my questions and to help. You both always found a time despite your busy schedules, from last-minute meetings to quick responses to data after hours, none of this would be possible without you both, and I am excited to see where your bright futures take you.

This thesis would not have been possible without the endless time spent on preparation and beamline that led to a successful production of RaF^{-}. From theory to shifts during the run, the CRIS collaboration deserves all the praise. Thank you for letting me be a small part of it. Thank you to all the members of the Nuclear Moments group at IKS. The weekly meetings were very beneficial and helped keep me on track during this process. I want to acknowledge Bram for quickly helping me adjust the code for this experimental setup.

As this concludes my time at KU Leuven, I wanted to express my gratitude to all of my peers, professors, and people I have met here. Thank you so much for making Belgium home for these past two years.

The most important thanks goes to my friends and family. You all supported me so much on this journey, always believing in me. Thank you to my mom and dad for always bringing me peace, and to Lili and Nick for visiting me on several occasions, and joining me on countless trips to the frituur.

Summary

This thesis explores the efficiency of producing RaF^- anions from a beam of RaF^+ cations through double charge exchange with sodium vapor. RaF is of particular interest in time-reversal and parity-violating physics, as it has been predicted to be sensitive to parity-violating moments such as the nuclear or electronic Electric Dipole Moment (EDM). Its sensitivity is due to the radium nucleus having a high atomic number, as well as the fact that some specific isotopes of Ra have a static octupole (pear-shaped) deformation. The production of RaF^- is proposed as a promising alternative to improve the trapping efficiency of RaF for high precision experiments. During the experiment at ISOLDE/CERN performed in December 2024, a beam of mass-selected RaF^+ ions was delivered to the Collinear Resonance Ionization Spectroscopy (CRIS) setup and directed through a sodium vapor charge exchange cell, where sequential electron exchange reactions were expected to form neutral RaF and then, RaF^-. In this thesis, several approaches were employed to estimate the cross section for this reaction and evaluate the efficiency of RaF^- production under varying charge exchange cell conditions in order to compare to experimental results. The overall objective of this thesis is to find out how the parameters within the charge exchange cell influence the probability of charge exchange to create RaF^- starting from the RaF^+ beam.

Contributions

Prof. Jérôme Loreau introduced me to the locked dipole model and suggested I explore ways to handle theta. I did independent research to find the ADO, AADO, and temperature-dependent ADO models. Prof. Jérôme Loreau had the idea to use CaF as a baseline for ab initio calculations. He also suggested using the rubidium dissociation model as a starting point for the ion-pair formation.

Both Prof. Jérôme Loreau and Justus Berbalk originally suggested obtaining RaF polarizability ranges based on trends from other alkaline earth monofluorides. The idea to implement the STREUSEL technique along with the correlation with polarizability was that of my own. I came up with the idea to interpolate the dipole moment for RaF^+ using RaF, CaF, and CaF^+ dipole moments.

All experimental data was analyzed by me with the assistance of my supervisors, Justus Berbalk and Carlos Fajardo. The codes to analyze the data for CRIS setups was written by Ph.D. student Bram van den Borne and are accessible to everyone in IKS. Prof. Agi Koszorús from IKS provided the paper that introduced me to Massey's adiabatic criterion. I participated in the experiment (ISOLDE at CERN) in December 2024 under the guidance of Justus Berbalk and Carlos Fajardo. The campaign to produce RaF^- is part of a larger project with collective contributions from the CRIS and ISOLDE collaborations.

List of Figures

List of Tables

Contents

Chapter 1

Introduction

The Standard Model (SM) of particle physics has achieved remarkable success in describing known fundamental particles and interactions. However, it leaves unresolved key questions, such as the matter–antimatter asymmetry of the universe, which cannot be explained with the currently observed violations of Charge (C) and Parity (P) in the strong and weak fundamental interactions (active on the nuclear length scale). Extensions beyond the Standard Model (BSM) propose new sources of charge and parity (CP) violation that can be probed through precision measurements on atoms and molecules at low energies. It is of interest to search for new sources of CP violation, as this could help resolve the strong CP problem, the puzzling conservation of CP symmetry in the strong interaction [1]. While CP violation has been observed in weak interactions, no CP-violating effects have been detected in strong interactions, despite being allowed theoretically. CP-violating effects can be probed through precision measurements of permanent electric dipole moments (EDMs), since a CP-violating term would induce a permanent EDM in particles. Therefore, the observation of a measurable EDM could signal new physics beyond the SM, which predicts values several orders of magnitude below current experimental sensitivity [2]. The current best experimental bound is $|d_e| < 4.1 \times 10^{-30}\ e \cdot \mathrm{cm}$ whereas the SM prediction is $|d_e|_{\mathrm{SM}} < 10^{-35}\ e \cdot \mathrm{cm}$ [3] [4].

Heavy polar molecules offer an attractive platform for these searches due to their intrinsic enhancement factors. In particular, molecules with large internal electric fields and close-lying opposite-parity states allow for the amplification of symmetry-violating effects [5]. Radium monofluoride (RaF) is especially well-suited for such measurements due to the presence of its radium nucleus being pear-shaped in some isotopes (^{222}Ra, ^{224}Ra, ^{226}Ra). These isotopes exhibit strong octupole deformation that enhances the nuclear Schiff moment (the observable related to a nuclear EDM) [6]. RaF possesses favorable molecular structure properties that allow for ultra-high precision measurements of small shifts of its electronic levels, down to the microHz level, induced by the presence of an EDM. One such property is its highly diagonal Franck–Condon factors (FCFs), which enable efficient laser cooling [7]. RaF has a ground electronic state of $X^2\Sigma^+$, with an unpaired electron, making it an open-shell molecule.

A series of spectroscopic experiments have been carried out at ISOLDE-CERN to characterize the RaF molecular structure. Ruiz et al. (2020) presented that RaF was first produced and spectroscopically analyzed to measure its low-lying vibronic structure [8]. Udrescu et al. (2021) measured isotope shifts for $^{223-226,228}$RaF, demonstrating agreement with ab initio predictions [9]. Wilkins et al. (2023) reported that a molecular Bohr–Weisskopf effect was observed in ^{225}RaF via magnetic hyperfine spectroscopy of the $A^2\Pi_{1/2} \leftarrow X^2\Sigma^+$ transition [10]. Udrescu et al. (2024) studied the $A^2\Pi_{1/2} \leftarrow X^2\Sigma^+$ transition at high resolution in ^{226}RaF, enabling the development of a laser cooling scheme [11]. Athanasakis-Kaklamanakis et al. obtained spectroscopy of the lowest 14 excited states of RaF and compared it to relativistic quantum chemical models [12] Despite these advances, a major challenge remains: producing neutral RaF in the cold, rovibrational ground state necessary for precision measurement. A proposed solution involves using a sodium vapor charge exchange cell (CEC) to convert an incoming RaF^+ ion beam into neutral RaF and subsequently, RaF^- [7]. Trapping a charged particle is easier than trapping a neutral particle. The motivation for trapping a negative ion as opposed to the positive ion is due to it being easier to remove an electron with a laser as opposed to adding one to produce the neutral. From a trapped anion, the electron is easily removed via photodetachment to yield neutral RaF molecules with low internal energy and high state selectivity. This thesis seeks to elucidate the ideal CEC parameters for the production of RaF^-. This will be done by modeling the double charge exchange process using a set of semiclassical methods designed to estimate reaction cross sections based on properties of the sodium vapor and the RaF species in either exchange. These models differ in taking into account properties such as the relative velocity of the colliding species, polarizability, and the dipole moment of the polar molecule. By combining these methods with the sodium vapor density and the physical dimensions of the charge exchange cell (CEC), it is possible to estimate how efficiently RaF^- can be produced. Figure 1.1 describes the overall process for this thesis, where the models to obtain the cross section of the first exchange are discussed in Chapter 5, followed by Chapter 6, which calculates the second exchange's cross sections. The necessary data analysis to determine the ion rate of both the cationic and anionic species, as well as the charge exchange temperature, is examined in Chapter 7. The final efficiency calculations for both experimental results and analytical models are presented and compared in Chapter 8. These models are intended to guide future experiments and help optimize RaF laser cooling and EDM measurement.

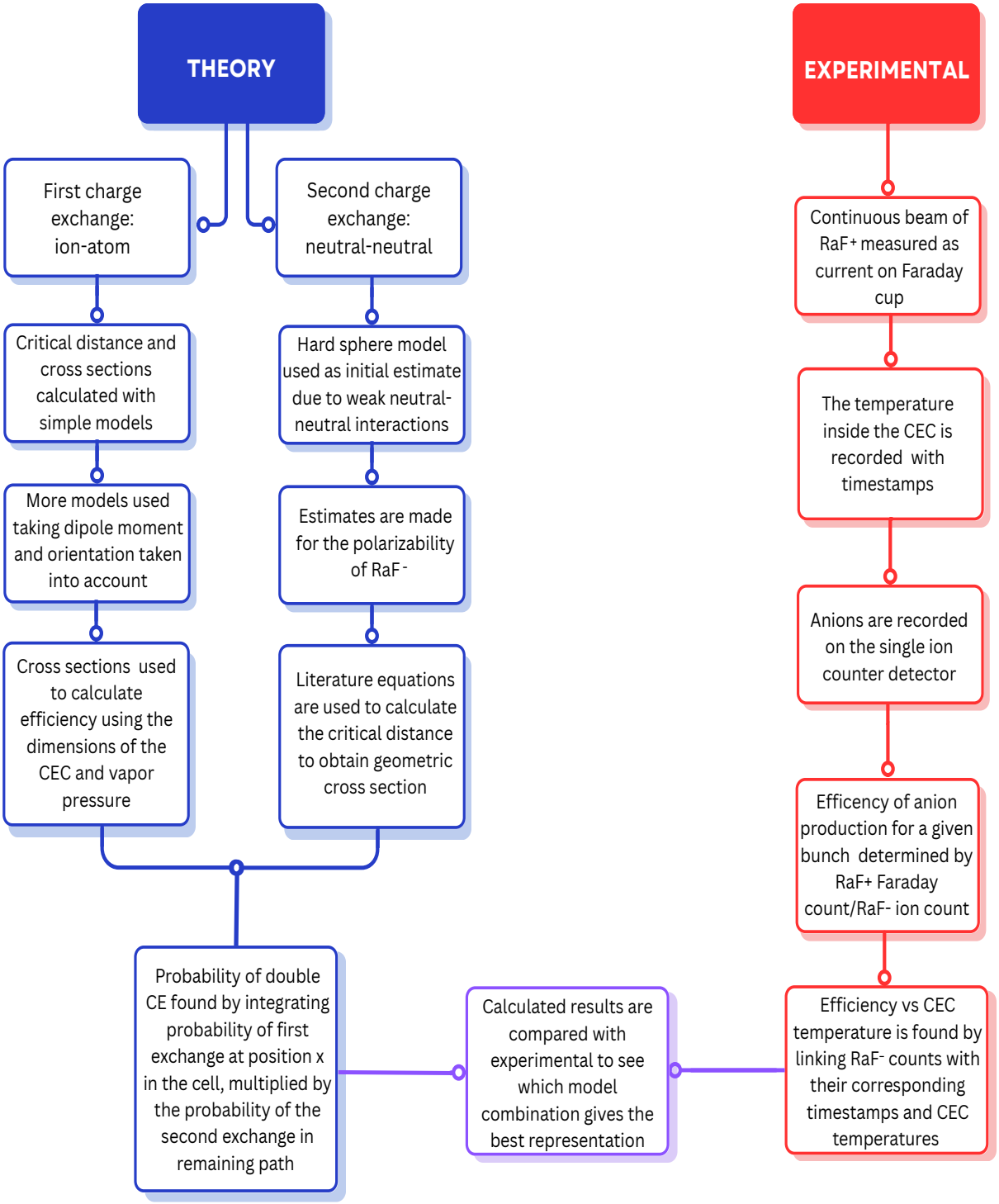

Figure 1.1: General flowchart for the process in obtaining and comparing the calculated vs experimental probability of RaF^- formation. The term "PES Curves" refers to potential energy surfaces. The details of all of these models, as well as any interpolated values used in the models, will be discussed in detail in the related chapter.

Chapter 2

Theory

2.1 The Schrödinger Equation in Collision Theory

Quantum mechanical non-relativistic treatment of charge exchange collisions is solved using the time-dependent Schrödinger equation (TDSE). The TDSE governs the evolution of a particle's wavefunction under the influence of an interaction potential that changes with time [13]. The TDSE in a one-dimensional space for a single non-relativistic particle is

$$i\hbar\frac{\partial\Psi(r,t)}{\partial t} = -\frac{\hbar^2}{2m}\frac{\partial^2\Psi(r,t)}{\partial r^2} + V(r,t)\Psi(r,t) \tag{2.1}$$

where $\Psi(r,t)$ is the wavefunction describing the probability of finding the particle at position r and time t, $\hbar$ is the reduced Planck's constant, m is the mass of the particle, and $V(r)$ is the potential energy [14].

In many-body systems, such as molecular collisions, the TDSE becomes dramatically more complex

$$i\hbar\frac{\partial}{\partial t}\Psi(\mathbf{r}_1,\mathbf{r}_2,\ldots,\mathbf{r}_N,t) = \hat{H}\Psi(\mathbf{r}_1,\mathbf{r}_2,\ldots,\mathbf{r}_N,t) \tag{2.2}$$

In this case of N-body systems, the Hamiltonian $\hat{H}$, including all kinetic and potential energy terms between the particles, is

$$\hat{H} = -\frac{\hbar^2}{2}\sum_{n=1}^{N}\frac{1}{m_n}\nabla_n^2 + V(\mathbf{r}_1,\mathbf{r}_2,\ldots,\mathbf{r}_N,t) \tag{2.3}$$

where N is the total number of particles in the system, m_n is the mass of the $n$the particle, and ∇_n^2 is the Laplacian with respect to its coordinates $\mathbf{r}_n$ [15]. The potential V includes all interactions between particles. The TDSE does not account for relativistic effects, which be-

come significant in heavy atoms where inner electrons move at velocities close to the speed of light. These high velocities change orbital shapes and energies; so, small alterations known as relativistic corrections to the Schrödinger equation must be applied when these effects are at play [16]. It is also important to take into account that it is not possible to analytically solve the Schrödinger equation except for very simple systems such as the hydrogen atom [17]. For more complex systems, such as charge exchange collisions, an approximation must be used.

2.2 Collision of a Fast Molecular Beam and Atom at Rest

The charge exchange between a diatomic ion such as RaF^+ and a neutral atom like Na can be simplified as a two-body collision process. In this case, the system consists of two bodies, a rigid rotor (RaF^+) and an atom, Na. RaF^+ is modeled as a rigid rotor, so that its internal bond is fixed at its equilibrium length. The interaction between the Na atom and the molecule is then characterized by their relative position and orientation, shown in Figure 2.1.

To simplify the system, Jacobi coordinates are commonly used. The Jacobi coordinate vectors for the system of interest are defined as follows:

- $\overrightarrow{r}$: The equilibrium bond vector between Ra and F atoms
- $\overrightarrow{R}$: The vector from the center of mass (COM) of RaF^+ to the Na atom
- θ: The angle between $\overrightarrow{r}$ and $\overrightarrow{R}$

As stated, r is held fixed, and the orientation of the molecule in space is described by the angle θ between $\overrightarrow{r}$ and $\overrightarrow{R}$.

The rigid-rotor approximation simplifies the treatment of RaF^+ while preserving the essential anisotropic features of the molecular target. The center of mass (COM) must be obtained for the rigid-rotor RaF^+.

To determine the COM of RaF^+, the standard formula can be used

$$R_{\text{COM}} = \frac{m_{\text{Ra}} x_{\text{Ra}} + m_{\text{F}} x_{\text{F}}}{m_{\text{Ra}} + m_{\text{F}}} \tag{2.4}$$

If the fluorine is at position zero and Ra is the equilibrium distance away, the COM location relative to fluorine is:

$$R_{\text{COM}} = \frac{m_{\text{Ra}} \cdot r}{m_{\text{Ra}} + m_{\text{F}}} \tag{2.5}$$

This COM serves as the origin for defining $\overrightarrow{r}$ and $\overrightarrow{R}$. As stated before, the Jacobi coordinates simplify the kinetic energy expression in the Hamiltonian. This makes it easier to solve the

Schrödinger equation by decoupling internal and external motions.

A schematic of the two-body Jacobi coordinate arrangement is shown in Fig. 2.1, where the RaF^+ molecule is aligned with $\vec{r}$ pointing from F to Ra, and the position of the neutral Na atom and the transferred electron are shown relative to the COM of the diatomic molecule.

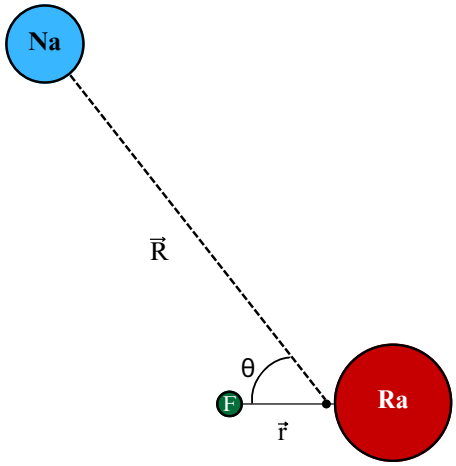

Figure 2.1: Jacobi coordinates used to describe the two-body charge exchange system involving RaF^+, Na. The internal coordinate $\overrightarrow{r}$ is fixed for the rigid rotor, and $\overrightarrow{R}$ connects the COM of RaF^+ to Na.

2.3 Elastic and Inelastic Collisions

Depending on how energy is redistributed in the system and what internal transitions take place during the interaction, collisions can be either elastic or inelastic [18][16].

Elastic

A collision is defined as elastic when the total kinetic energy of the system is conserved, and the internal states of the species remain unchanged. A pseudo-collision in which the species reflect Coulombic repulsion is known as Rutherford scattering and can be defined as elastic [19].

$$E_{\text{kin}}^{\text{out}} = E_{\text{kin}}^{\text{in}}, \tag{2.6}$$

This implies that the relative velocity before and after the collision is the same in magnitude

$$|\vec{v}_1' - \vec{v}_2'| = |\vec{v}_1 - \vec{v}_2| \tag{2.7}$$

Treating the collision as head-on between two particles of masses m_1 and m_2, with initial velocities v_1 and v_2, the final velocities after the collision are given by:

$$v_1' = \frac{m_1 - m_2}{m_1 + m_2} v_1 + \frac{2m_2}{m_1 + m_2} v_2, \tag{2.8}$$

$$v_2' = \frac{2m_1}{m_1 + m_2} v_1 + \frac{m_2 - m_1}{m_1 + m_2} v_2. \tag{2.9}$$

In the special case where the two masses are equal ($m_1 = m_2$), these simplify to:

$$v_1' = v_2, \quad v_2' = v_1. \tag{2.10}$$

Given this, it is possible that a charge exchange could be an elastic collision as in the instance $\mathrm{H}^+ + \mathrm{H} \rightarrow \mathrm{H} + \mathrm{H}^+$. However, an elastic charge exchange by definition will be symmetrical and resonant [20].

Inelastic

An inelastic collision involves energy redistribution from translational motion to internal modes, such as ionization or excitation. Although the total energy is conserved, part of the kinetic energy is converted into internal energy. In both inelastic and elastic collisions, the momentum is conserved.

The conversion of kinetic energy to internal energy results in less kinetic and relative velocity energy after the collision

$$E_{\text{kin}}^{\text{out}} = E_{\text{kin}}^{\text{in}} - \Delta E_{\text{int}}, \tag{2.11}$$

$$|\vec{v}_1' - \vec{v}_2'| < |\vec{v}_1 - \vec{v}_2| \tag{2.12}$$

where ΔE_{int} is the internal energy converted from the part of the initial kinetic energy. The internal energy gained can be in the form of rotational, vibrational, and electronic energy [21].

Contrary to elastic collisions where the masses are equal in charge transfers, the inelastic charge transfers can be for symmetric and asymmetric reactions [22]. Although elastic collisions are inherently resonant, inelastic collisions can be both nonresonant and resonant. If there is no net change in translational and internal energy, the collision is known to be inelastic and nearly resonant. This could happen in the case of a charge transfer where the ionization potential (IP) of the two species differ slightly, but the transferred electron ends up in an excited state of the product, and the energy of that excited state can offset the difference in IP [13].

Inelastic Collision Selection Rules

Just as spectroscopic selection rules dictate which optical transitions are allowed, inelastic collision reactions are governed by their own selection rules that depend on conserved properties

such as symmetry and angular momentum during the interaction.

Symmetry

Symmetry principles are central to understanding which transitions are allowed or forbidden during charge exchange collisions. In the present reaction, the total system evolves from an initial state Ψ_{initial}, representing the RaF^+ molecular ion and neutral Na atom, to a final state Ψ_{final}, after charge transfer.

The probability of a transition between these states is governed by the matrix element

$$\langle \Psi_{\text{final}} | \hat{H}_{\text{int}} | \Psi_{\text{initial}} \rangle, \tag{2.13}$$

which becomes zero if the initial and final states differ in symmetry under operations that are conserved throughout the collision [23].

Five fundamental symmetry invariances of the molecular Hamiltonian are identified as

1. Translation in space: resulting in conservation of total linear momentum

2. Translation in time and time reversal: ensures the conservation of energy and time-reversal symmetry of the S-matrix, which relates the initial and final quantum states in a scattering process

3. Rotation of all particle coordinates in space, corresponding to conservation of total angular momentum

4. Reflection of particle coordinates in the center of mass, giving rise to parity conservation

5. Permutation of indices in identical particles (nuclei and electrons): imposes exchange symmetry constraints (e.g., Pauli exclusion)

For linear molecules, electronic states are often labeled by their reflection symmetry: Σ^+, which is symmetric under reflection, and Σ^-, which is antisymmetric under reflection.

Transitions such as $\Sigma^+ \rightarrow \Sigma^-$ are symmetry-forbidden if reflection symmetry is conserved during the collision [13]. For homonuclear diatomic molecules, parity-based selection rules also apply to transitions between gerade (g) and ungerade (u) states, which are defined in respect to inversion through the molecular center.

Franck–Condon Considerations in Inelastic Collisions

Although it is not a selection rule, vibrational transitions are governed by the Franck–Condon (FC) principle. The FC principle provides a useful framework for understanding vibrational transitions that occur during fast electronic processes, such as charge exchange in molecular collisions. It states that the most intense molecular transition between vibrational states occurs on a timescale much shorter than the nuclear motion, so the internuclear separation is effectively fixed. On a potential energy diagram, the transition is represented as a vertical line between electronic states at constant bond length [16][24].

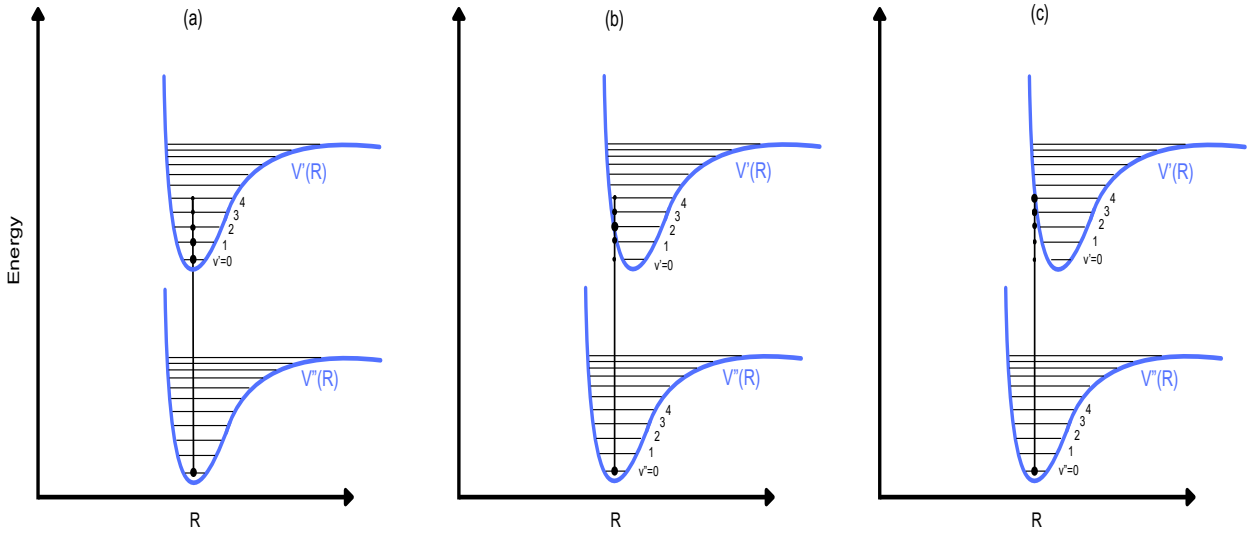

Figure 2.2: Franck–Condon transitions from the vibrational ground state to vibrational levels in the excited state, (a) the equilibrium distance does not change during excitation; (b) the equilibrium distance increases slightly during excitation; (c) the equilibrium distance increases greatly during excitation. Image inspired by [24].

The probability of a transition between vibrational states of the initial and final electronic configurations is quantified by the Franck–Condon factor, defined as the squared overlap of vibrational wavefunctions

$$q_{v'v''} = \left[\langle \psi^{v'}(\mathbf{r}) | \psi^{v''}(\mathbf{r}) \rangle\right]^2 \tag{2.14}$$

where $\psi^{v'}(\mathbf{r})$ and $\psi^{v''}(\mathbf{r})$ are the vibrational wavefunctions associated with vibrational levels v' and v'' in the final and initial electronic states, and $\mathbf{r}$ is the nuclear coordinate.

FCFs play a vital role in understanding which vibrational states will be populated, as the FCFs for the vibrational states of interest can be summed to get the overall probability of a vibrational transition. The exclusive population of low vibrational states is due to a near-diagonal Franck–Condon matrix. This means that the transition probabilities are largest when the vibrational quantum number remains unchanged ($v'' = v'$), so the molecule is most likely to remain in the same vibrational state during the electronic transition. Diagonal matrices indicate high selectivity and minimal vibrational branching [7].

2.4 Potential Energy Surfaces

The Born–Oppenheimer Approximation

The Born-Oppenheimer (BO) approximation simplifies calculations by factorizing the total wavefunction into separate electronic and nuclear components. It is based on the large mass disparity between electrons and nuclei, which allows the electrons to respond extremely quickly to nuclear movement [16]. The electrons can be treated as moving relative to fixed nuclei, so that electronic motion can be solved first, and then nuclear motion can be solved on the resulting potential energy surface (PES).

$$\Psi(\mathbf{r}, \mathbf{R}) = \psi_{\text{el}}(\mathbf{r}; \mathbf{R}) \cdot \chi(\mathbf{R}), \tag{2.15}$$

where ψ_{el} is the electronic wavefunction that depends dynamically on electron position $\mathbf{r}$ and parametrically on fixed nuclear positions $\mathbf{R}$, so that differing nuclei positions give different wavefunctions. $\chi(\mathbf{R})$ is the nuclear wavefunction.

The full molecular Hamiltonian is written as:

$$\hat{H} = \hat{T}_e + \hat{T}_N + \hat{V}_{\text{e-e}} + \hat{V}_{\text{n-n}} + \hat{V}_{\text{e-n}}, \tag{2.16}$$

which contains the kinetic energies of the electron and nuclei, $\hat{T}_e$ and $\hat{T}_N$, and the V terms are the potential energies of the system [14]. As stated before, the BO approximation fixes the nuclei, so the nuclear kinetic energy operator $\hat{T}_N$ is initially neglected. An adiabatic electronic wavefunction $\psi_{\text{el}}(\mathbf{r}; \mathbf{R})$ is obtained by solving the electronic Schrödinger equation:

$$\left[\hat{T}_e + \hat{V}_{\text{e-e}} + \hat{V}_{\text{e-n}}\right] \psi_{\text{el}}(\mathbf{r}; \mathbf{R}) = E_{\text{el}}(\mathbf{R}) \psi_{\text{el}}(\mathbf{r}; \mathbf{R}), \tag{2.17}$$

where $E_{\text{el}}(\mathbf{R})$ is the electronic energy eigenvalue at each internuclear geometry $\mathbf{R}$. This function defines an adiabatic PES where the nuclei subsequently move. Once $E_{\text{el}}(\mathbf{R})$ is obtained, the nuclear part of the wavefunction $\chi(\mathbf{R})$ is solved.

It should be noted that in collisions of extremely large projectile velocities, the BO approximation is no longer valid as the incident nuclei can no longer be considered as slowly changing relative to electrons, and nuclear motion must be included in a diabatic representation [25]. The velocity of the experiment of focus does not fall into the high velocity criterion as shown in Chapter 5; therefore, the BO approximation is applicable as orbital velocities of target electrons are greater than the relative collision velocity of the nuclei [13]. The BO approximation can also break down when two potential energy surfaces are close together, so there is little energy separation

$|V^I(R) - V^J(R)|$, enhancing the probability of nonadiabatic transitions [16]. This concept is relevant for the present system, as discussed in Chapter 4, where the collision energy lies in a regime where nonadiabatic transitions are likely. In low-energy charge exchange processes, avoided crossings can influence the electron transfer probability.

Nonadiabatic Coupling

Nonadiabatic or vibronic coupling describes how the nuclear motion in the molecule creates mixing between adiabatic electronic states. The coupling is quantified by the nonadiabatic derivative coupling vector

$$\mathbf{d}(\mathbf{R}) = \langle \psi_n | \nabla \mathbf{R} | \psi_m \rangle \tag{2.18}$$

where ψ_n and ψ_m are the electronic wavefunctions of the interacting species, and $\mathbf{R}$ represents the internuclear distance between them. These terms appear in the nuclear Schrödinger equation as coupling terms and describe how the motion of nuclei along the distance of two colliding species can cause transitions between electronic states. If the electronic states respond strongly to the nuclear motion, the derivative coupling vector becomes large. This can occur near avoided crossings, where the wavefunctions are rapidly changing, making a transition more likely [26].

Avoided Crossings

The von Neumann–Wigner non-crossing rule states that two PESs of the same symmetry cannot intersect for diatomic systems; instead, they form an avoided crossing, which is the way charge transfer always proceeds [27] [16]. Transitions between PESs are most probable near these avoided crossings, where the nonadiabatic coupling, $H_{12}(R)$, becomes large. When this coupling element is large compared to the energy difference between the two PES curves, the avoided crossing can be represented using a diabatic model

$$\hat{H}_{\text{diab}}(R) = \begin{pmatrix} V_1(R) & H_{12}(R) \\ H_{12}(R) & V_2(R) \end{pmatrix} \tag{2.19}$$

where V denotes the potential energy, as represented by the curves shown in Figure 2.3 and $H_{12}(R)$ is the coupling element between the two states, so that when $H_{12}(R) \neq 0$, there is an avoided crossing [27][28]. For a charge exchange reaction, Figure 2.3 can be described as V_1 being asymptotically $A^+ + B$ and V_2 being asymptotically $A + B^+$. The general two-level Hamiltonian capturing an avoided crossing using adiabatic representation obtained by diagonalizing the diabatic Hamiltonian is

$$\hat{H}_{\text{adiab}}(R) = \begin{pmatrix} V_+(R) & 0 \\ 0 & V_-(R) \end{pmatrix} \tag{2.20}$$

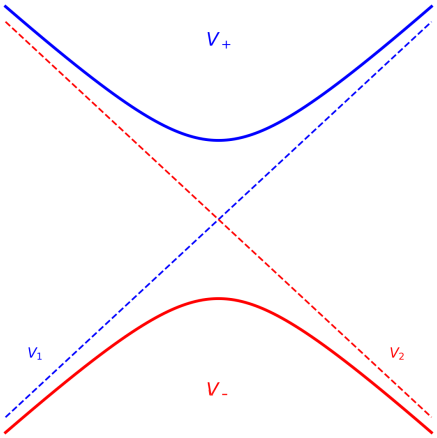

Figure 2.3: Adiabatic (solid) and diabatic (dashed) potential energy curves showing an avoided crossing. The adiabatic states V_+ and V_- exhibit energy splitting due to coupling, while the diabatic states V_1 and V_2 intersect at the crossing point. Adapted from [27].

2.5 Cross Sections in Charge Exchange Collisions

This chapter will conclude with classical and quantum descriptions of cross sections. In collisions, the cross section is the probability of interaction between colliding particles, so in a charge exchange case, the cross section determines the probability of electron transfer between the colliding species. It also allows a connection between theory and experiment [13].

Cross Section Classical Models

Models relying on classical mechanics are a good starting point for quantum descriptions when the de Broglie wavelengths are small [29]. The classical models rely on the angle of scattering of the impact parameter [30].

Impact Parameter Model

The impact parameter b is present in both elastic and inelastic scattering processes. It is defined as the perpendicular distance from the projectile's straight trajectory to the center of the target (see Fig. 2.4). The number of particles scattered per unit time between θ and $\theta + d\theta$ is equal to the number of incident particles per unit time with impact parameters between b and $b + db$. This relationship between impact parameter and scattering angle gives rise to the differential

cross section [30].

$$\frac{d\sigma}{d\Omega} = \frac{b}{\sin\theta}\left|\frac{db}{d\theta}\right| \tag{2.21}$$

In classical charge exchange modeling, the total cross section can be obtained by integrating the probability of charge exchange over the impact parameter

$$\sigma = 2\pi \int_0^{b_{\max}} b\, P(b)\, db \tag{2.22}$$

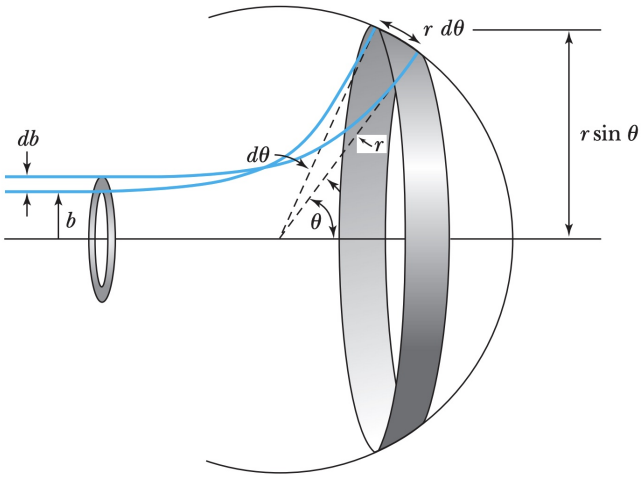

Figure 2.4: Depiction of impact parameter b, scattering angle θ, radius, r, from target to scattering distance, and the differential elements db and $d\theta$. Taken directly from [31].

Hard Sphere Model

In the hard sphere approximation, particles can be treated as hard spheres and only interact if their impenetrable surfaces touch. These hard surfaces make this model an elastic scattering. Since the model is spherical and the scattering is elastic, each impact parameter corresponds to a different scattering angle. The differential cross section for this case is constant:

$$\frac{d\sigma}{d\Omega} = \frac{R^2}{4}$$

Treating this value as the radius squared in the area of a sphere equation gives the total cross section

$$\sigma_{\text{tot}} = \pi R^2 \tag{2.23}$$

This model is commonly used for estimating cross sections in systems where the range of interaction is clearly defined and the scattering is isotropic [30].

Cross Section Theoretical Models

Quantum mechanically, scattering processes are described using wavefunctions and transition amplitudes. This serves as a foundation to build more complex models on. The incoming particle is represented as a wave packet, and how the system changed is described by the TDSE. Solving the TDSE gives the probability amplitudes for different outgoing wave components that correspond to the various final states of the system. These amplitudes determine the observable scattering outcomes. The scattering amplitude appears in the asymptotic form of the scattered wave [30]. If the incoming wave packet has a well-defined energy, the problem can be simplified using the time-independent Schrödinger equation. In this stationary framework, the wavefunction far from the scattering region is expressed in its asymptotic form as

$$\psi_{\vec{k}}(\vec{r}) = e^{i\vec{k}\cdot\vec{r}} + f(\theta,\phi)\frac{e^{ikr}}{r}, \tag{2.24}$$

Where the first term $e^{i\vec{k}\cdot\vec{r}}$ is the incoming plane wave moving toward the target, the second term is the scattered wave that spreads out spherically [30].

The differential cross section is defined as the squared magnitude of the scattering amplitude

$$\frac{d\sigma}{d\Omega} = |f(\theta,\phi)|^2 . \tag{2.25}$$

In collisions, it is possible to use a hybrid approach, treating the motion of the nuclei using classical mechanics, in their trajectory paths, and the electrons using quantum mechanics. This is known as a semiclassical model. There are many semiclassical models that have been developed to handle charge exchange collisions, and those relevant will be touched on later.

Chapter 3

Experimental Setup

3.1 ISOLDE at CERN

The experiment was conducted at the Isotope Separator On Line Device (ISOLDE) facility at CERN. ISOLDE generates low-energy radioactive beams that have been mass separated in the range of 30-60 keV. Additionally, there is a high-intensity and energy (HIE) area in the facility. There are two separators that are responsible for the mass separation: the high resolution separator (HRS) and the general purpose separator (GPS) [32]. All experiments with the Collinear Resonance Ionization Spectroscopy (CRIS) utilize the HRS, as the technique uses a beam of bunched particles as opposed to a continuous ion beam. This is achieved via a device named the ISOLDE COOLer (ISCOOL) located on the HRS. ISCOOL is a radio-frequency quadrupole cooler and buncher (RFQcb) trap.

The experiment was proposed during the winter physics period as ^{226}Ra has an extremely long half-life of 1,600 years. This experiment used a uranium carbide (UC_x) target, which was irradiated with 1.4 GeV of protons from the proton synchrotron booster (PBS) one week before the experiment ran, enough time to ensure the presence of Ra after irradiation. Hundreds of isotopes of lighter mass than uranium were produced from the nuclear reaction from the (UC_x) target, including the long-lived ^{226}Ra. After, carbon tetrafluoride (CF_4) gas was slowly added in to serve as the reagent in the formation of various neutral fluoride molecules [33]. The neutral radioactive species were ionized and accelerated to 30 kV for mass separation. This was achieved by setting the front end to 30 kV while the extraction electrode was grounded, creating a field gradient. To optimize the parameters needed to produce RaF^- the HRS was periodically set to isolate UO (A/q = 254) as stated before. Once the beam was tuned, the HRS was set to RaF^+ (A/q = 245), and an initial measurement of the quantity of RaF^+ molecules was obtained by the Faraday cup. These molecules were sent to the ISCOOL, the RFQcb trap filled with helium buffer gas. [34]. The radioactive ion beams (RIBs) that have been mass selected by the HRS go through ISCOOL in order to be bunched, increasing the signal-to-noise ratio

as data is collected from bunches getting to the detector, and cooled, allowing for improved transmission of the beamline [35]. This is done by adding an electric field gradient to pile up the ions in a potential well before ejection to the CRIS setup [8].

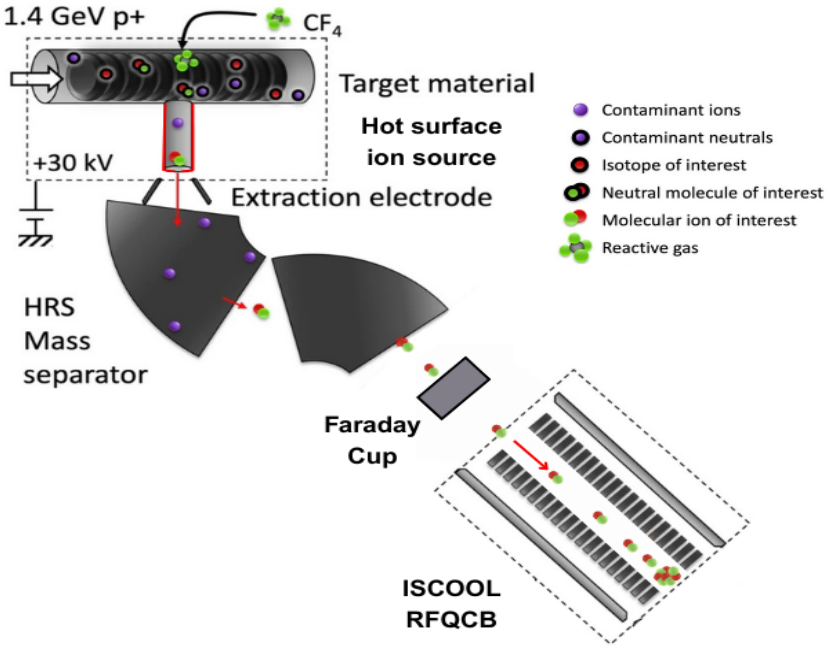

Figure 3.1: Detailed schematic of the ISOLDE portion of the experiment. Protons were sent in from the PSB to the target container containing uranium carbide. The image depicts the products after the nuclear reaction, which includes the neutral molecule of interest and neutral contaminants. All species are ionized by a hot tantalum line (shown as the red outline). RaF^+ is mass selected by the HRS, and the current is measured by the Faraday cup to get the number of ions. RaF^+ then enters ISCOOL to be cooled and bunched. Image adapted from [33].

3.2 CRIS Beam Line

Originally developed as an atomic spectroscopy technique, the CRIS experiment located in the ISOLDE facility provides information on nuclear structures of exotic isotopes from measurements of nuclear spin, nuclear magnetic dipole, and electric quadrupole moment, as well as changes in mean squared charge radii [36][37]. It does this by studying unstable isotopes with very short half-lives via multi-step ionization paired with the high resolution of collinear laser spectroscopy [38]. RaF has been the focus of multiple prior CRIS experiments, and information has been uncovered on its electronic, vibrational, rotational (rovibronic), and hyperfine structure [39]. Magnetic hyperfine interactions have been analyzed in detail by Wilken et al. (submitted for publication), and the quadrupole hyperfine structure is being investigated by C.M. Fajardo et al. (in preparation). Doppler-free resolution from the collinear lasers is ideal to study the hyperfine structure, spin, and isotope shifts of radioactive nuclei, as the Doppler effect broadens spectral lines. The purpose of this particular experiment is to obtain charge exchange parameters for the production of RaF^- and the electron affinity of RaF by photodetaching RaF^- into

RaF. The latter point will not be discussed in this thesis. For this reason, the collinear lasers that are implemented in most CRIS experiments were not needed. The CRIS setup chosen as all the necessary component were available there and the configuration used was a slightly modified version as the optical parametric oscillator (OPO) was placed at the end of the beamline instead of inside the laser tent and a neutral particle detector (NPD) was installed on the same axis as the MagneToF. Once the ion bunches from ISOLDE reached CRIS, they entered the charge exchange cell (CEC) that had been filled with sodium vapor as a result of heating solid sodium. The temperature of the CEC was measured from the center thermocouples, with another pair of thermocouples placed on the endcaps to ensure that too much sodium vapor did not escape the cell. Inside the CEC, the double electron capture takes place with subsequent single charge exchanges with the neutral sodium vapor. Sodium gas was chosen as the buffer gas of choice as the first charge exchange is nearly resonant due to the similar ionization potentials (IPs) of sodium (5.14 eV) and RaF (4.98 eV) [8][40][41]. Some of the RaF^+ ions undergo one charge exchange to yield the neutrals, some produce the anion, and others do not undergo a reaction at all, resulting in all three species being present after the CEC. All species continue on towards the electrostatic bender, whose polarity was switched depending on whether RaF^+ or RaF^- was to be detected on the MagneToF [42]. The neutrals produced from one charge exchange from the CEC are not directed by the bender and fly straight without detection. From there, if the polarity of the bender was negative, RaF^- was detected with the MagneToF, and an OPO provided a tunable laser to probe the photodetachment of RaF^- with the neutrals being detected by the NPD. The NPD is transparent to the OPO laser, but the MagneToF is not, so it was moved in and out of the beamline axis depending on the objective of the scan. Given the multiple detection devices in the experiment, the efficiency of negatively produced RaF anions can be determined by the measurements between the Faraday cup after the HRS and the MagneToF.

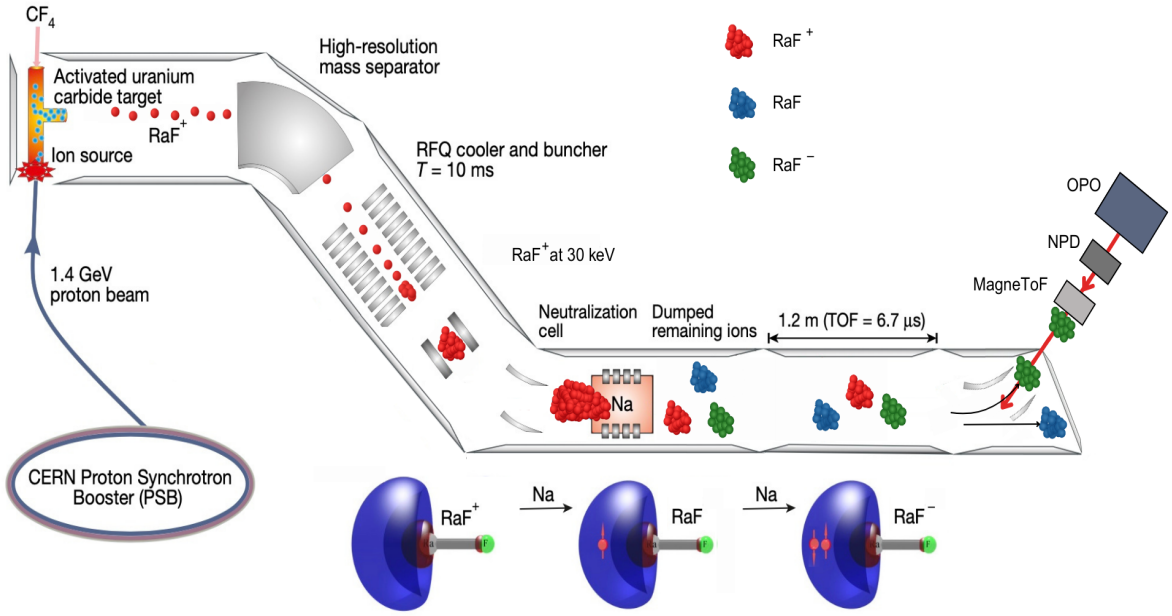

Figure 3.2: Experimental setup for the production of RaF^-, both ISOLDE and CRIS sides are shown. The ISOLDE side is not as detailed as Figure 3.1 but shows the PSB and the flow of RaF^+ from the target chamber, through the HRS and ISCOOL. The CRIS side details the ions going into the sodium CEC, where either a double charge exchange (DCE) of RaF^+ with Na, then the resulting neutral RaF with another Na atom to form RaF^-, single charge exchange (SCE) in which only the RaF^+ reaction with Na happens to form RaF, or no reaction occurs to give the three RaF species. These three reaction pathways yield the three most probable species of RaF^+, RaF, and RaF^-. In the case that is depicted in this image, the anions are separated from the neutrals and cations by the benders. The anions were detected with a separate MagneToF, and a tunable laser from an OPO was used to detach an electron from RaF^-, resulting in the neutral, whose presence could be detected in the NPD. As stated before, this image would be different if the polarity of the bender was switched to guide the cations. Adapted from [8] and [39].

Charge Exchange Cell

Since the production of RaF^- occurs via DCE inside the CEC, this component of the setup will be of primary interest in this thesis. The occurrence of DCE varies with the density of Na vapor, so the variation of CEC temperature measured through the thermocouple centers is of great importance. The charge exchange cell (CEC) was resistively heated using cartridge heaters powered by a Delta Elektronika power supply capable of delivering up to 32 V and 15 A. The temperatures were recorded during the experiment, giving the amount of RaF^- ions as a function of CEC temperature, which resulted in a curve with a maximum negative ion count, which will be discussed later.

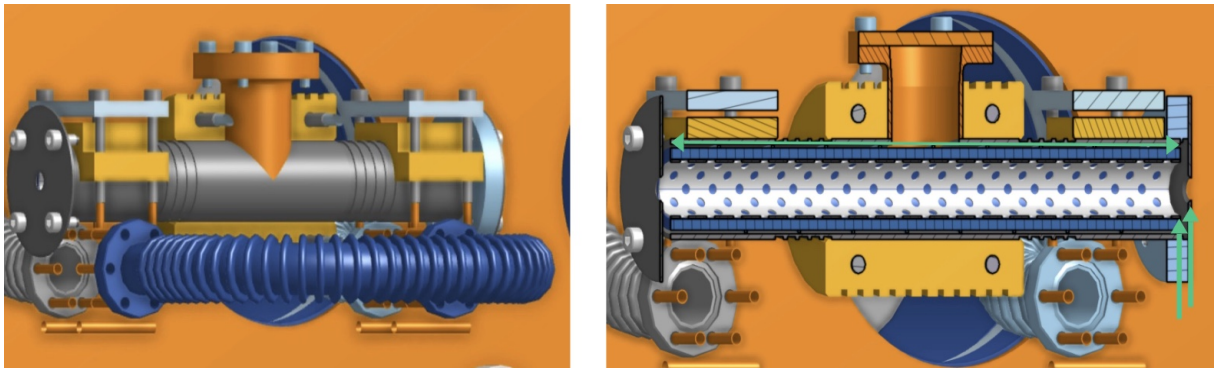

Figure 3.3: Details the CEC casing. The image to the right shows the cross section view with the dimensions of interest with green arrows (CEC radius and length along with beam entry size).

The measurements where the Na vapor is contained in the CEC is a cylinder with a length of 19 cm and a radius of 0.750 cm. The point of entry in which the RaF^+ beam is confined to is 0.300 cm, meaning the beam trajectory correlates to approximately 16% of the volume of the CEC. This measurement of the length will be referred to in the efficiency chapter.

3.3 Data Analysis

To evaluate the production of RaF^- ions during the charge exchange process, the count rate per ion bunch from the single ion detector (MagneToF) was analyzed as a function of the CEC temperature.The ISCOOL voltage readout was recorded and subsequently used to compute the effective ion beam kinetic energy. The corresponding temperature, measured by the thermocouple centers were used as the binning axis.

The temperature-dependent data were binned using a function that grouped events into fixed-width bins in temperature space. For each bin, the mean temperature, standard deviation, and total number of detected counts were calculated. To obtain a normalized count rate, the total counts in each bin were divided by the product of the number of bunches and the median time between bunches.

$$\text{Count Rate}_{\text{MagneToF}} = \frac{N_{\text{counts}}}{N_{\text{bunches}} \times \Delta t_{\text{median}}} \tag{3.1}$$

The resulting count rate was then plotted as a function of the bin center temperature.

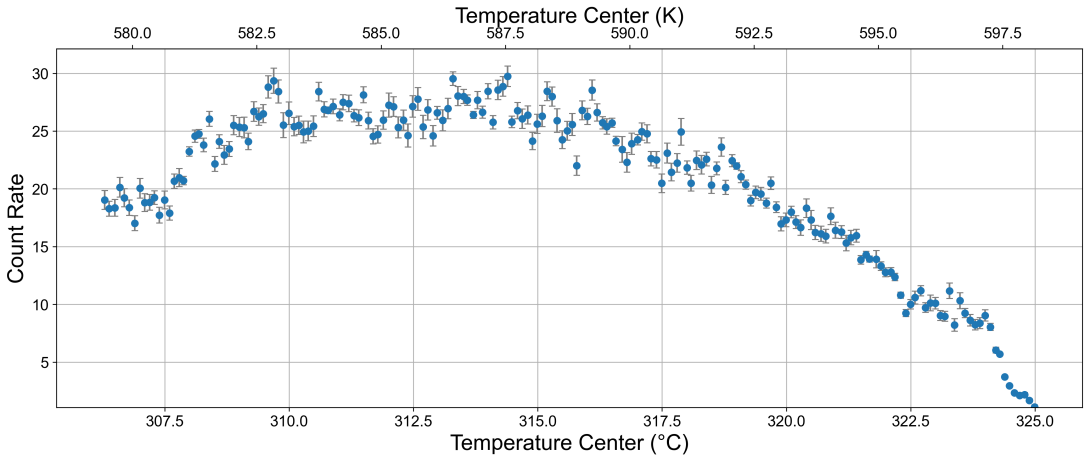

Figure 3.4: RaF^- count rate as a function of temperature. Counts were grouped into 0.1 °C bins, and the average time spent in each bin was used to calculate the count rate for that temperature.

Since the ions exit the RFQcb with a high velocity, a Doppler correction must be applied to the recorded wavenumber in order to make it relative to the fast-moving ion beam. Regarding the topic of this thesis, it does not involve a scanned spectroscopy frequency, so there is no laser frequency to be Doppler-shifted. However, an aspect of the experiment, the measurement of electron affinity, does involve laser spectroscopy frequencies. Doppler-shifts can be calculated using the formula

$$\nu = \nu_{\text{laser}} \cdot \frac{1+\beta}{\sqrt{1-\beta^2}}, \tag{3.2}$$

where $\beta = v/c$ is the normalized ion velocity,

$$\beta = \sqrt{1 - \left(\frac{(mc^2)^2}{(eV_{\text{acc}} + mc^2)^2}\right)}, \tag{3.3}$$

Where V_{acc} is the total acceleration voltage, m is the ion mass, and c is the speed of light.

Chapter 4

RaF^- Campaign

4.1 Experimental Approach

Background on Producing Cold Neutrals

Prior to this campaign, Hamamda et al (2015) proposed pathways to produce cold neutral polar molecules based on Rydberg electron transfer (RET), in which a highly excited Rydberg atom donates its outer electron to form an anionic polar molecule [43]. The resulting anion could then be decelerated and subsequently neutralized through photodetachment, yielding a cold neutral molecule. In the context of this experiment, this would follow the form of:

$$\mathsf{RaF} + \mathsf{Na}(n\ell) \rightarrow \mathsf{RaF}^- + \mathsf{Na}^+ \tag{4.1}$$

$$\mathsf{RaF}^- \rightarrow \mathsf{RaF} + e^- \tag{4.2}$$

This concept operates effectively within closed-shell molecules, where RET results in the formation of a weakly bound dipole-bound anion with a loosely attached electron that can be easily removed. However, for open-shell molecules such as RaF, anion formation requires the electron to occupy a valence orbital with compatible spin pairing and falls outside the assumptions of the dipole-bound RET model.

Reaction Process

While the potential energy curves of RaF^+ and neutral RaF are nearly parallel in their ground states, this is disrupted from neutralization collisions with other species [44][8][7]. The charge exchange interaction results in vibrational excitation and broad internal state distribution in the RaF product as mentioned in Chapter 1. It was proposed to use a second charge exchange

step, forming RaF$^-$. The motivation for this experimental scheme was strongly supported by theoretical predictions of nearly parallel potential energy curves among the lowest electronically excited states of RaF$^-$ as shown in Figure 4.1.

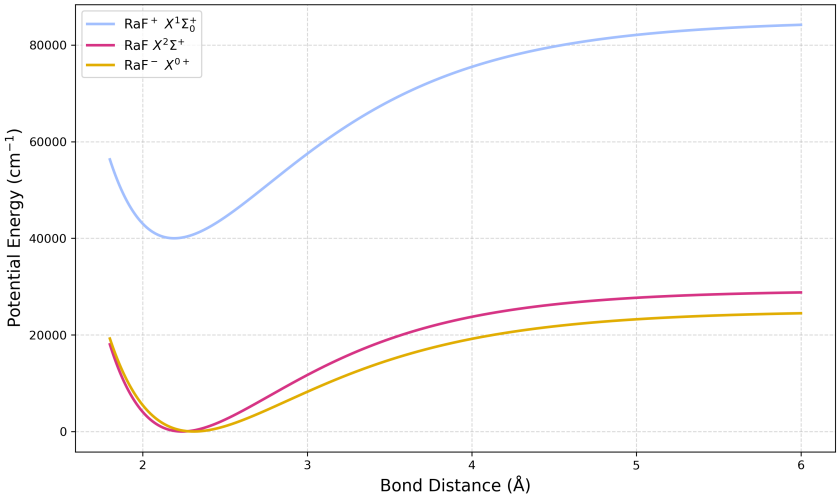

Figure 4.1: Potential energy curves for the ground states of RaF$^+$, RaF, and RaF$^-$. The RaF$^-$ state exhibits similar equilibrium bond lengths and nearly parallel shapes to RaF, enabling efficient electron transfer with minimal vibrational excitation. Morse potential parameters for RaF taken from "Spectroscopy of short-lived radioactive molecules" [8]. Morse potential parameters for RaF$^+$ taken from "Ion neutralisation mass-spectrometry route to radium monofluoride (RaF)" [41]. Morse potential parameters for RaF$^-$ taken from "Stopping mass-selected alkaline-earth metal monofluoride beams of high energy via formation of unusually stable anions" [7]. These values are listed in Table 4.1.

Table 4.1: Morse potential parameters for RaF$^+$, RaF, and RaF$^-$ states used to generate potential energy curves in Figure 4.1.

Species	State	D_e (cm^{-1})	r_e (Å)	ω_e (cm^{-1})	Method	Reference
RaF$^+$	$X^1\Sigma_0^+$	45100	2.19	502	4c RCC-SD	[41]
RaF	$X^2\Sigma^+$	29200	2.24	441.8	Experimental	[8]
RaF$^-$	X^{0+}	25000	2.31	383	4c-CCSD(T)	[7]

The narrow distribution gives a cold and well-defined population that can be further photodetached to yield the desired cold neutral molecules. The formation of RaF$^-$ in charge inversion collisions between RaF$^+$ and sodium vapor can proceed via two primary mechanisms, a double electron transfer (DCE) and a sequential single-electron transfer. In the DCE pathway, two electrons are transferred from a single sodium atom to RaF$^+$ in one step:

$$\mathrm{RaF}^+ + \mathrm{Na} \rightarrow \mathrm{RaF}^- + \mathrm{Na}^{2+} \tag{4.3}$$

The minimum energy necessary for this process can be estimated by [13]

$$\Delta E_1 = (\mathrm{IP}^{\mathrm{I}} + \mathrm{IP}^{\mathrm{II}})(\mathrm{Na}) - \mathrm{IP}^{\mathrm{I}}(\mathrm{RaF}) - \mathrm{EA}(\mathrm{RaF}) - E_{\mathrm{Na}} \tag{4.4}$$

where $(\mathrm{IP}^{\mathrm{I}}+\mathrm{IP}^{\mathrm{II}})(\mathrm{Na})$ is the double ionization potential of sodium, $\mathrm{IP}^{\mathrm{I}}(\mathrm{RaF})$ is the first ionization

potential of RaF, EA(RaF) is the electron affinity of RaF, and E_{Na} is sodium atom's recoil energy which is typically negligible at high incident energies [13].

Using the values of 5.14 eV for the first IP of sodium, 47.3 eV for the second IP of sodium, 4.969 eV as the IP of RaF, and 0.894 eV for the EA of RaF,[45][40][7] it is found that

$$\Delta E_1 \approx (5.14 + 47.3) - 4.969 - 0.893919 = 46.577 \text{ eV} \tag{4.5}$$

This large energy mismatch makes this reaction nonresonant and endothermic.

The second possibility for charge exchange proceeds through two independent single-electron transfer steps. In the first collision, RaF^+ is neutralized

$$\text{RaF}^+ + \text{Na} \rightarrow \text{RaF} + \text{Na}^+ \tag{4.6}$$

This pathway to produce neutral RaF has already been proven successful at ISOLDE. As mentioned in Chapter 3, this reaction is nearly resonant, as the ionization potential of sodium closely matches the ionization energy of RaF. After the first inelastic collision, the neutral RaF product retains some of the translational motion from the starting 30 keV beam and continues on to collide with another neutral sodium atom

$$\text{RaF} + \text{Na} \rightarrow \text{RaF}^- + \text{Na}^+ \tag{4.7}$$

The overall energy required for this sequential two-step charge inversion process can be estimated using [13]

$$\Delta E_2 = \text{IP}^{\text{I}}_a(\text{Na}) + \text{IP}^{\text{I}}_b(\text{Na}) - \text{IP}^{\text{I}}(\text{RaF}) - \text{EA}(\text{RaF}) - E_{a,\text{Na}} - E_{b,\text{Na}} - E_{\text{Na}} \tag{4.8}$$

where $IP^{\text{I}}_{a,b}(\text{Na})$ are the ionization energies of separate neutral sodium atoms in the first and second collisions (5.14 eV), $\text{IP}^{\text{I}}(\text{RaF})$ is the ionization energy of RaF (4.969 eV), and $\text{EA}(\text{RaF})$ is the electron affinity (0.894 eV), and the recoil energies can be excluded as previously stated [45][8][40][7].

$$\Delta E_2 \approx 5.14 + 5.14 - 4.969 - 0.893919 = 4.417 \text{ eV} \tag{4.9}$$

This is the minimum energy to drive both electron transfers. Since the first reaction is nearly resonant, the majority of this energy comes from the second exchange, but compared to the energy barrier from the DCE, this sequential process is far more thermodynamically favorable and efficient in the scheme of keV kinetic energies.

4.2 Rationale Behind Using Semiclassical Models

Ideally, the cross section values pertaining to the charge exchange reactions of interest could be obtained by a full quantum chemical computation. It is difficult to calculate the charge exchange reaction for the second exchange, as all electronic states of the neutral complex up to the threshold where the ion-pair is formed. In the context of RaF, this is especially challenging due to the relativistic effects arising from the heavy radium nucleus; so, relativistic corrections to the electronic wavefunction would be necessary for calculations. In the same vein, SOC also increases with atomic number, scaling approximately as $\sim Z^4$. As a result of this strong SOC in heavy atoms, quantum chemistry calculations require specialized relativistic treatment. This treatment is typically described in a four-component wavefunction, but this is not supported by most software programs. Consequently, in all relativistic SOC treatments, the four-component description must be reduced to a two-component representation that is compatible with most available computational packages. This conversion is difficult to implement as it requires precise derivation of expressions of two-component operators and error-free execution for every property. Gaul et al. (2020) utilized a quasirelativistic approach and extended it with modular computations through a ”toolbox” approach [46]. Given the complexity of such an approach and the difficult dynamics of the second charge exchange step, the execution of the computations necessary to achieve the overall efficiency of a double charge transfer to produce RaF$^-$ is outside the scope of a master's thesis, and semiclassical models will be employed to approach this challenge. To handle the efficiency of the double charge exchange, the reactions 4.6 and 4.7 will be treated separately to obtain individual cross sections.

In a collision, a channel represents possible configurations the system can take in terms of electronic states. If the quantum states are treated as interacting, they can be represented by coupled channels, as the channels influence each other. A coupling matrix element quantifies the strength of interaction as a function of internuclear distance, as first introduced in Eq. 2.19. The Rapp and Francis (RF) and Landau-Zener (LZ) models have been used for approximate solutions of coupled equations with two molecular states [47][48]. Relating to a double charge exchange, coupling would be between the initial ion and neutral state (entrance channel), the intermediate state after one electron transfer, and the final state where both electrons have been transferred (exit channel). However, even in circumstances of studying a reaction following the form of Equation 4.4, Almeida and Langford (1990) treated the transfers independently with two independent electron LZ transitions [49]. How much of a role channel coupling plays in a charge exchange process is strongly dependent on the relative velocity of the colliding particles. At low energies, there is enough time for electrons to exchange, leading to significant coupling between entrance, intermediate, and exit channels [50]. Transitions between them must be treated as coupled channels to accurately represent these collisions. These transitions often result from avoided crossings, exhibiting a gap due to a nonzero coupling matrix element. For collisions with higher energies, the duration of the interaction shortens, reducing the ability of the electronic wavefunction to follow nuclear motion, and nuclear motion dominates. The system evolves more diabatically, and the effect of coupling matrix elements becomes weaker.

Although the avoided crossings still exist, the probability of transitioning between coupled states decreases with increasing velocity. For this collision, the energy will be shown to fall in the low-energy region. Although a fully coupled quantum treatment would be most accurate in this low-energy regime, the infeasibility of such a treatment for RaF requires an alternative. Therefore, a semiclassical two-step model is adopted while acknowledging the limitations from not being able to take into account the effects of channel coupling, potentially underestimating the cross sections. In this approach, the cross sections for each charge exchange step are treated separately and then combined to estimate the overall efficiency of negative ion production.

Chapter 5

First Charge Exchange

5.1 Model Considerations

Energy Region

The applicability of models for handling charge exchange collisions is typically defined by the energy region the collision falls into. The kinetic energy is often expressed in energy per atomic mass unit (keV/u) of the projectile, which normalizes the energy across different systems. In the case of a RaF^+ ion with a mass of 245.023803 u and a total kinetic energy of 29.935211 ± 0.000044 keV (which will be shown in Chapter 7), the energy per atomic mass unit is calculated as

$$\frac{E}{m} = \frac{29.935211 \text{ keV}}{245.023803 \text{ u}} = 0.122173 \text{ keV/u}.$$

This value of 0.122173 keV/u places the collision in the low-energy region, defined as 0.01-1 keV/u [51]. Knowing this energy range will guide the models used, as the validity of charge exchange models greatly depends on it. The reaction

$$RaF^+ + Na \rightarrow RaF + Na^+ \tag{5.1}$$

is known as an ion-atom collision, a type of collision that is widely explored in literature. Models will be used to estimate the cross section of this ion-atom charge exchange, starting from the simplest and adding in complexity.

Input Parameters

Certain values will be used repeatedly throughout this chapter in the various models. Tables 5.1, 5.2, 5.3 contain the values of relevant dipole moments, polarizabilities, and ionization potential. Due to the absence of a published dipole moment for RaF^+, an estimate was obtained by leveraging the relationship between the neutral and cation dipole of a similar alkaline earth monofluoride, CaF. The approach relies on the equation

$$\mu = qa \tag{5.2}$$

where μ is the dipole moment, q is the charge separation, and a is the bond length a, all in atomic units.

Bond lengths for CaF and CaF^+ were taken from Harrison et al. (2002) at the relativistic coupled-cluster singles and doubles (RCCSD) level [52]. The dipole moments of CaF and CaF^+ were calculated in Molpro using CCSD with a dyall-v4z basis [53][54][55]. This gave a result of 1.2009 a.u. for CaF and 0.6400 a.u. for CaF^+. The bond lengths of RaF and RaF^+ were taken from literature [12]. The dipole moment of RaF used is the same one included in Table 5.1 and uses the Kramers-restricted configuration interaction method with single and double excitations (KRCISD) and a dyall-v4z basis set [56]. For each species, the effective charge separation q was back-calculated as $q = \mu/a$. The ratio of q between CaF^+ and CaF was found applied to the known q value of RaF to infer the expected q for RaF^+.

Given this, the dipole moment of RaF^+ was estimated to be:

$$\mu(\mathrm{RaF}^+) = q_{\mathrm{RaF}^+} \cdot a_{\mathrm{RaF}^+} \approx 5.3455 \times 4.0913 = 0.7654 \text{ a.u.} \tag{5.3}$$

This value provides a physically reasonable estimate for the dipole moment of RaF^+ for use in modeling the long-range interactions in the first charge exchange.

The polarizability of RaF is also a hurdle, as it has not been fully established. This challenge was alleviated by creating a range where the polarizability could fall. This was done by using values from literature from different methods (KRCISD/DFT) as well as interpolating the values from the same source by excluding RaF and calculating a proposed value using the trends of molecular mass from the other alkaline earth fluorides [56]. The lowest value in the range was from interpolating RaF by molecular mass from the available calculated polarizabilities of CaF, SrF, and BaF(using FSCC method with X2C Hamiltonian and s-aug-dyall.v4z basis set) [57].

Table 5.1: Dipole Moment

Molecule	**Dipole Moment (a.u.)**	**Method**	**Source**
RaF^+	0.7654	Calculation from CaF^+, CaF, and RaF	This work
RaF	1.424	KRCISD	[56]

Table 5.2: Polarizability

Molecule	**Polarizability (a.u.)**	**Method**	**Source**
RaF	219.5	KRCISD	[56]
RaF	299	DFT	[56]
RaF	552.550	DF Interpolated	[56]
RaF	439.340	KRCISD Interpolated	[56]
RaF	350.317	s-aug-dyall.v4z Interpolated	[57]
Na (^{2}S)	162.70	Experimental	[58]
Na^+	0.48	B3LYP/aug-cc-pVTZ	[59]

Table 5.3: Ionization Potential

Molecule	**Ionization Potential (a.u.)**	**Method**	**Source**
RaF^-	0.0328510	RECP-CCSD(T)	[7]
RaF	0.1826078	Dirac19 CCSD(T)	[40]
Na	0.1888580	Experimental	[45]

These values will continue to be referred to in the chapter. All of the parameters are in atomic units, and it should be noted that all the formulas mentioned in the models will be in atomic units unless noted otherwise.

5.2 Applicable Models

Hard Sphere Model

The simplest way to treat a collision is to view the partners as impenetrable spheres so that the reaction occurs if they come into contact [60]. The hard boundary of the two partners can be described by the van der Waals (vdW) radii, representing the closest distance of approach with

any non-bonded atoms or molecules, as illustrated in Figure 5.1. This neglects any attractive forces between the two species as well as any repulsive forces outside of those intrinsic to the vdW radius.

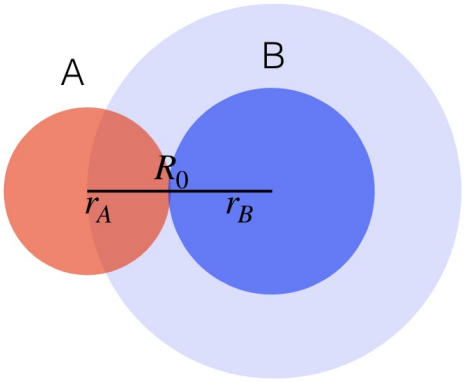

Figure 5.1: Representation of the hard sphere collision model, where the reaction occurs if there is contact between the two species, A and B. Taken directly from [60].

The vdW radius for sodium is given as 4.2897 a.u., 5.3479 a.u. for radium, and 2.7778 a.u. for fluorine [61]. It is not so simple as to add the vdW radii for radium and fluorine together, as this would be an overestimate, and the radius of RaF^+ is needed for the first charge exchange. A technique was applied that can estimate the molecular radius of a charged species based on the gradient of the electrostatic field potential, taking into account the extent of spatial influence [62][63]. More details on this method will be discussed in the next chapter. For now, the radius of RaF^+ was calculated in ORCA using CCSD and a dyall-v4z basis set [64][65]. The radius was found to be 5.9050 a.u. from the molecular volume, which is less then the summation of the atomic vdW radii (8.1257 a.u.) as expected. Now with a predicted radius for RaF^+ along with the vdW of Na, the cross section according to the hard sphere model can be found [60]

$$\sigma = \pi R_0^2 = \pi (r_A + r_B)^2 \tag{5.4}$$

This gives the geometric cross section for a radius of atom A and molecule B as depicted in Figure 5.1. The rate constant can then be obtained by [60].

$$k(T) = \int_0^\infty \sigma v f(v)\, dv = \sigma \int_0^\infty v f(v)\, dv = \pi R_0^2 \bar{v} \tag{5.5}$$

$$= \pi R_0^2 \sqrt{\frac{8 k_B T}{\pi \mu}} \tag{5.6}$$

where μ is the reduced mass of the system. The results at 585 K for the hard sphere model are below.

Table 5.4: Hard Sphere Model for First Charge Exchange at 585 K

r **(a.u.)**	σ **(a.u.^{2})**	k **(cm^3/molecule·s)**
10.19470	326.5355	7.019×10^{-10}

Classical Langevin Model

The Langevin theory is a straightforward way to obtain the cross section of an ion-atom collision, and has been built on by later models [66]. In its simplest form, it assumes that the neutral atom possesses no permanent dipole moment and a dipole is induced from the electric field of the ion. This results in a long-range attractive potential in the form of

$$V(r) = -\frac{\alpha}{2r^4} \tag{5.7}$$

where $V(r)$ is the interaction potential energy as a function of distance between the ion and atom r, and α is the polarizability of the neutral atom. This potential leads to a classical trajectory description where an ion approaching the neutral with an impact parameter less than a critical value of b_c incurs a reaction. Solving for this yields the Langevin cross section:

$$\sigma_L = 2\pi q\sqrt{\frac{\alpha_Y}{\mu}} \cdot \frac{1}{v} \tag{5.8}$$

where v is the relative velocity between the ion and the atom, μ is the reduced mass of the system, and α is the polarizability of sodium. The relative velocity from the impact must be found and will be used in further calculations. For a beam of RaF^+ with sodium as a thermal gas in the CEC, the relative velocity can be calculated from the separate velocities.

The velocity of RaF^+ is

$$v_{\mathrm{RaF^+}} = \sqrt{\frac{2E}{m_{\mathrm{RaF}}}} \tag{5.9}$$

where E is the kinetic energy and m_{RaF} is the mass of RaF.

For sodium vapor at temperature T, it follows a Boltzmann distribution.

$$v_{\mathrm{Na}} = \sqrt{\frac{2k_BT}{m_{\mathrm{Na}}}} \tag{5.10}$$

The relative velocity is then

$$v_{\mathrm{rel}} = v_{\mathrm{RaF^+}} - v_{\mathrm{Na}} \tag{5.11}$$

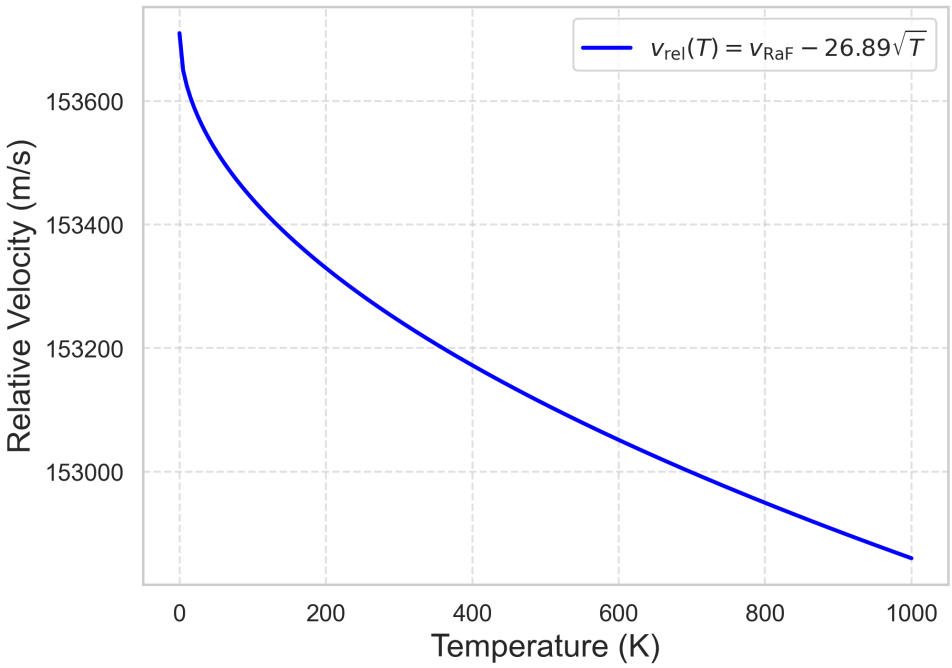

Figure 5.2: Relative velocity between RaF^+ (29.935211 keV) and Na vapor in the CEC as a function of temperature. The change in relative velocity is small over the 0-1000 K range.

As seen in Figure 5.2, the relative velocity at temperatures of 0 K in the CEC is 153710.00 m/s, whereas for temperatures of 1000 K it is 152859.52 m/s. This is only a 0.55% difference; a temperature of 585 K will be used throughout the relative velocity calculations for consistency, as it does not have a significant impact on the cross section. With all this in mind, the Langevin cross section gives a rather low value of 5.8643 a.u.^{2}.

The Langevin rate constant is defined as

$$k_L = 2\pi q \left(\frac{\alpha_e}{\mu}\right)^{1/2} \tag{5.12}$$

where q is the charge of the ion, α_e is the polarizability of Na in, and μ is the reduced mass of the system, all using cgs-esu units [67]. This results in a Langevin rate constant of 2.508×10^{-9} cm^3/s for the system of RaF^+ and Na.

Extended Langevin Model

Naturally, the classical Langevin Model that originally described charge-induced dipole interactions was further built upon to include London dispersion forces [68]. These forces arise from instantaneous dipole–induced dipole interactions, which create an uneven charge distribution from a polar neighbor (in this case, the approaching collision partner). The parameter C

describes the strength of the dispersion interaction

$$C = \frac{3}{2} \cdot \frac{\alpha_1 \alpha_2}{\left(\frac{\alpha_1^{1/2}}{N_1} + \frac{\alpha_2^{1/2}}{N_2} \right)} \tag{5.13}$$

α_1 and N_1 refer to the neutral atom (Na) and are the polarizability and number of valence electrons, and α_2 and N_2 are the polarizability and number of outer shell electrons for the ion (RaF^+). Polarizability ranges for RaF were used instead of the ion, as they were readily available. This range of neutral polarizabilities will be larger than that of its cation form, but it is used as this model is not expected to give accurate predictions. The interaction potential as a function of internuclear distance,r, is

$$V(r) = -\frac{\alpha_1}{r^4} - \frac{4C}{r^6} \tag{5.14}$$

The critical capture distance, r_c, is found by solving the expression

$$v_{\text{rel}}^2 = \frac{\alpha_1}{\mu r_c^4} + \frac{4C}{\mu r_c^6} \tag{5.15}$$

The cross section can then be found in the equation

$$\sigma(v) = \frac{2\pi}{\mu v_{\text{rel}}^2 r_c^4} \left(\alpha_1 + \frac{3C}{r_c^4} \right) \tag{5.16}$$

The first term serves as a scaling factor for the probability of a charge exchange at a given velocity. The second term details the strength of the attractive potential from both the charge-induced dipole interaction and dispersion contribution. The thermal rate constant is the average of the velocity-dependent cross section over the Maxwell–Boltzmann distribution of relative velocities, v, from the thermal motion of sodium in the charge exchange cell.

$$k(T) = \int_0^\infty v\, \sigma(v)\, P(v,T)\, dv \tag{5.17}$$

where the probability of having a specific relative velocity is defined as

$$P(v) = 4\pi \left(\frac{m}{2\pi k_B T} \right)^{3/2} v^2 \exp\left(-\frac{m v^2}{2 k_B T} \right) \tag{5.18}$$

where m is the reduced mass of RaF^+ and Na. The results for the parameter C, critical distance, cross section, and rate constant are shown in Table 5.5.

Table 5.5: Critical distance, capture cross section, and thermal rate constant at $T = 585$ K for various RaF polarizabilities using the Extended Langevin model. The units for polarizability are in a.u., which is defined as a_0^3.

Polarizability (a.u.)	C **(a.u.)**	r_c **(a.u.)**	σ**(v) (a.u.**^{2}**)**	$k(T)$ **(cm**^{3}**/s)**
219.50	3635.4	2.08254	1.32353	1.755×10^{-11}
299.00	4848.7	2.18199	1.19007	1.889×10^{-11}
350.32	5613.3	2.23457	1.12742	1.968×10^{-11}
439.34	6910.6	2.31162	1.04412	2.091×10^{-11}
552.55	8514.0	2.39185	0.96678	2.232×10^{-11}

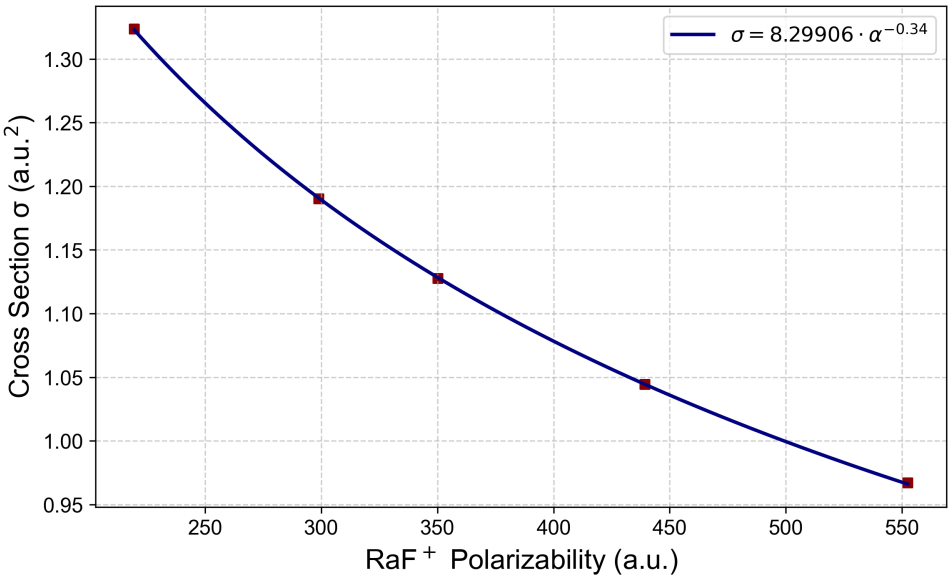

Figure 5.3: Extended Langevin Model cross section from Su-Bowers approach, $\sigma(v)$, as a function of RaF^+ polarizability at 585.15 K. A fit has been overlaid for comparison.

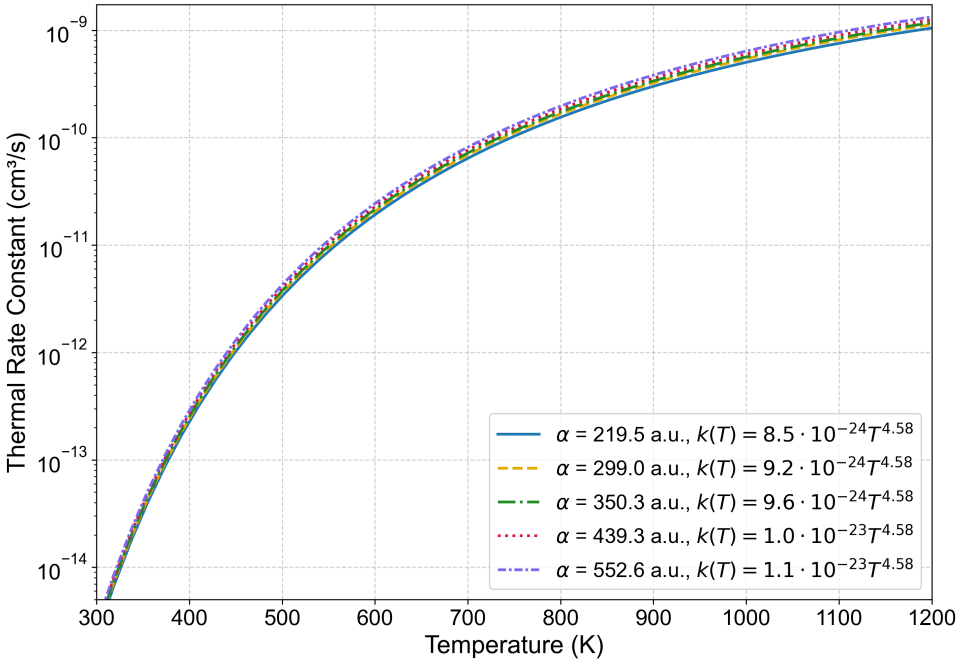

Figure 5.4: Extended Langevin Model thermal rate constant from Su-Bowers approach, $k(T)$ for varying polarizability values of RaF, taken from Table 5.2.

The thermal rate constant $k(T)$ increases steadily with temperature as shown in Figure 5.4 in the range of 300-800 K. This is due to the change in the Maxwell–Boltzmann velocity distribution and the increased probability of close-range encounters. This suggests that more kinetic energy increases the likelihood of charge exchange by allowing RaF^+ and Na to approach closer before repulsion dominates as the curve begins to flatten out at higher temperatures.

While this model starts to include more parameters than the classical Langevin model, it does not take into consideration dipole orientation or permanent dipoles, which are developed further.

Locked Dipole Model

A substantial literature review has been done on a collision system involving an ion and a molecule with a permanent dipole [69]. However, in this system, RaF^+ is both the ion and the molecule with a dipole, and sodium is the polarizable species. This reverses the roles from the given models, but the long-range interactions remain valid despite this inversion, as the electrostatic potential depends on the relative charges and how they are distributed, not by which collision partner carries them. This interaction potential is expressed by two terms and serves as the basis for the subsequent models. The first term describes the energy gain when a dipole is induced, and the second term captures the interaction between the permanent dipole of the projectile and the target. This depends on the dipole orientation; whether this term is attractive or repulsive depends on the alignment. To find the point where the potential energies cross by solving for the critical distance, the potentials of the entrance and exit channels can

be set equal to each other

$$-\frac{\alpha_{\mathrm{Na}}}{2R^4} - \frac{\cos\theta\mu_{\mathrm{RaF}^+}}{R^2} = -\frac{\alpha_{\mathrm{Na}^+}}{2R^4} - \frac{\cos\theta\mu_{\mathrm{RaF}}}{R^2} \tag{5.19}$$

where α is the polarizability and and μ is the dipole moment. This complete potential energy balance, when used to solve the critical distance, r, will be known as the "entrance-exit potential" for the subsequent models. Another form to solve r is a simplified method that focuses on the reactant potential

$$V(R) = -\frac{\alpha_{\mathrm{Na}}}{2R^4} - \frac{\cos\theta\mu_{\mathrm{RaF}^+}}{R^2} \tag{5.20}$$

where the left-hand side $V(R)$ can be replaced by $\mathrm{IP(RaF)} - \mathrm{IP(Na)}$, since RaF acts as the electron acceptor and Na as the donor. This considers only the entrance channel potential by balancing against the ionization energy gap between the reactants. It relies on the assumption that charge exchange becomes energetically allowed when the interaction energy compensates for the energetic cost of electron transfer. This will be known as the "ionization threshold" method when solving for r. In the case of a locked dipole, the dipole moment of RaF^+ is said to be perfectly aligned with the neutral axis. This gives an orientation angle $\theta = 0$, so that $\cos\theta = 1$. Under this assumption, the interaction is maximally attractive, and the second term in the potential simplifies to $-\mu/R^2$. This gives

$$-\frac{\alpha_{\mathrm{Na}}}{2R^4} - \frac{\mu_{\mathrm{RaF}^+}}{R^2} = -\frac{\alpha_{\mathrm{Na}^+}}{2R^4} - \frac{\mu_{\mathrm{RaF}}}{R^2} \tag{5.21}$$

for the entrance-exit potential and

$$IP(RaF) - IP(Na) = -\frac{\alpha}{2R^4} - \frac{\mu}{R^2} \tag{5.22}$$

for the ionization threshold in the locked dipole. Using the values from Tables 5.3, 5.2, and 5.1, the critical distance is calculated to be 6.0862 a.u. from the entrance-exit potential and 13.8119 a.u., from the ionization threshold, suggesting charge exchange is possible at much larger distances when using the simplified method. The cross section equation for the general equation Equation (5.32) is

$$\sigma = \pi r_c^2 + \frac{\pi\alpha}{r_c^2\mu v^2} + \frac{2\pi\mu_D}{\mu v^2}\cos\overline{\theta} \quad \text{(evaluated at } r = r_c\text{)} \tag{5.23}$$

where the reduced mass, μ, is differentiated from the dipole moment μ_D by the subscript. Equation (14) of Su and Bowers (1973) expresses the total capture cross section as a sum of three contributions: a geometric term, a charge-induced dipole interaction, and a permanent dipole alignment effect. This addition to the critical distance, r_c, is to represent the fact that the impact parameter, b, would be greater than r_c due to long-range attraction [70]. At 585 K, the cross section is found to be 116.4701 a.u.^{2} from the entrance-exit potential (EEP) and 599.3544 a.u.^{2} when using the ionization threshold (IT). Both of these values give larger results compared to the previous models. This increase is due to the inclusion of the permanent

dipole moment through the attractive term $\frac{\cos\theta\,\mu}{R^2}$. As discussed earlier, assuming an angle of $\theta = 0$ results in $\cos\theta = 1$. This maximizes the magnitude of this term without a sign change. This alignment condition makes the interaction strongly attractive at longer ranges, increases the critical radius, and leads to a much larger charge exchange cross section compared to the previously discussed models that neglect permanent dipole effects. The rate constant for Equation (5.32) is

$$k(T) = \left(\frac{2\pi q}{\mu^{1/2}}\right)\left[\alpha^{1/2} + c\mu_D\left(\frac{2}{\pi k_B T}\right)^{1/2}\right] \tag{5.24}$$

where c is a parameter between 0 and 1, detailing how locked in the species is (one in this case). This equation shows that at low temperatures the dipole term dominates, and at high temperatures, the rate approaches a constant. This rate behavior illustrated in Figure 5.5 is different from Figure 5.4, where the rate constant increased with temperature due to higher kinetic energy enhancing the likelihood of reactive collisions at shorter distances. The rate for the locked dipole model details the diminishing influence of dipole orientation as kinetic energy rises, as the thermal motion disrupts the alignment between the dipole and polarizable Na.

Table 5.6: Locked dipole model results at $T = 585$ K.

Method	r_c **(a.u.)**	σ **(a.u.^{2})**	$k(T)$ **(cm^3/s)**
Entrance–Exit Potential (EEP)	6.0862	116.4701	3.597×10^{-9}
Ionization Threshold (IT)	13.8119	599.3544	3.597×10^{-9}

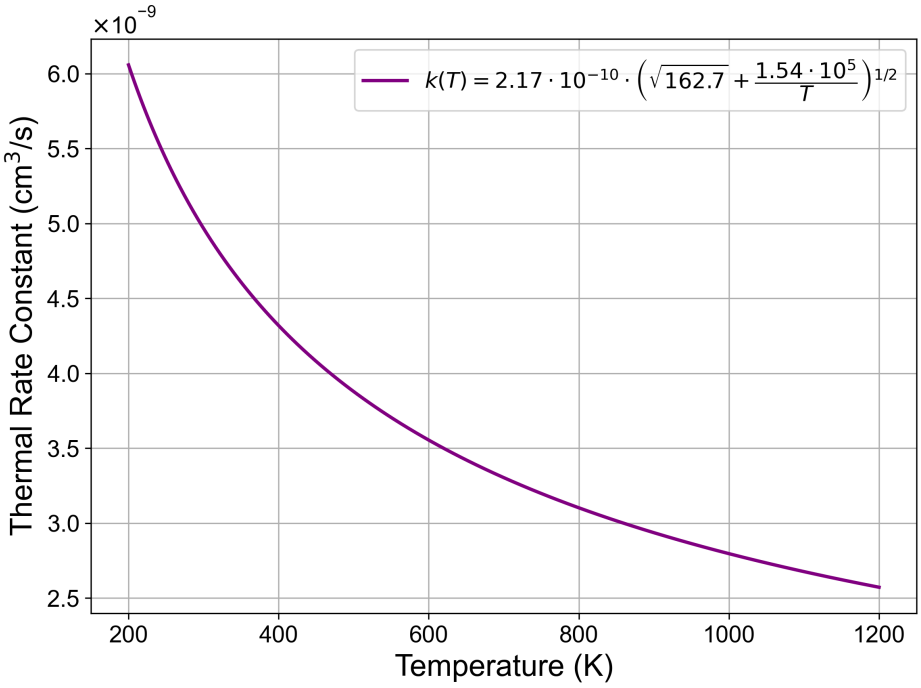

Figure 5.5: Rate constant from the Locked Dipole model as a function of temperature.

It is evident that the dipole orientation has a large impact on the critical distance, cross section, and rate constant. Although the simplest way to handle θ is to treat it as a locked dipole, this

is not realistic in collision experiments. The EEP method from Equation (5.21) can be used to see how the critical distance varies in Figure 5.6. The critical distance variation from the dipole orientation using Equation (5.22) is shown in Figure 5.6.

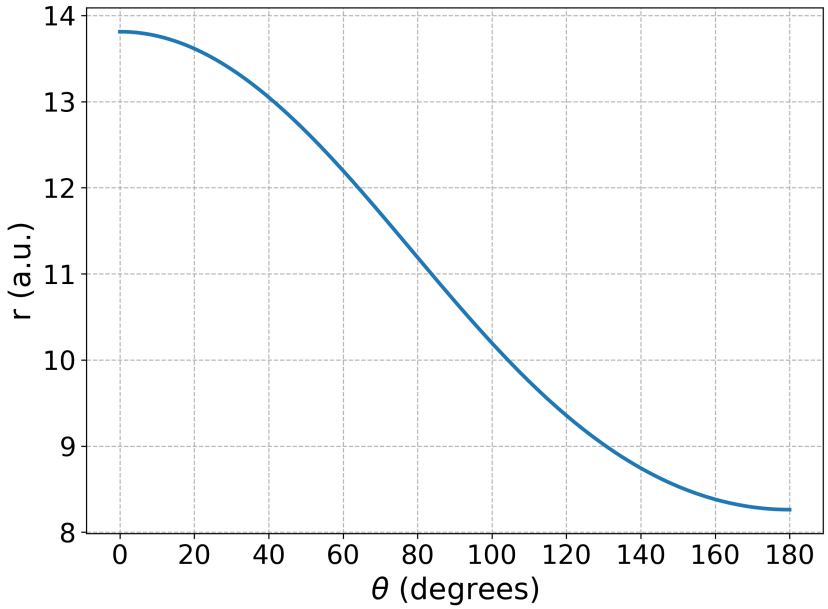

Figure 5.6: How the critical distance varies with dipole orientation angle θ in IT method from Equation (5.32) at 585 K. Charge exchange can occur at the largest separation distance between RaF^+ and Na when $\theta = 0°$ (locked dipole, 13.8119 a.u.), and at shorter distances when $\theta = 180°$ (8.261840 a.u.).

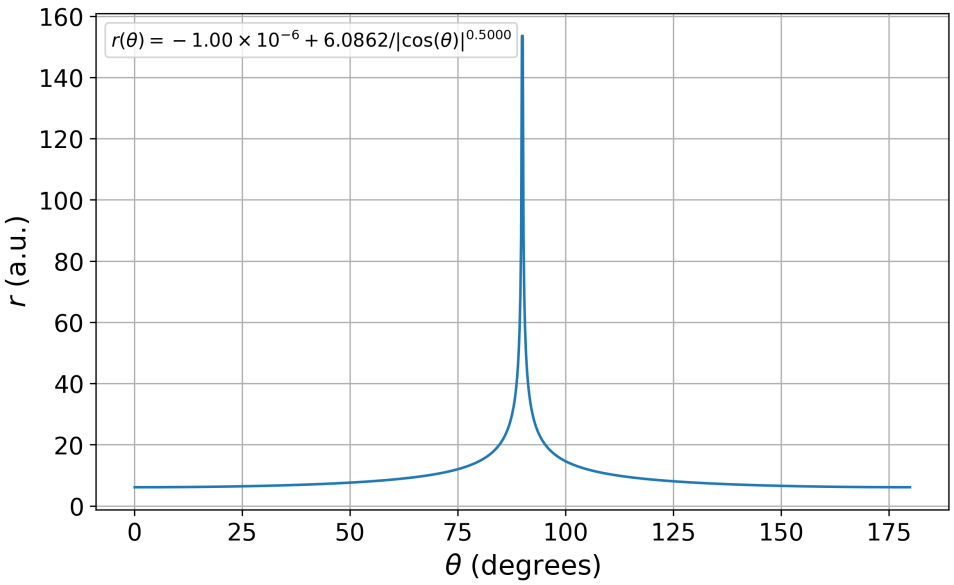

Figure 5.7: Variation of the critical distance as a function of the dipole orientation angle, based on the EEP (Equation (5.31)). The function shows the symmetric behavior of R about 90°, excluding the region between 89.9° and 90.1° to obtain the best fit for the other angles. The distance, r, diverges around 90°, meaning the potentials do not cross at a physically meaningful distance. However, by evaluating the function over very narrow increments of 1.0×10^{-13} degrees, realistic distances are obtained at $\theta = 90°$, oscillating between 1.4077 and 9.8635 a.u. These make more physical sense, but the mathematical relationship is not sound for reasonable results in this range due to the numerical instability. The crossing is 6.0862 a.u. when $\theta = 0°$ and 32.5789 a.u. at $\theta = 88°$.

Consequently, the cross section will change due to variation of dipole alignment. For the IT, the cross sections fall in the range of 214.438895 a.u.^{2}- 599.3144 a.u.^{2} as seen in Figure 5.8.

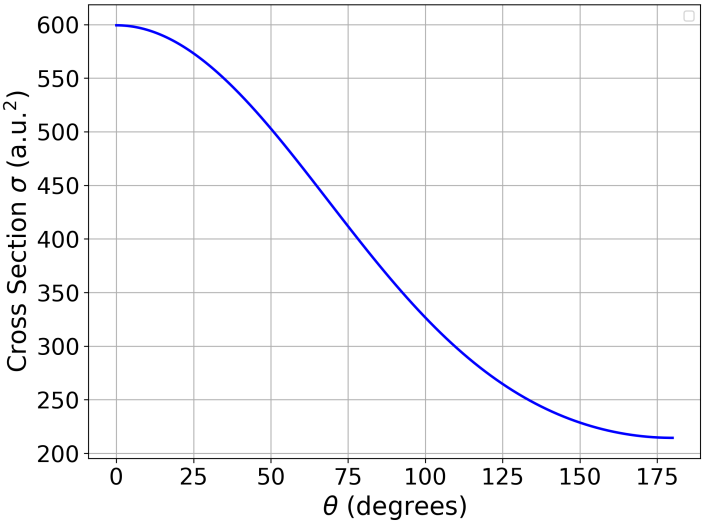

Figure 5.8: Cross section as a function of dipole orientation angle θ at 585 K using Equation (5.23) and the IT method. The variation in σ shows how the alignment affects the probability of charge exchange.

In the EEP, there is a drastic range in the cross section values, from $\theta = 0°$ (116.4701 a.u.^{2})

to the unrealistic value at $\theta = 89°$ (6667.8680 a.u.^{2}), attributed to the steep increase in cross section as the dipole orientation angle approaches $90°$. The average cross section across the valid range of angles (excluding $88°$–$92°$) is 300.6667 a.u.^{2}.

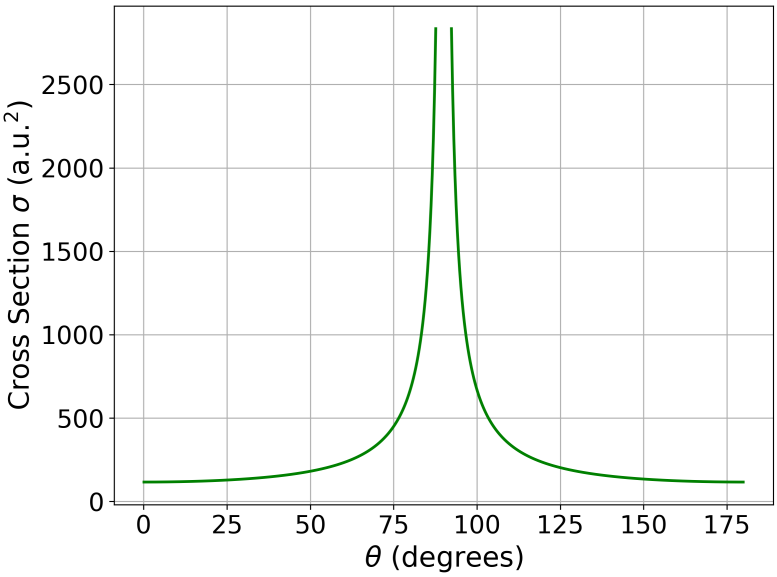

Figure 5.9: Cross section as a function of the dipole orientation angle θ, computed using Equation (5.23) and the critical distance $R(\theta)$ from Equation (5.31). The cross section shows strong dependence on this orientation. As stated, the magnitude increases rapidly as the angle approaches $90°$ and is not reliable for a cross section.

The next models will discuss different ways to handle this dipole orientation.

Average Dipole Orientation

The Average Dipole Orientation (ADO) model avoids the simplistic assumption of a "locked dipole" by averaging over the orientation angle θ. This is done with a weighted probability distribution [70]. This results in an average angle $\bar{\theta}$, calculated using

$$\bar{\theta} = \frac{\int \theta P(\theta)\, d\theta}{\int P(\theta)\, d\theta} \tag{5.25}$$

In the ADO framework, the weighting function $P(\theta)$ relies on the dynamics of the rotor under the influence of the induced dipole. This probability is proportional to the time the dipole spends at each orientation angle, dependent on the effective potential energy and rotational energy of the system. The average angle can then be expressed as

$$\bar{\theta}(r) = \frac{\displaystyle\int_0^{\pi} \frac{\theta \sin\theta\, d\theta}{\left[E_{\text{rot}} + \left(\frac{\mu_D}{r^2}\right)\cos\theta\right]^{1/2}}}{\displaystyle\int_0^{\pi} \frac{\sin\theta\, d\theta}{\left[E_{\text{rot}} + \left(\frac{\mu_D}{r^2}\right)\cos\theta\right]^{1/2}}}$$

where μ_D is the dipole of RaF^+ molecule, and E_{rot} is its rotational energy.

When the polar molecule RaF^+ approaches a neutral sodium, its rotational motion is affected by the ion-induced dipole. As the negative end of RaF^+s dipole rotates toward Na, it experiences an attractive interaction and transfers angular momentum from the system to the RaF^+ rotor. If the positive end approaches, the rotor decelerates and transfers angular momentum back to the system [70]. This leads to oscillatory angular momentum exchange; this oscillatory behavior influences the dipole alignment described by the average orientation angle $\theta(r)$. To determine if this motion is oscillatory or not, it should be determined if

$$E_{\text{rot}} \gg \frac{\mu_D}{r^2} \quad \text{or} \quad E_{\text{rot}} \ll \frac{\mu_D}{r^2}.$$

In the high rotational energy case, $E_{\text{rot}} \gg \frac{\mu_D}{r^2}$, the RaF^+ molecule rotates freely, and the ion-induced dipole interaction with the nearby sodium atom has little effect on its orientation. When $E_{\text{rot}} \ll \frac{\mu_D}{r^2}$, the electric field from the induced dipole of Na is strong enough to disturb the rotational motion of RaF^+, leading to oscillatory alignment of the dipole. A specific rotational energy for a rotational quantum number, J, is given by

$$E_{\text{rot}} = BJ(J+1) \tag{5.26}$$

Although the original treatment does not specify a rotational level, the rotational quantum number $J_{\max}$ at 585 K was selected to estimate the rotational energy of RaF^+. This assumes that RaF^+ reaches thermal rotational equilibrium with sodium in the CEC. This may overestimate the true rotational excitation, as the high translational energy of the beam does not necessarily equate to rotational energy. However, it can provide an upper bound for the rotational energy.

$$J_{\text{max}} \approx \sqrt{\frac{k_B T}{2B}} - \frac{1}{2} \tag{5.27}$$

and

$$B = \frac{h^2}{8\pi^2 I}, \qquad I = \mu r_e^2 \tag{5.28}$$

I is the moment of inertia, μ is the reduced mass of RaF^+, and r_e is the bond length of RaF^+ where a value of 2.165 Å is used [12]. From Equation 5.27, $J_{\max} \approx 31$. To ensure all appropriate distances are covered, the range from the EEP and IT methods for r is included, to compute E_{rot} as shown in Table 5.7.

Table 5.7: Comparison of rotational energy and dipole interaction energy for $J = 31$ as a function of r.

r **(a.u.)**	E_{rot} **(a.u.)**	$q\mu_D/r^2$ **(a.u.)**
1	0.0009276	0.765367
2	0.0009276	0.191342
3	0.0009276	0.085041
4	0.0009276	0.047835
5	0.0009276	0.030615
6	0.0009276	0.021260
7	0.0009276	0.015622
8	0.0009276	0.011959
9	0.0009276	0.009450
10	0.0009276	0.007654
11	0.0009276	0.006330
12	0.0009276	0.005303
13	0.0009276	0.004525
14	0.0009276	0.003901
15	0.0009276	0.003402
16	0.0009276	0.002986
17	0.0009276	0.002631
18	0.0009276	0.002323
19	0.0009276	0.002053
20	0.0009276	0.001914
21	0.0009276	0.001736
22	0.0009276	0.001583
23	0.0009276	0.001448
24	0.0009276	0.001331
25	0.0009276	0.001225
26	0.0009276	0.001131
27	0.0009276	0.001050
28	0.0009276	0.000975

Even though $J_{\max}$ does not vary with internuclear distance, Table 5.7, shows it alongside μ_D/r^2 for comparison. It is evident that even at the highest distance, $E_{\text{rot}} \ll \frac{\mu_D}{r^2}$, meaning that there is not enough rotational energy to dislodge the dipole alignment [70]. This absence of necessary

rotational energy leads to the equation for $\bar{\theta}$

$$\bar{\theta} = \frac{2\sqrt{2}A}{\sqrt{1-\cos K}} \tag{5.29}$$

where A is an integral over allowed dipole orientations and K is the maximum angle for the RaF^+ dipole when rotating in the induced field of Na, $\cos K = -\frac{E_{\text{rot}}\, r^2}{q\mu}$.

Since R is unknown, both $\bar{\theta}$ and R have to be be solved self-consistently. To achieve this, the expression for $\bar{\theta}(R)$ from Eq. 5.29 was substituted into the relationship between R and θ in both the EEP and IT methods to identify the self-consistent root values. This led to an $\bar{\theta}$ of $76.3003°$ for the EEP and $75.0635°$ using IT. The critical distance was calculated for the IT and EEP methods by using $\overline{\theta}$ as the angle value in Eqs. (5.32) and (5.21). All the parameters were input into Equation 5.23 to obtain the cross section.

Table 5.8: ADO results at $T = 585$ K.

Method	r_c **(a.u.)**	σ **(a.u.^{2})**	k**(T) (cm^3/s)**
EEP	12.5062	491.3838	1.877×10^{-9}
IT	11.4449	411.5346	1.944×10^{-9}

The ADO model was initially developed to characterize ion-polar molecule collisions, specifically for proton transfer reactions. The method has been shown to reproduce the dipole dependence for charge transfer, but may not be a good indicator for the absolute magnitude of charge transfer rate constants [71]. While this can provide a useful approximation of orientational effects, it can be further expanded to average orientation within the effective potential in the system [71].

Total Angular Momentum Conserved Average Dipole Orientation

The Average Angular Momentum Conserved Dipole Orientation (AADO) model extends the ADO Model by relaxing its assumption that, on average, there is no angular momentum exchange between the rotating dipole (RaF^+) and the target Na [71]. Instead, AADO conserves total angular momentum during each collision and calculates the average dipole alignment $\overline{\cos\theta}$ in the effective potential. As stated in the ADO section, in this system, RaF^+ is the dipolar molecule and is subject to alignment by the induced field it creates in polarizable Na. To determine which form of the angle-averaged dipole alignment $\overline{\cos\theta}$ to use, it is important to evaluate whether the dipole rotational energy dominates or is negligible [72]. In the high rotational energy case of ($E_{\text{rot}} \gg \frac{\mu_D}{r^2}$), the dipole is essentially freely rotating and only weakly aligned. If $E_{\text{rot}} \ll \frac{\mu_D}{r^2}$, the dipole motion is significant, and the low rotational energy form is to be used. As shown in Table 5.7, the dipole dominates over the rotational energy in the distance range at

585 K. Therefore, the equation to be used for the $\overline{\cos\theta}$ is

$$\overline{\cos\theta} = \frac{1}{3}\left[1 - \frac{2E_{\text{rot}}r^2}{q\mu_D}\right] \tag{5.30}$$

As in the same case with the ADO, there is a circular dependency as $\overline{\cos\theta}$ relies on r in Equation (5.30) and r in the exit-entrance potential method as

$$-\frac{\alpha_{\text{Na}}}{2R^4} - \frac{\overline{\cos\theta}\,\mu_{\text{RaF}^+}}{R^2} = -\frac{\alpha_{\text{Na}^+}}{2R^4} - \frac{\overline{\cos\theta}\,\mu_{\text{RaF}}}{R^2} \tag{5.31}$$

and the ionization threshold by

$$V(R) = -\frac{\alpha_{\text{Na}}}{2R^4} - \frac{\overline{\cos\theta}\,\mu_{\text{RaF}^+}}{R^2} \tag{5.32}$$

This can be addressed by finding the pair of $\overline{\cos\theta}$ and r that best matches the solutions in these potentials. For the EEP, energy matching between entrance and exit channels, Equation (5.31) can be used. A range of distances between 6.0862 a.u. and 32.5789 a.u. was tested, each yielding a corresponding $\overline{\cos\theta}$ using the AADO model in Equation (5.30). Each pair of r and its calculated $\overline{\cos\theta}$ can be used in Equation (5.31) to find where the inequality is minimized. From the top ten pairs where the inequality was minimized, half of the results were in a physically meaningful pair, as it is not in the vicinity of 90 degrees. That pair that gave the best agreement corresponds to a critical distance of 7.8467 a.u. and an angle-averaged alignment of 0.283587. For IT, a range of r values between 8.2618 a.u. and 13.8119 a.u. can be input into Equation (5.30), reflecting the bounds discussed earlier. Each distance gives a $\overline{\cos\theta}$ that can be used with its associated distance and compared to the known value of $IP(RaF)-IP(Na)$ to get a pair that minimizes the deviation. This procedure gives a critical distance of $r = 11.3563$ a.u. and an angle-averaged alignment of $\overline{\cos\theta} = 0.22913$. The cross section can be found by using the r value and $\overline{\cos\theta}$ in Equation (5.23).

Table 5.9: AADO model results at $T = 585$ K.

Method	r **(a.u.)**	σ **(a.u.^{2})**	$k(T)$ **(cm^3/·s)**
EEP	7.8467	193.4804	2.025×10^{-9}
IT	11.3563	405.1843	1.851×10^{-9}

Temperature-dependence of ADO

Both the ADO and AADO were formulated under the assumption that the reaction takes place at 300 K. The ADO was reparameterized in the context of higher temperatures [73]. This was done by finding the temperature dependence on the dipole locking coefficient c. This coefficient depends on the ratio $\mu_D/\alpha^{1/2}$, which determines how effectively the dipole can be aligned by the electric field generated during the collision. Molecules with large dipole moments and small partner polarizabilities are more easily oriented, leading to stronger long-range interactions.

As temperature increases, the dipole's rotational motion becomes more significant, leading to partial or complete randomization of its orientation. At low temperatures, the dipole aligns closely with the ion's field ($\theta \approx 0°$, $c \approx 1$), resulting in strong long-range attraction. At higher temperatures, thermal rotation disrupts this alignment, increasing the average orientation angle and reducing c toward zero. This behavior is captured in tabulated values of c as a function of both $\mu_D/\alpha^{1/2}$ and temperature, enabling accurate interpolation for use in applying it at 585 K for the experiment of interest. Table I in Su and Bowers (1975) was used to create a function to extract the coefficient c at 585 K with a $\mu_D/\alpha^{1/2}$ ratio of 0.155873. This is visualized in Figure 5.10.

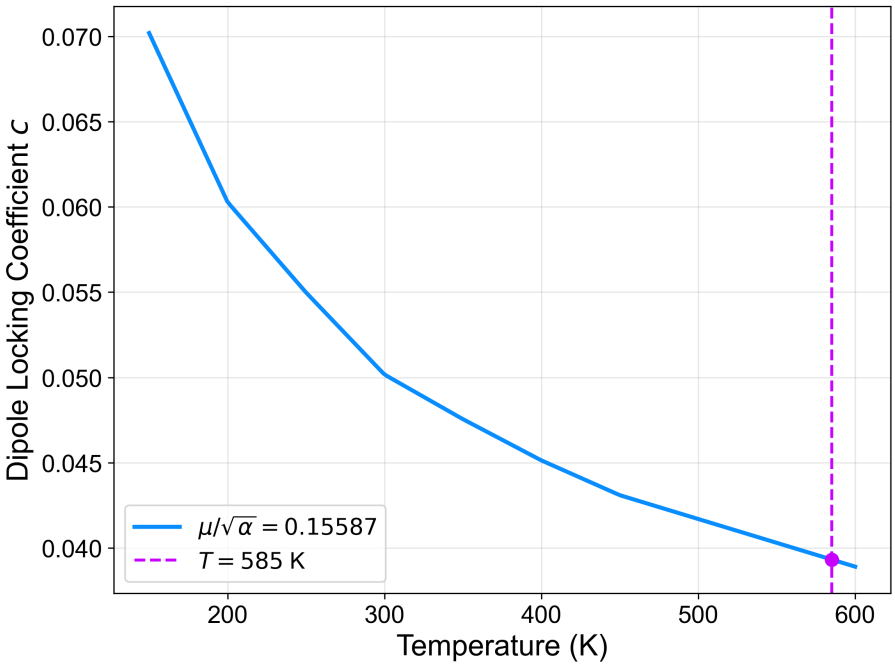

Figure 5.10: Temperature dependence of the orientation coefficient c for $\mu/\sqrt{\alpha} = 0.1559$.

Using the interpolation method, a parameter c, $\cos\theta$, of 0.0393 is obtained ($87.746°$). After inputting this value with Equation 5.31 for EEP and Equation 5.32 for IT, the cross section can be found. The results for the temperature-dependent ADO method are shown in Table 5.10.

Table 5.10: Temperature-dependent ADO model results at $T = 585$ K.

Method	r **(a.u.)**	σ **(a.u.^{2})**	$k(T)$ **(cm^3/·s)**
EEP	30.6906	2959.1602	1.041×10^{-9}
IT	10.7956	366.1632	1.041×10^{-9}

5.3 Summary of First Charge Exchange Results

Table 5.11: Comparison of first charge exchange models at $T = 585$ K.

Model	r **(a.u.)**	σ **(a.u.^{2})**	$k(T)$ **(cm^3/·s)**
Hard Sphere	10.1947	326.5355	7.019×10^{-10}
Langevin	–	5.8643	–
Extended Langevin	2.083–2.392	0.967–1.324	$(1.755–2.232) \times 10^{-11}$
Locked Dipole (EEP)	6.0862	116.4701	3.597×10^{-10}
Locked Dipole (IT)	13.8119	599.3544	3.597×10^{-9}
ADO (EEP)	12.5062	491.3838	1.877×10^{-9}
ADO (IT)	11.4449	411.5346	1.944×10^{-9}
AADO (EEP)	7.8467	193.3804	2.025×10^{-9}
AADO (IT)	11.3563	405.1843	1.851×10^{-9}
Temp.-Dep. ADO (EEP)	30.6906	2959.1602	1.041×10^{-9}
Temp.-Dep. ADO (IT)	10.7956	366.1632	1.041×10^{-9}

As shown in Table 5.11, the hard sphere model predicts a cross section of 326.54 a.u.^{2}, which falls within the range predicted by the locked-dipole and ADO-derived models. This close agreement suggests that the hard-sphere approximation can agree with those that take permanent dipole moments and their orientation into consideration when using the vdW radius for the neutral target atom alongside the electrostatically determined radius of the polar ionic projectile molecule. The Langevin-based models, which only consider ion-induced dipole interactions, are significantly lower. This discrepancy highlights the potential limitations of Langevin-based approaches in systems such as this, where long-range interactions dominate.

There is a discrepancy when comparing critical distances from the EEP model and IT methods. The EEP model equates the long-range interaction potentials of the reactant and product channels, providing crossing distances that capture the behavior of the system. However, near $\theta = 90°$, the dipole terms vanish, leading to numerical instability and divergence, and the results are not physically realistic in this range. The IP threshold method remains stable across all angles, as it is calculated from the fixed energy cost of the difference in the ionization energies of the RaF electron acceptor and Na donor. Altogether, it is expected that the EEP method gives a better prediction for the critical distance than the IT method when not in the divergence range. As seen in Table 5.11, the EEP method is not realistic for the temperature-dependent ADO model, as it corresponds to an angle of $87.746°$.

Chapter 6

Second Charge Exchange

6.1 Model Considerations

The second charge exchange of the reaction

$$\mathrm{RaF} + \mathrm{Na} \rightarrow \mathrm{RaF}^{-} + \mathrm{Na}^{+} \tag{6.1}$$

is a bit more uncertain in the ways to model, as it is a neutral-neutral collision that results in ion-pair formation. At longer ranges, the dipole moment of a neutral molecule such as RaF behaves as a neutral point, whereas at closer ranges this is not the case. It would be expected that ion-atom collisions have a much larger cross section due to their long-range interaction potential than that of a reaction with two neutral species [74]. Despite any initial Coulombic, induced-dipole, or permanent dipole attraction, the RaF and Na electron transfer can occur at relatively large distances from a jump of the sodium's valence electron to RaF at a distance that corresponds to the crossing point of the lowest covalent (neutral) and ionic (ion-pair) potential energy surfaces [75]. This model is known as "harpooning" and does not depend on the dipole moment of RaF [76]. For an ion-pair reaction, there are three distinct velocity regions: the threshold region where collision time $\gg$ vibrational excitation time, the post-threshold region where collision time approximately equals vibrational excitation time, and the high velocity regime where collision time $\ll$ vibrational excitation time [77]. These three types determine the stretching of the RaF^{-} bond length and whether RaF^{-} is quenched by Na^{+}. For the system, the collision time can be estimated for a range of critical distances as shown in Table 6.1, and the vibrational time can be found from the harmonic vibrational wavenumber of RaF^{-}, 401 cm^{-1} [7].

Table 6.1: Comparison of collision time at various critical distances with the vibrational time of RaF^-.

Critical Distance (Å)	**Collision Time (fs)**	**Vibrational Time (fs)**
0.5	0.095	83.18
1.5	0.286	83.18
2.5	0.477	83.18
3.5	0.668	83.18
4.5	0.858	83.18
5.5	1.049	83.18
6.5	1.240	83.18
7.5	1.431	83.18

This puts the reaction in the high velocity region, meaning the vibrational states are essentially frozen during the collision, and the distribution of RaF^- vibrational levels will match the neutral RaF vibrational distribution according to the Franck-Condon principle, as RaF will not be quenched by Na and there will be no bond stretching during the transfer. In these higher velocity regions, the orientation of species is not significant [76]. Additionally, which species possesses the negative charge in the ion pair depends on which is more electronegative. Values that will be used in the models for this chapter are listed in Tables 6.2 and 6.3.

Table 6.2: Polarizability

Molecule	**Polarizability (a.u.)**	**Method**	**Source**
Na (^{2}S)	162.70	Experimental	[58]
Na^+	0.48	B3LYP/aug-cc-pVTZ	[59]

Table 6.3: Ionization Potential

Molecule	**Ionization Potential (a.u.)**	**Method**	**Source**
RaF^-	0.0328510	RECP-CCSD(T)	[7]
Na	0.1888580	Experimental	[45]

This chapter will go through the various models that were used for the neutral-neutral interaction.

6.2 Applicable Models

Hard Sphere Model

Starting with the hard sphere view of a collision, as with the last chapter, neutral RaF and Na can be said to be impassible spheres. Using the vdW radius of Na (4.2897 a.u.) and the STREUSEL radius of RaF (5.5078 a.u.) (which will be discussed in detail in this chapter), the cross section can be found [62][63].

$$\sigma = \pi R_0^2 = \pi(r_A + r_B)^2 \tag{6.2}$$

The rate constant at 585 K is [60]

$$k(T) = \int_0^\infty \sigma v f(v)\, dv = \sigma \int_0^\infty v f(v)\, dv = \pi R_0^2 \bar{v} \tag{6.3}$$

$$= \pi R_0^2 \sqrt{\frac{8k_B T}{\pi \mu}} \tag{6.4}$$

The hard sphere model results are shown in Table 6.4.

Table 6.4: Hard Sphere Model for Second Charge Exchange at 585 K.

r **(a.u.)**	σ **(a.u.**^{2}**)**	$k(T)$ **(cm**^{3}**/s)**
9.7975	301.5630	6.483×10^{-10}

Hubers–Kleyn–Los High-Velocity Model

The cross section in an ion-pair formation relies on the crossing radius R_c and the coupling matrix element $H_{12}(R_c)$ [77]. The crossing radius is given by

$$R_c = \frac{1}{\Delta E},$$

where $\Delta E = \mathrm{IP_{Na}} - \mathrm{EA}_v$, with EA_v representing the vertical electron affinity of RaF. The coupling element decays exponentially with R_c, such that larger separations reduce the likelihood of electron transfer. The IP of sodium is available in Table 6.3, but only the adiabatic electron affinity of RaF is known. Using the adiabatic EA as opposed to the vertical gives a slight underestimate for R_c as it is larger as seen in Figure 6.1, but should give a good approximation as the RaF and RaF^- curves are nearly parallel.

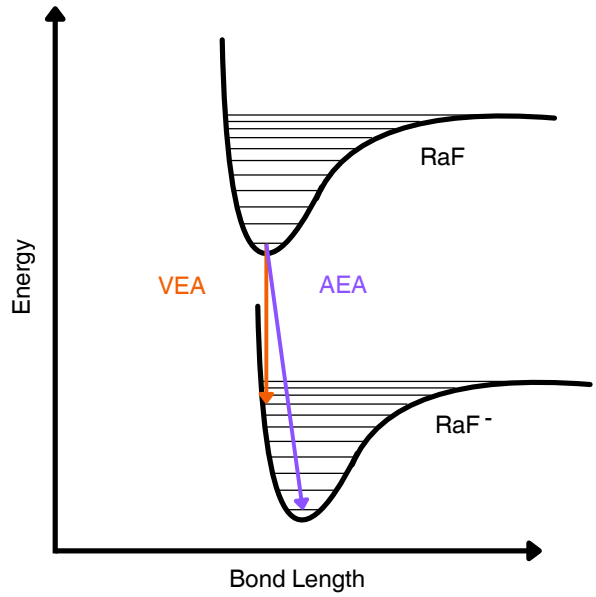

Figure 6.1: Schematic representation of the difference between vertical and adiabatic electron affinities (VEA and AEA). Figure inspired by [78].

Using the values from Table 6.3 gives

$$R_c = \frac{1}{0.1888547 - 0.0328509} = 6.4101 \text{ a.u.} \tag{6.5}$$

The geometric cross section then obtained by

$$\sigma = \pi R_c^2 \tag{6.6}$$

The results for the Hubers–Kleyn–Los model are given in Table 6.5.

Table 6.5: Hubers–Kleyn–Los High-Velocity Model Results at 585 K

r (a.u.)	σ (a.u.^{2})
6.4101	129.0861

Kimura Model for Ion-Pair Formation at 585 K

Kimura (2007) described the interaction between two neutral species using a weak polarization potential in the entrance channel and a Coulomb potential in the final ion-pair state [79]. The long-range interaction before charge transfer is given by

$$V_i(R) = -\frac{\alpha_{\mathrm{Na}}}{R^4}, \tag{6.7}$$

where α_{Na} is the polarizability of sodium. After ion-pair formation, the interaction potential has a Coulombic attraction

$$V_f(R) = -\frac{1}{R}. \tag{6.8}$$

Equating the entrance and exit potentials gives the condition

$$\frac{\alpha_{\mathrm{Na}}}{R^4} = \frac{1}{R}, \tag{6.9}$$

which simplifies to

$$\alpha_{\mathrm{Na}}^{1/3}. \tag{6.10}$$

Using the polarizability of sodium, the critical distance is calculated as

$$R_c = (162.7)^{1/3} = 5.4592 \text{ a.u.} \tag{6.11}$$

The geometric cross section is computed by

$$\sigma = \pi R_c^2 = \pi \times (5.4592)^2 = 93.6285 \text{ a.u.}^2 \tag{6.12}$$

The results for the Kimura model are in Table 6.6.

Table 6.6: Kimura Model Results at 585 K

R_c **(a.u.)**	σ **(a.u.^{2})**
5.4592	93.6285

Dissociation Model

The dissociation model is based off an analytical approach that describes the dissociation of Rb_2 into its ion-pairs, Rb^+ and Rb^-, giving an equation for the potential of this ion formation. [80]. Of course there is no dissociation in the reaction of interest; however, in the equation from the paper, it is seen that the dissociation energy was computed from subtracting the EA of Rb from the IP of Rb, this was substituted in as the IP of RaF^- subtracted from the IP of Na

$$V_{\mathrm{ion}}(R) = \mathrm{IP}(\mathrm{Na}) - \mathrm{IP}(\mathrm{RaF}^-) - \frac{1}{R} - \frac{\alpha(\mathrm{Na}^+) + \alpha(\mathrm{RaF}^-)}{2R^4} \tag{6.13}$$

and neutral potential can be described as shown in the Kimura model

$$V_{\mathrm{neutral}}(R) = -\frac{\alpha_{\mathrm{Na}}}{R^4}, \tag{6.14}$$

These two equations can be set equal to each other to find the crossing distance, as done in Chapter 5, and this method is denoted as the exit-entrance potential (EEP). Alternatively, the

potential can be set equal to the energy cost of electron transfer, the IP of the electron donor subtracted from the IP of the acceptor. This method is known as the ionization threshold (IT)

$$\mathrm{IP}(\mathrm{RaF}^-) - \mathrm{IP}(\mathrm{Na}) = \mathrm{IP}(\mathrm{Na}) - \mathrm{IP}(\mathrm{RaF}^-) - \frac{1}{R} - \frac{\alpha(\mathrm{Na}^+) + \alpha(\mathrm{RaF}^-)}{2R^4} \tag{6.15}$$

All the terms needed are in Table 6.2 and Table 6.3 with the exception of the polarizability of RaF^-. As calculating the polarizability of RaF^- would be extremely difficult, a technique was applied to predict a value similar to the vdW radius, which could then give a range of possible polarizabilities as a relationship between the two has already been established [81].

As mentioned earlier, the STREUSEL method varies from vdW by the cutoff boundary assigned to a species [62, 63]. Van der Waals qualifies the closest approach for a non-bonded species through overlapping spheres [62]. The STREUSEL method, on the other hand, calculates the boundary as the distance from the nucleus where the electric field changes less than a specified threshold (10^{-5} eV/electron), representing the chemically affected space. This accounts more for long-range effects of highly polar and charged species, which is applicable in the charge exchanges of interest. The method as described in Mroz et al. (2022) was followed, with the exception of using a dyall-v4z basis set for all calculations, as neither def2-TZVP nor aug-cc-pVTZ were available for radium, with all calculations done in ORCA [62][64][65]. To verify the relationship of vdW and STREUSEL-based radii with polarizability, the results of ab initio calculated polarizabilities for alkaline-earth monofluorides (AEMFs) were plotted as a function of various radii. The values for these differing radii are listed in Tables 6.7 and 6.8.

Table 6.7: Calculated dipole polarizabilities (a.u.) of alkaline earth metal fluorides (AEMF) using DF/QZ and KRCISD/QZ methods from Bala et al (2019). All values are in atomic units [56].

AEMF	**DF/QZ (a.u.)**	**KRCISD/QZ (a.u.)**	**Reference**
BeF	25.33	26.00	[56]
MgF	49.83	51.16	[56]
CaF	145.13	131.50	[56]
SrF	211.33	180.17	[56]
BaF	339.33	270.66	[56]
RaF	299.00	219.50	[56]

Table 6.8: Values of van der Waals (vdW) and STREUSEL radii (a.u.) calculated with CCSD/dyall-v4z for selected atomic and molecular species. Molecular vdW radii are computed as the sum of the atomic components. The vdW radii are from [61], and the STREUSEL radii were computed according to [62][63].

Species	**vdW Radius (a.u.)**	**STREUSEL Radius (a.u.)**
Be	2.89	3.6785
Mg	3.27	4.1024
Ca	4.37	4.7026
Sr	4.71	4.9139
Ba	5.06	5.2102
Ra	5.35	–
F	2.78	2.6598
Na	4.29	4.0298
BeF	5.67	3.8622
MgF	6.05	4.6905
CaF	7.14	5.0955
SrF	7.48	5.2755
BaF	7.84	5.4211
RaF	8.13	5.5078

Various techniques, including different combinations of van der Waals and STREUSEL radii, were applied to the molecules using DF/QZ and KRCISD/QZ methods, as shown in Figure 6.2 and Figure 6.3, respectively.

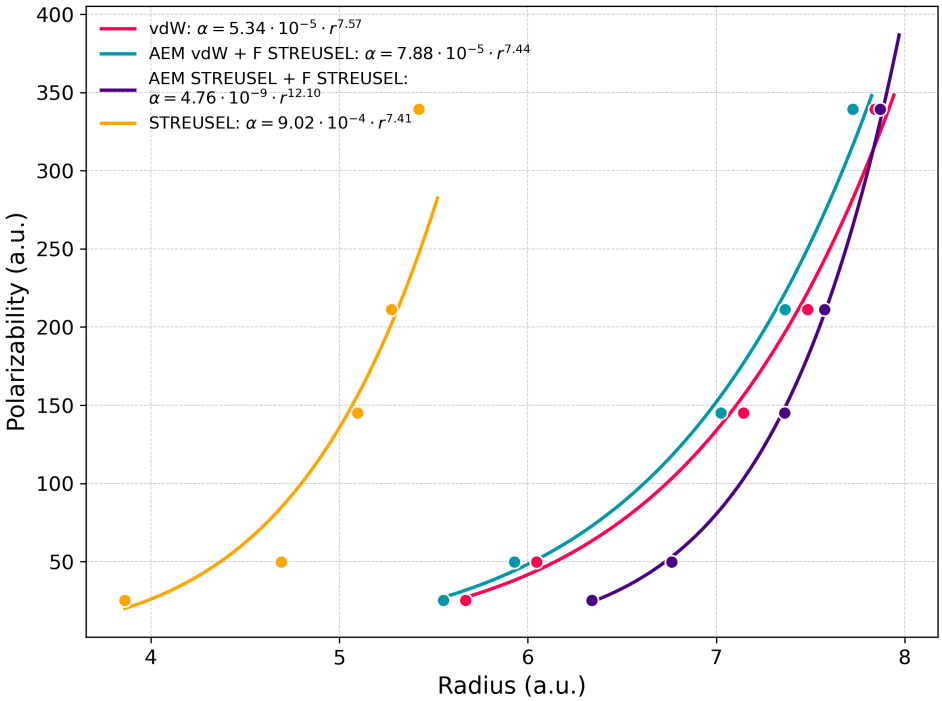

Figure 6.2: Polarizability of AEMFs using DF/QZ as a function of various radii.

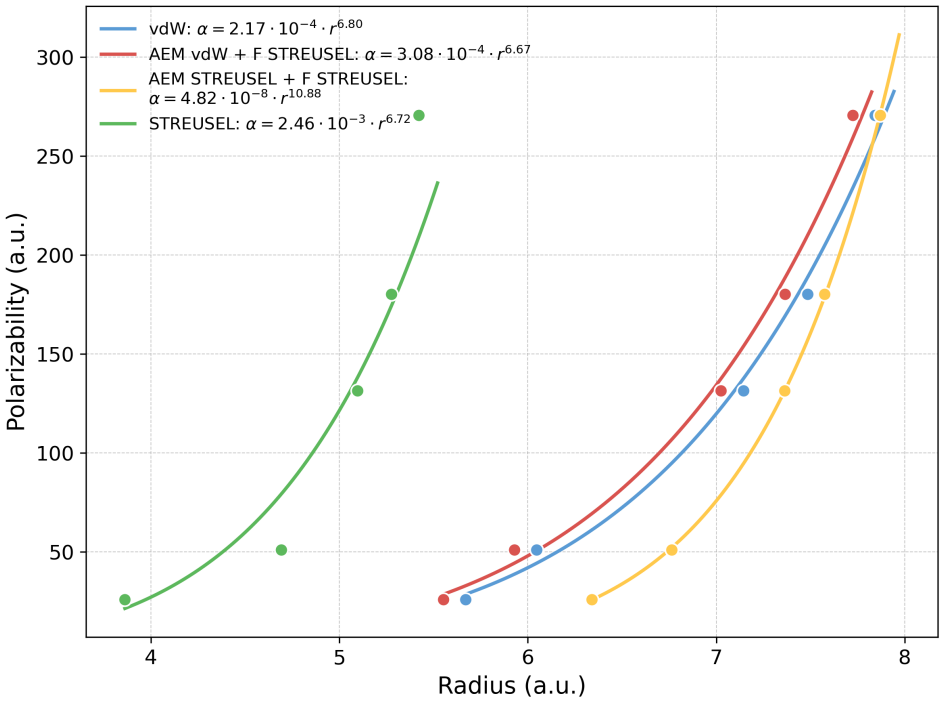

Figure 6.3: Polarizability of AEMFs using KRCISD/QZ as a function of various radii.

The predicted polarizability values for RaF are shown in Table 6.9.

Table 6.9: Predicted polarizabilities (a.u.) of RaF using fitted power-law models based on different effective radii. Van der Waals radii were summed for the individual atoms, with one method using the alkaline earth metal (AEM) vdW radius in combination with the STREUSEL radius of fluorine. Each cell lists the predicted value and its corresponding fit equation.

Radius Type	**Radius (a.u.)**	**DF Prediction (a.u.)**	**KRCISD Prediction (a.u.)**
STREUSEL only	5.5078	279.16 $\alpha = 9.02 \cdot 10^{-4} \cdot r^{7.41}$	234.59 $\alpha = 2.46 \cdot 10^{-3} \cdot r^{6.72}$
vdW	8.1258	412.32 $\alpha = 5.34 \cdot 10^{-5} \cdot r^{7.57}$	333.85 $\alpha = 2.17 \cdot 10^{-4} \cdot r^{6.80}$
AEM vdW + F STREUSEL	8.0077	415.56 $\alpha = 7.88 \cdot 10^{-5} \cdot r^{7.44}$	327.31 $\alpha = 3.08 \cdot 10^{-4} \cdot r^{6.67}$

To decide which radius type is needed to predict the polarizability of RaF^-, the effective radii can be compared for predicting the polarizability of RaF, using calculated values of AEMFs from DF/QZ and KRCISD/QZ. The fitted equations were used to find the predicted RaF polarizabilities. These projections are then compared against the calculated values of 219.5 a.u. for RaF (KRCISD/QZ) and 299 a.u. (DF/QZ). Table 6.10 summarizes the percent errors for each method and their average. It is important to note that the power fits in these models are relatively consistent with the relationship that has been established in the literature of $\alpha \propto R^7$ [81].

Comparing the tested radii models, the STREUSEL-only radius produced the lowest error. This contrasts with the vdW and AEM vdW + F STREUSEL models, which overestimated the polarizability for both, suggesting that vdW-based radii may not be well suited in the relationship of polarizability for heavy polar molecules like RaF. These findings support focusing on the STREUSEL-only radius results for predicting the polarizability of RaF^-.

Table 6.10: Percent error between predicted and true polarizabilities for RaF using different effective radii. Errors are computed for both DF and KRCISD predictions, with the average shown for each model.

Radius Type	**DF % Error**	**KRCISD % Error**
STREUSEL only	6.6354	6.8747
vdW	37.8997	52.0957
AEM vdW + F STREUSEL	8.9833	49.1162

Now that a correlation has been shown for AEMFs radii models and polarizability, the same

technique was done for the anions. Limited calculations were available, with only BeF^- and MgF^- having values for the anionic polarizability. The Møller–Plesset perturbation theory calculations in Table 6.11 were used to obtain relationships between the anionic polarizability and various radii as shown in Figure 6.4 [59].

Table 6.11: Van der Waals and STREUSEL radii (a.u.) for selected atomic and anionic species. Van der Waals radii are from [61], and the STREUSEL radii are computed according to [62][63].

Species	**Radius Type**	**Radius (a.u.)**
Be	vdW	2.89
Mg	vdW	3.27
F	vdW	2.78
Ra	vdW	5.35
F^-	STREUSEL	5.2213
BeF^-	STREUSEL	3.9406
MgF^-	STREUSEL	4.6544
RaF^-	STREUSEL	5.5874

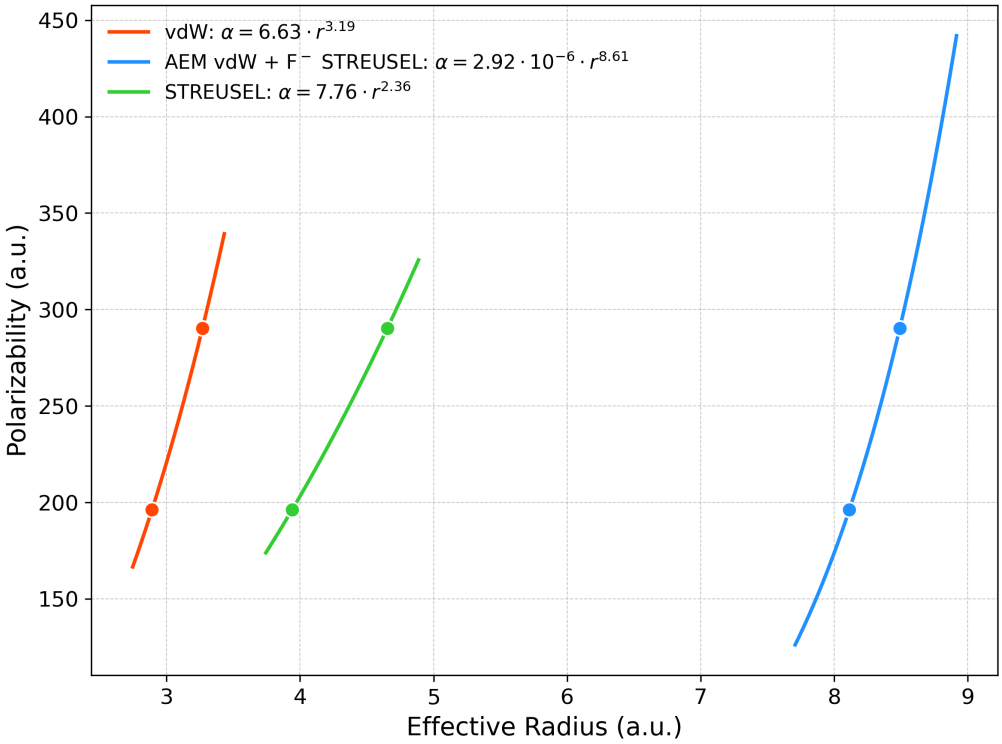

Figure 6.4: Polarizability scaling of anions using Møller–Plesset perturbation theory and B2PLYP with the aug-cc-pVTZ basis set and FULL ultrafine integration grid. The effective radii methods were vdW (adding the vdW radii of the alkaline earth metal and neutral fluoride), adding the alkaline earth metal vdW radius to the STREUSEL calculated F^- radius, and the STREUSEL calculated radius for the anionic molecule.

From the fitted correlations from BeF^- and MgF^-, the polarizability of RaF^- can be extrapolated according to its radius under each model. For the vdW radius (Ra + F), the predicted polarizability is extremely large with $\alpha_{RaF^-} \approx 5296.52$ a.u. Using the AEM vdW + STREUSEL(F^-) radius, the prediction increases to $\alpha_{RaF^-} \approx 1916.16$ a.u. Whereas using the STREUSEL-calculated radius gives an estimated polarizability that is significantly lower at $\alpha_{RaF^-} \approx 450.06$ a.u. Despite the STREUSEL method varying the least for the neutral molecules, it is lower than expected, as it is within the range of RaF polarizabilities. The AEM vdW + STREUSEL seems to be more promising for the anions as its power-fits align more with the expected relationship of $\alpha \propto R^7$ [81].

Now that there are estimates for the polarizability of RaF^-, the critical distance can be found from the EEP

$$-\frac{\alpha_{\mathrm{Na}}}{R^4} = \mathrm{IP}(\mathrm{Na}) - \mathrm{IP}(\mathrm{RaF}^-) - \frac{1}{R} - \frac{\alpha(\mathrm{Na}^+) + \alpha(\mathrm{RaF}^-)}{2R^4} \tag{6.16}$$

and the IT

$$\mathrm{IP}(\mathrm{RaF}^-) - \mathrm{IP}(\mathrm{Na}) = \mathrm{IP}(\mathrm{Na}) - \mathrm{IP}(\mathrm{RaF}^-) - \frac{1}{R} - \frac{\alpha(\mathrm{Na}^+) + \alpha(\mathrm{RaF}^-)}{2R^4} \tag{6.17}$$

Using the values from Table 6.2 and Table 6.3, the critical distance can be found in both EEP and IT methods using the predicted RaF^- polarizabilities of 5296.52 a.u., 1916.16 a.u., and 450.06 a.u. The geometrical cross section can then be computed, with these results shown in Table 6.12.

Table 6.12: Comparison of EEP and IT models for different RaF^- polarizabilities at 585 K.

Method	α_{RaF^-} **(a.u.)**	R **(a.u.)**	σ **(a.u.^{2})**
EEP	5296.52	15.4076	745.7957
EEP	1916.16	12.3617	480.0719
EEP	450.06	8.9681	252.6655
IT	5296.52	12.3087	475.9642
IT	1916.16	9.7773	300.3163
IT	450.06	7.1520	160.6973

Massey Adiabaticity Criterion

Although it is not a method to obtain the critical distance or cross section, the Massey adiabaticity criterion does define the projectile energy at which the charge exchange cross section is maximized for asymmetrical charge transfers [82]. The Massey criterion is based on the adiabaticity parameter

$$\eta = \frac{a|\Delta E|}{\hbar v}, \tag{6.18}$$

where a is the interaction distance, ΔE is the change in energy for the reaction, v is relative velocity, and $\hbar$ is the reduced Planck constant. When $\eta \gg 1$, the collision is relatively slow, and the electronic wavefunction has enough time to adjust. As a result, the system evolves adiabatically. When $\eta \ll 1$, the projectile velocity is very fast and the electronic state does not have enough time to change. The charge exchange cross section is maximized when $\eta \approx 1$, as the transition time and collision time are comparable.

When the electronic transition time is approximately equal to the collision time, these two timescales can be set equal. Solving this condition yields the velocity at which charge transfer is optimized

$$v_{\max} = \frac{a|\Delta E|}{\hbar}. \tag{6.19}$$

This criterion has been looked into in the context of a double charge exchange [83]. As there are two ΔE values for a double charge exchange, Alton (2005) defines the second exchange as the dominant process [84]. This allows for the estimation of the velocity at which the cross section for the second exchange is maximized for a specific distance

$$E_{1,\mathrm{MAX}} = 8.31 \times 10^{-3} \cdot M_1 \cdot (a \cdot \Delta E_2)^2 \tag{6.20}$$

where $E_{1,\mathrm{MAX}}$ is the projectile energy in keV, M_1 is the mass of RaF in amu, a is the interaction distance in Å, and ΔE_2 is the change in energy for the second charge exchange in eV. The charge exchange of $\mathrm{RaF} + \mathrm{Na} \rightarrow \mathrm{RaF}^- + \mathrm{Na}^+$ has a maximum cross section at an interaction distance of 1.706 a.u. at 29.935211 keV as shown in Figure 6.5.

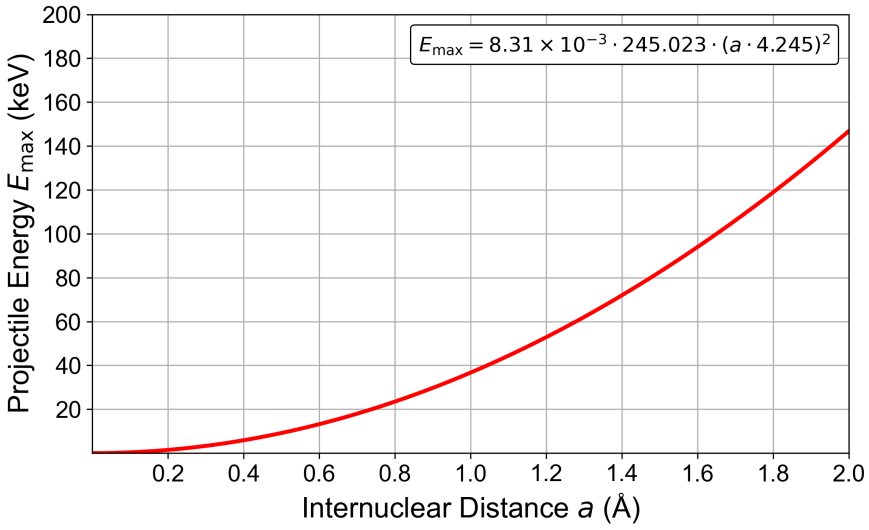

Figure 6.5: Depiction of maximum projectile energy as a function of internuclear distance according to the Massey adiabaticity criterion, which predicts maximum charge exchange when the timescales for nuclear motion and electronic transitions are comparable. The plot is specifically for RaF in a charge exchange with Na.

This result aligns with the results in the second charge transfer, as the optimal distance is within

the critical distance for all models. Despite having to assume that if within the critical distance, charge exchange occurs with a 100% probability within the critical radius, the Massey criterion gives a useful estimate of the distance at which the transition probability is maximized.

6.3 Summary of Second Charge Exchange Results

The results in Table 6.13 show to be relatively similar to those of the first charge exchange in Table 5.11.

Table 6.13: Comparison of second charge exchange models crossing distance R and cross section σ. The cross sections were calculated at 585 K.

Model	R **(a.u.)**	σ **(a.u.^{2})**
Hard Sphere	9.7975	301.5630
HKL	6.4101	129.0861
Kimura	5.4592	93.6285
Dissociation (EEP, $\alpha = 5296.52$)	15.4076	745.7957
Dissociation (EEP, $\alpha = 1916.16$)	12.3617	480.0719
Dissociation (EEP, $\alpha = 450.06$)	8.9681	252.6655
Dissociation (IT, $\alpha = 5296.52$)	12.3087	475.9642
Dissociation (IT, $\alpha = 1916.16$)	9.7773	300.3163
Dissociation (IT, $\alpha = 450.06$)	7.1520	160.6973

The second charge exchange was expected to have lower cross sections due to the neutral-neutral interaction. It is worth noting that the highest realistic cross section from the IT locked dipole in the first charge exchange is higher than any of the results of the second exchange. The hard sphere model is lower for the second exchange than from the first, attributed to the smaller STREUSEL size of RaF compared to RaF^+. The highest cross section is from the dissociation model EEP method from a RaF^- polarizability of 5296.52 a.u., which is not expected to be realistic. The Hubers-Kleyn-Los and Kimura models yield the lowest cross sections of all approaches. This is due to both models focusing on long-range weak interactions. The majority of the models for the second exchange fall in the range 93.6285-480.0719 a.u.^{2}.

Chapter 7

Experimental Results

As mentioned previously, the experiment ran at ISOLDE during the winter physics period, and data were collected during each scan.

7.1 Average Voltage

The experimental parameters were set to accelerate the RaF^+ beam from ISCOOL at 30 keV. To get a precise value to input into all of the models, the average voltage was found across scans when RaF^- was produced, along with the standard deviation to see how the voltage varies.

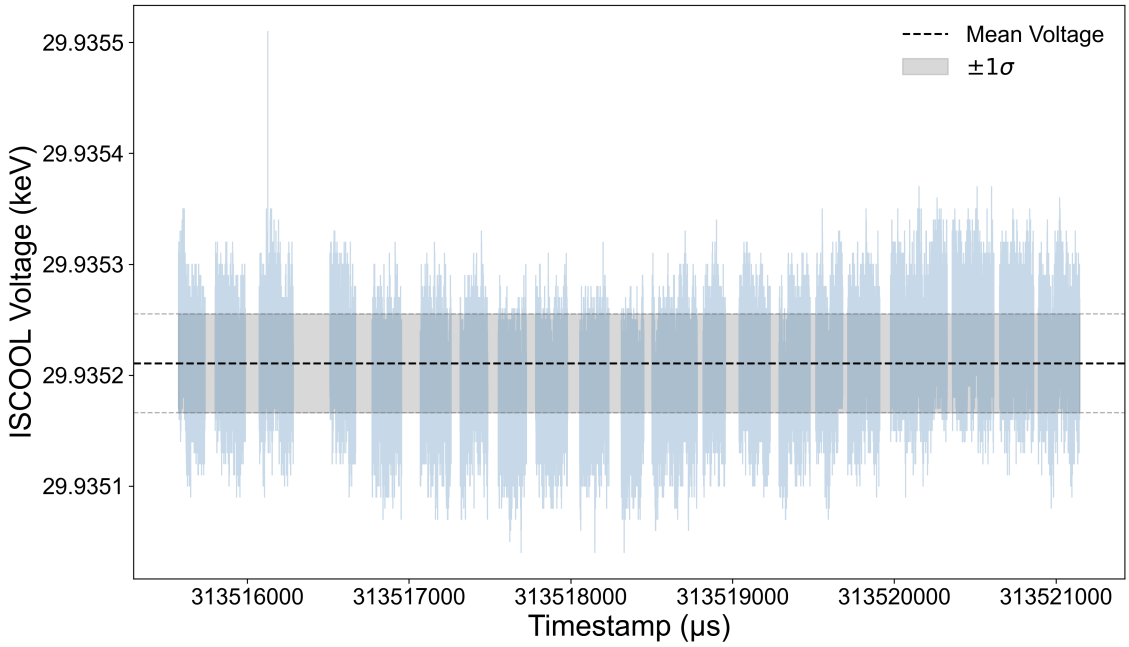

Figure 7.1: Overlay of ISCOOL voltages across scans 3013-3034 (scans where RaF^- was produced) is plotted in steel blue. The dashed line shows the mean voltage, and the shaded region represents one standard deviation.

Figure 7.1 shows that the average energy across the scans is $29,935.2 \pm 0000.04$ eV, and this is the value used in all the first and second charge exchange models.

7.2 Faraday Cup

There are multiple Faraday cups (FC) in the experimental setup, one of focus for finding how much of the RaF^+ beam is converted to RaF^- is the one located after ISCOOL. The Faraday cup blocks the beam, so measurements are taken periodically to get the current. Right before scan 3130 was taken (the scan that plotted RaF^- counts vs CEC temperature), the FC was inserted into the beamline. There is a dip in this stable region that is excluded from the mean and standard deviation. A zoomed-in version of this region and the exclusion are depicted in Figure 7.2.

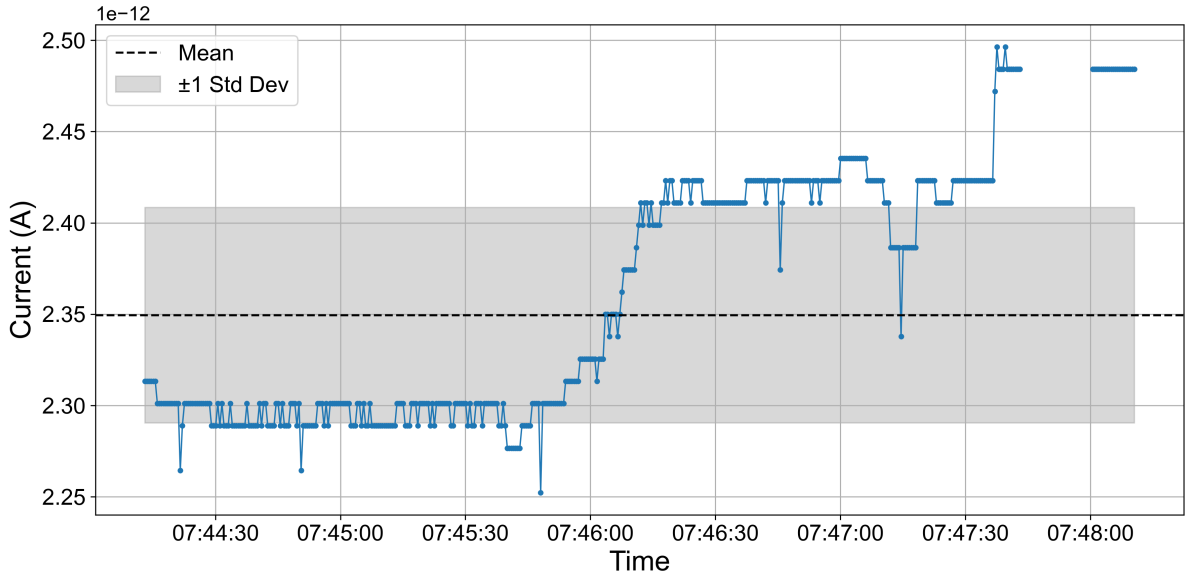

Figure 7.2: Stable current region recorded by the Faraday cup after ISCOOL.

From this data, the mean of the RaF^+ current is $2.349 \pm 0.059 \times 10^{-12}$ A.

7.3 MagneToF

As the MagneToF measures the negative ion count produced from the CEC, it is important to find the RaF^- counts per second for efficiency calculations. Results are plotted in Figure 7.3.

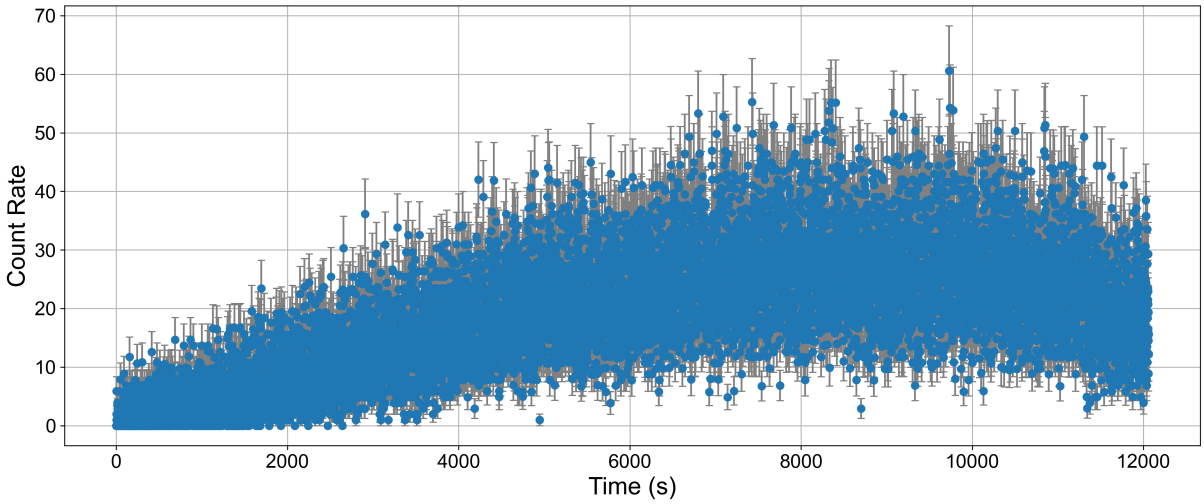

Figure 7.3: Count rate versus time on the MagneToF for scan 3130. Time bin is one second.

Figure 7.3 can be used to determine the maximum count rate per second, which is found to be 60.58 ± 7.69 counts/s at 9729.01 s. The associated error is the square root of the number of counts from a Poisson distribution. The MagneToF count rate per ion bunch is plotted in Figure 7.4 against the thermocouple center temperature in Celsius.

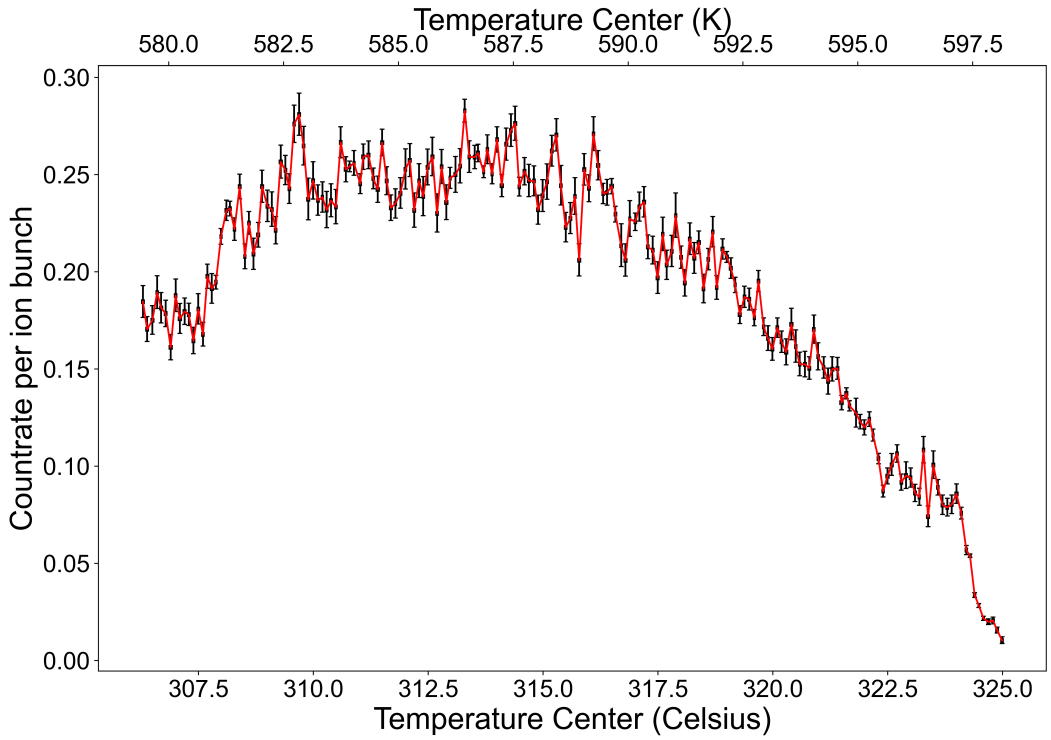

Figure 7.4: Experimental count rate of RaF^- as a function of temperature for scan 3130. The temperature bin is 0.1 Celsius.

Chapter 8

Efficiency Calculations

Now that cross sections have been evaluated using different models for both the first and second charge exchange, and experimental data have been introduced, the predicted efficiencies from the models can be compared with those observed experimentally.

8.1 First Charge Exchange Efficiency

The neutralization efficiency of charge transfer is related to the charge exchange cross section by

$$\epsilon = 1 - \exp(-\sigma n l) \tag{8.1}$$

where n is the Na vapor density and l is the path length of the CEC [85]. The analytical cross sections for the first charge exchange are in Table 5.11, and the path length of the CEC was introduced in Figure 3.3 to be 19 cm. The sodium vapor pressure in pascals can be obtained from

$$\log_{10}\left(\frac{p}{\mathrm{Pa}}\right) = 5.006 + A + \frac{B}{T}, \tag{8.2}$$

A and B are parameters for sodium [86]. The number density of sodium is calculated by

$$\rho(T) = \frac{p(T)}{k_B T} \tag{8.3}$$

and the vapor pressure as a function of temperature is shown in Figure 8.1.

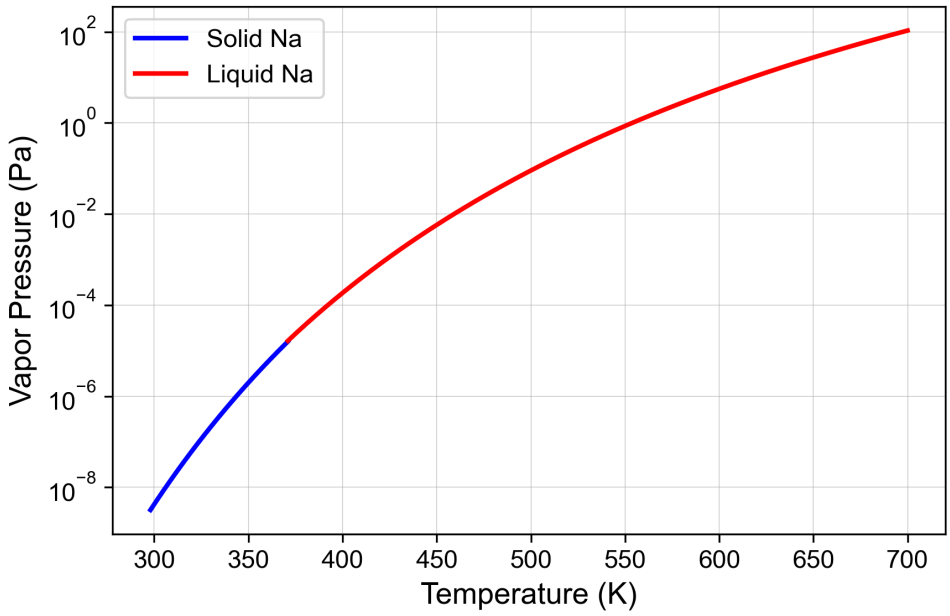

Figure 8.1: Vapor pressure of sodium in the solid and liquid phases as a function of temperature. Adapted from [87].

For the sake of consistent units, the cross sections from Table 5.11 are shown below with cm^2.

Table 8.1: Comparison of first charge exchange cross sections at $T = 585$ K.

Model	σ **(a.u.^{2})**	σ **(cm^2)**
Hard Sphere	326.5355	9.144×10^{-15}
Langevin	5.8643	1.642×10^{-16}
Extended Langevin	0.967–1.324	$(2.708–3.708) \times 10^{-17}$
Locked Dipole (EEP)	116.4701	3.261×10^{-15}
Locked Dipole (IT)	599.3544	1.678×10^{-14}
ADO (EEP)	491.3838	1.376×10^{-14}
ADO (IT)	411.5346	1.152×10^{-14}
AADO (EEP)	193.3804	5.415×10^{-15}
AADO (IT)	405.1843	1.135×10^{-14}
Temp.-Dep. ADO (EEP)	2959.1602	8.286×10^{-14}
Temp.-Dep. ADO (IT)	366.1632	1.025×10^{-14}

Using the number density as a function of temperature, the efficiency of neutralization can be found to vary by

$$\epsilon(T) = 1 - \exp\left(-\sigma \cdot \frac{p(T)}{k_B T} \cdot l \cdot 10^{-6}\right), \tag{8.4}$$

The efficency is plotted as a function of temperature in Figure 8.2.

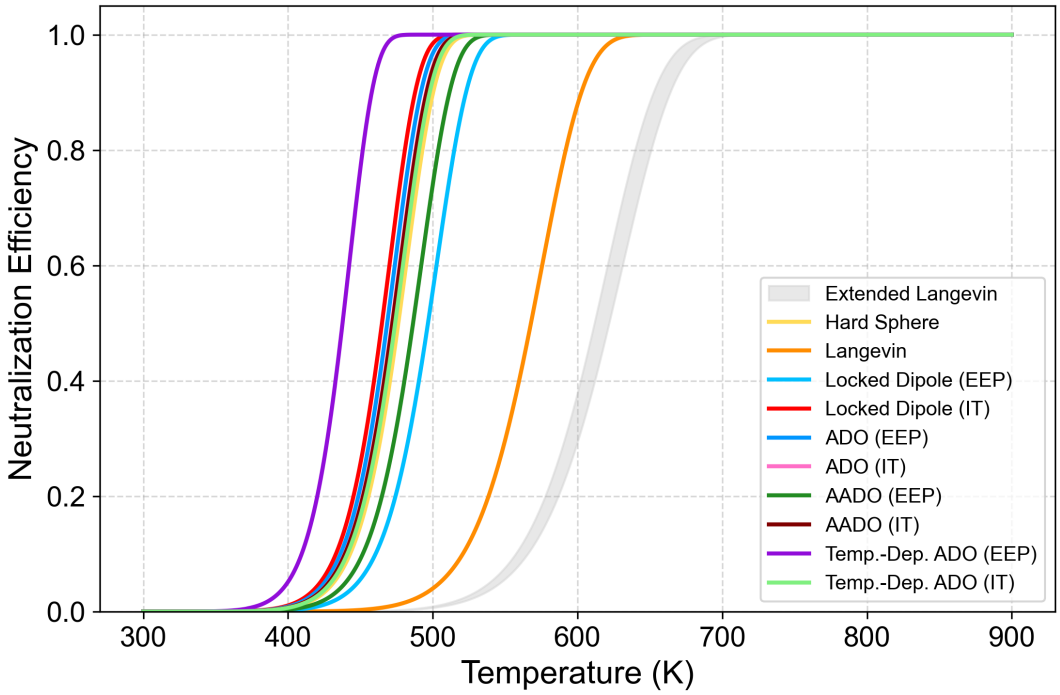

Figure 8.2: Neutralization efficiency as a function of temperature for analytical first charge exchange models. The shaded gray band indicates the range of predictions from the Extended Langevin model from various polarizabilities.

This efficiency distribution is extremely high, suggesting 100% neutralization is possible for the various models at a certain temperature. This is not realistic as this calculation assumes equal temperature distribution in the CEC, and therefore uniform sodium density throughout. To get the average sodium atoms/cm^2 for a cell that does not have uniform vapor density, it can be obtained by integrating the density by path length [88]

$$\overline{nl} = \int n\, dl \tag{8.5}$$

For a closer representation of the temperature profile inside the CEC, a parabolic distribution is assumed. The temperature along a cell length of 19 cm is

$$T(x) = a\left(x - \frac{L}{2}\right)^2 + T_{\text{center}} \tag{8.6}$$

where x is the position in the cell (0-19 cm), T_{center} is the temperature in the center of the CEC (8 cm), and a is a parameter for the distribution.

To find a, experimental data can be utilized to get an idea of how the temperature in the center and ends differ. The temperature from the thermocouple ends is related to the thermocouple center temperature collected in scan 3130. A linear fit gives

$$T_{\text{ends}} = m \cdot T_{\text{center}} + b \tag{8.7}$$

with experimentally fitted parameters $m = 0.146$ and $b = 53.4\,^{\circ}\text{C}$.

Using this relation, a can be expressed as

$$a = \frac{T_{\text{ends}} - T_{\text{center}}}{(L/2)^2} = \frac{(m-1)T_{\text{center}} + b}{(L/2)^2} \tag{8.8}$$

So, the full equation for the temperature gradient for a sodium vapor filled CEC with a length of 19 cm in Celsius is

$$T(x) = \left[\frac{(0.145761 - 1) \cdot T_{\text{center}} + 53.402456}{(19/2)^2}\right] \left(x - \frac{19}{2}\right)^2 + T_{\text{center}} \tag{8.9}$$

This temperature gradient throughout the length of the CEC, depending on the temperature of the center thermocouples, is depicted in Figure 8.3.

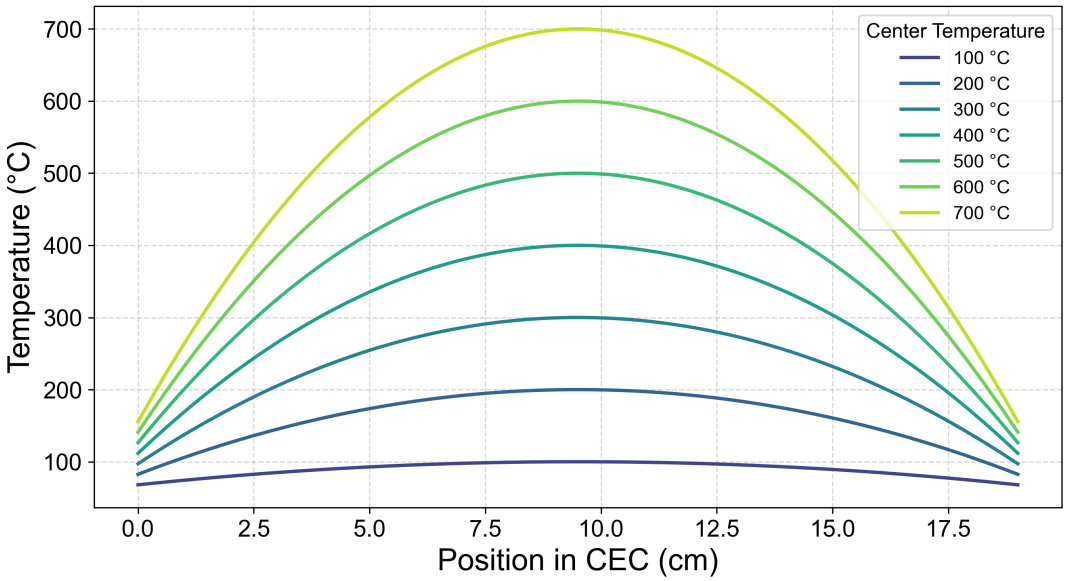

Figure 8.3: Parabolic temperature profiles in the CEC for different center temperatures. The parameters used are from experimental fits of thermocouple data in scan 3130.

Using this experimental distribution, the average sodium atom density (atoms/cm^2) along the 19 cm charge exchange cell length can be calculated as a function of the center temperature. The efficiency curves for a nonuniform temperature gradient are shifted towards higher temperatures in Figure 8.4 compared to Figure 8.2 as there is a lower density for a certain temperature using the non-uniform model.

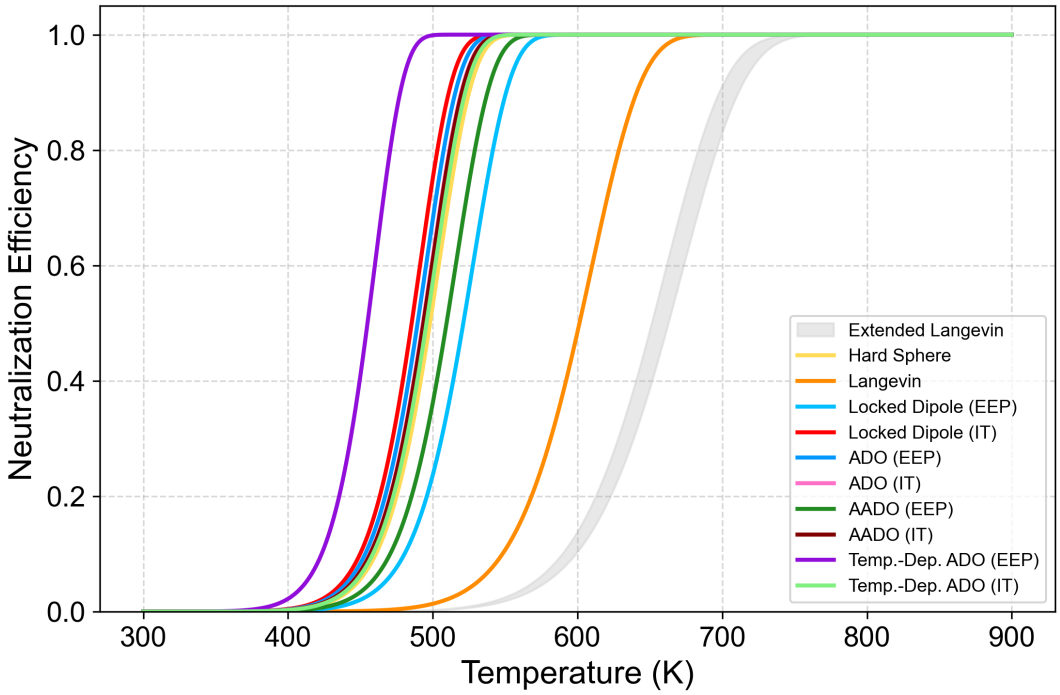

Figure 8.4: Neutralization efficiency using the non-uniform temperature distribution inside the CEC.

8.2 Second Charge Exchange Efficiency

The second exchange can only take place after one occurs, so this is a dependent event, and it is not as straightforward as multiplying the probabilities. The efficiency of a single charge exchange process in Equations 8.1 and 8.5 for non-uniform vapor density is used along with the logic that the second charge exchange can only occur at a time after the first. This rationale serves as the grounds that the probability of producing RaF^- is to be computed by integrating over the possible positions of the CEC where the first exchange may occur, while also accounting for the non-uniform sodium vapor density. The double charge exchange probability is then given by

$$P_{\text{double}} = \int_0^l n(x)\sigma_1 \, e^{-\int_0^x n(s)\sigma_1 \, ds} \left(1 - e^{-\int_x^l n(s)\sigma_2 \, ds}\right) dx \tag{8.10}$$

where the term $n(x)\sigma_1$ is the rate of the first charge exchange at position x, and the exponential factor is a Poisson survival probability, describing the probability that the first charge exchange has not occurred anywhere along the cell length. The second term in parentheses gives the probability that the second charge exchange occurs at a point after, between x and the end of the CEC, l. This integral is an attempt to capture the successive and spatially dependent nature of the double charge exchange process. The resulting dependent double charge exchange

probabilities as a function of the center temperature of the CEC are shown in Figure 8.5.

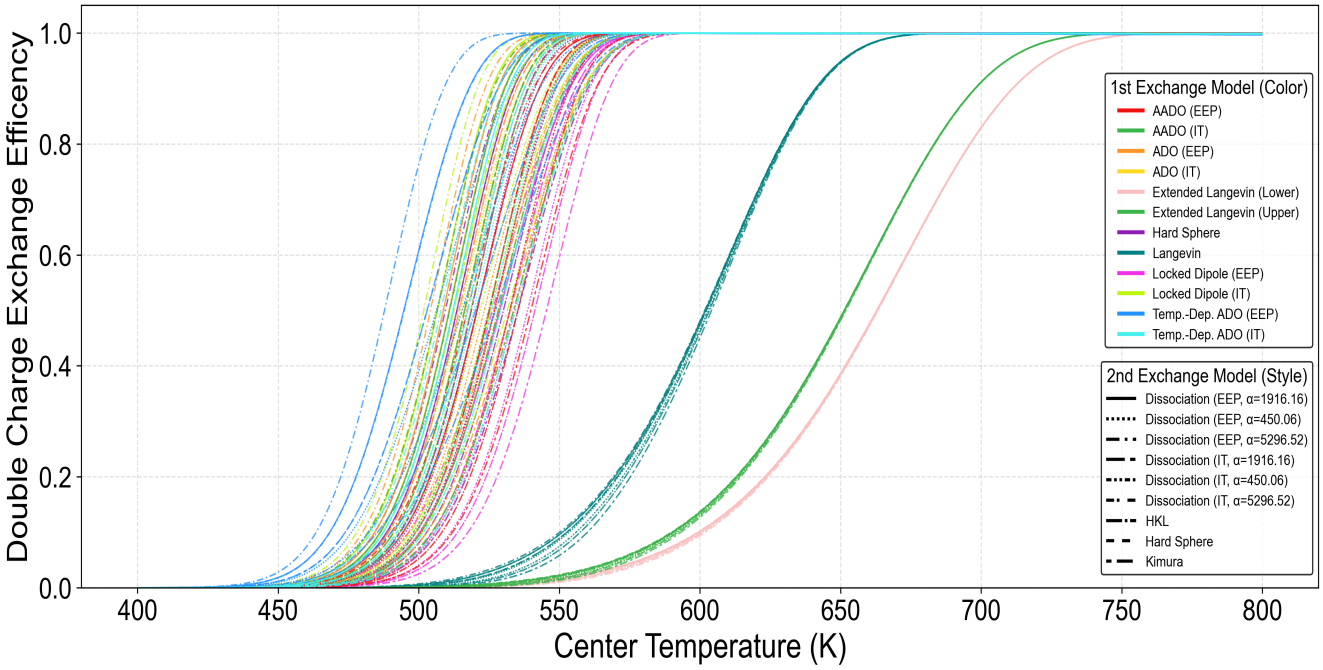

Figure 8.5: Dependent double charge exchange efficiency versus center temperature for various model combinations of the first and second charge exchange cross sections. The efficiency was found using Equation (8.10).

8.3 Experimental Efficiency

The experimental results can be used to find the efficiency of RaF^- as a function of temperature. The average Faraday cup current of RaF^+ taken before scan 3130 is $2.349 \pm 0.059 \times 10^{-12}$ A. The counts can be found from this current by dividing by the elementary charge, which gives $0.467 \pm 0.037 \times 10^7$ ions/s. The amount converted to RaF^- is found by dividing the count rate measured on the MagneToF by the ion rate measured by the Faraday Cup, and the efficiency is plotted as a function of temperature inside the CEC in Figure 8.6.

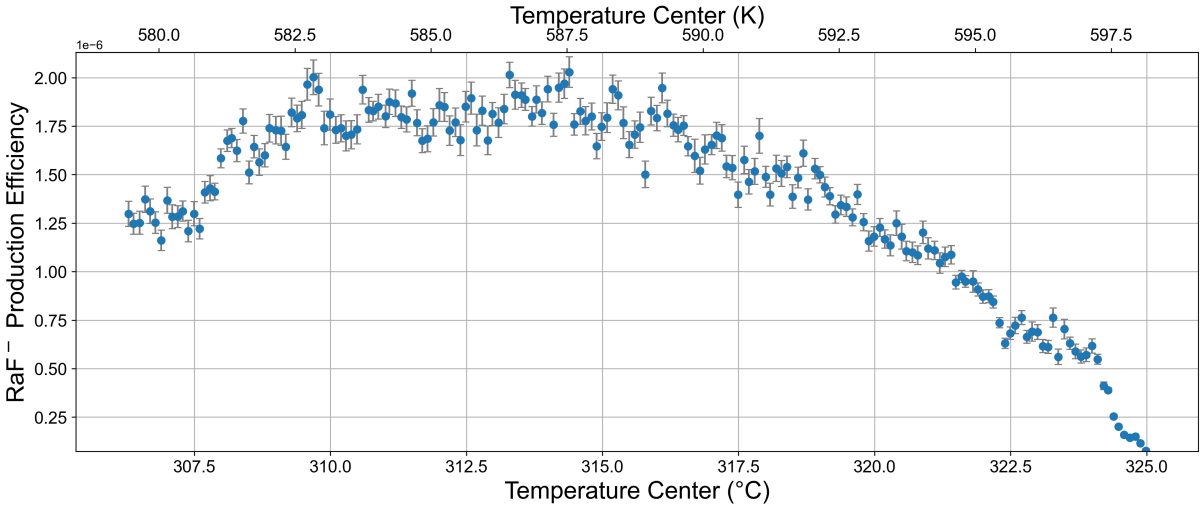

Figure 8.6: Experimental RaF^- production efficiency as a function of CEC temperature for scan 3130. The efficiency is computed as the ratio of RaF^- count rate to RaF^+ ion rate from the Faraday cup.

The maximum experimental efficiency for RaF^- production is $2.03 \pm 0.38 \times 10^{-6}$ at $314.39°C$ (587.54 K).

8.4 Comparison of Models and Experimental

Despite errors in capturing the temperature distribution inside the cell along with many different representations of the cross sections of the two exchanges, the analytical model is not in line with the experimental results. As seen in Figure 8.6, there is a peak efficiency at a specific CEC center temperature, with the efficiency falling off outside the optimal range. This is not the case with the equation used to calculate efficiency analytically

$$\epsilon = 1 - \exp(-\sigma n l), \tag{8.11}$$

As the efficiency rises drastically with temperature. This increase could be counteracted with a cross section temperature dependence that decreases at higher temperatures, but all the cross sections modeled were not able to encompass this as they did not vary significantly with changing temperatures. It is important to note that in typical ISOLDE experiments, roughly 30–50% of the beam is lost, so the efficiency would realistically range from $(2.90–4.06) \times 10^{-6}$. The optimal temperature defined by the experiment (587.41 K) was used to extract the efficiency from the analytical models, and the temperature where the efficiency would match the highest from the experiment was found. These comparisons are shown as a heatmap in Figures 8.7 and 8.8.

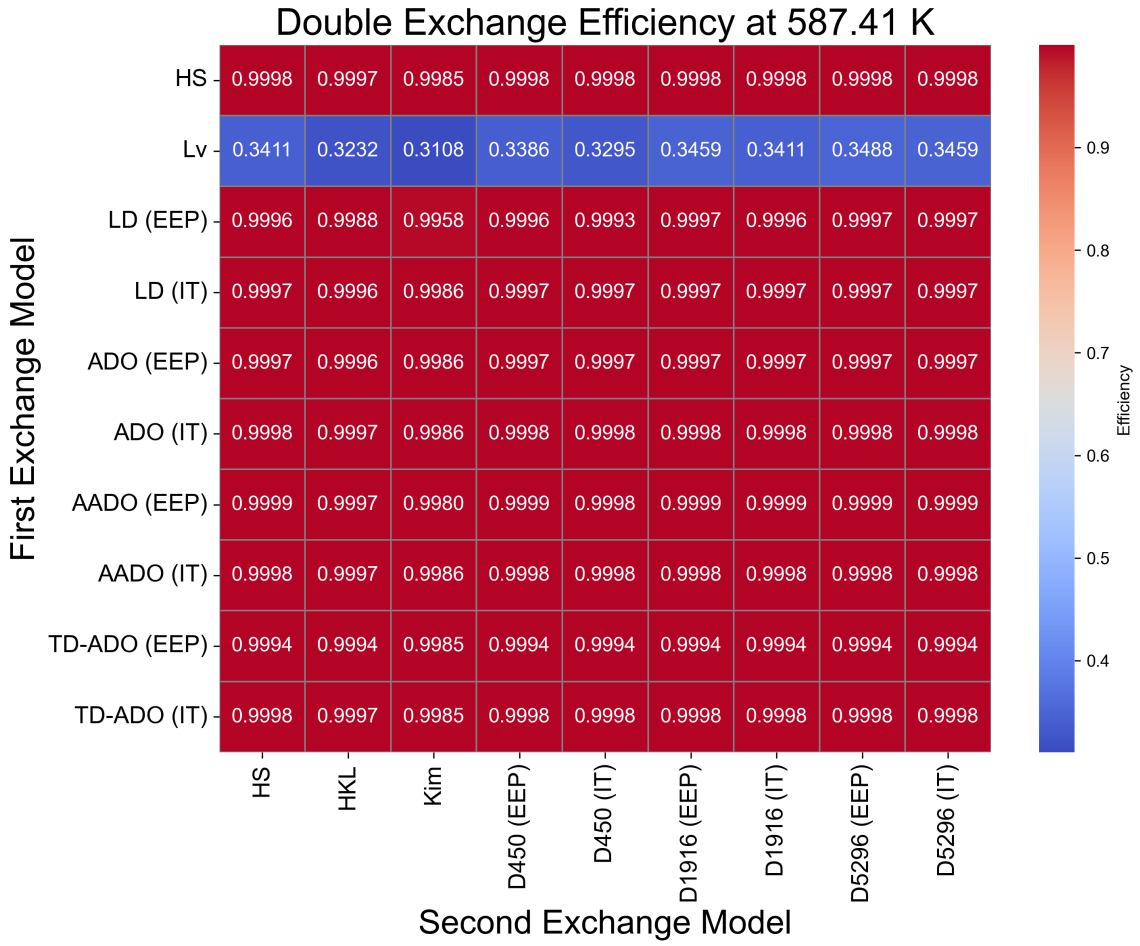

Figure 8.7: Double charge exchange probability at 587.41 K for each model combination.

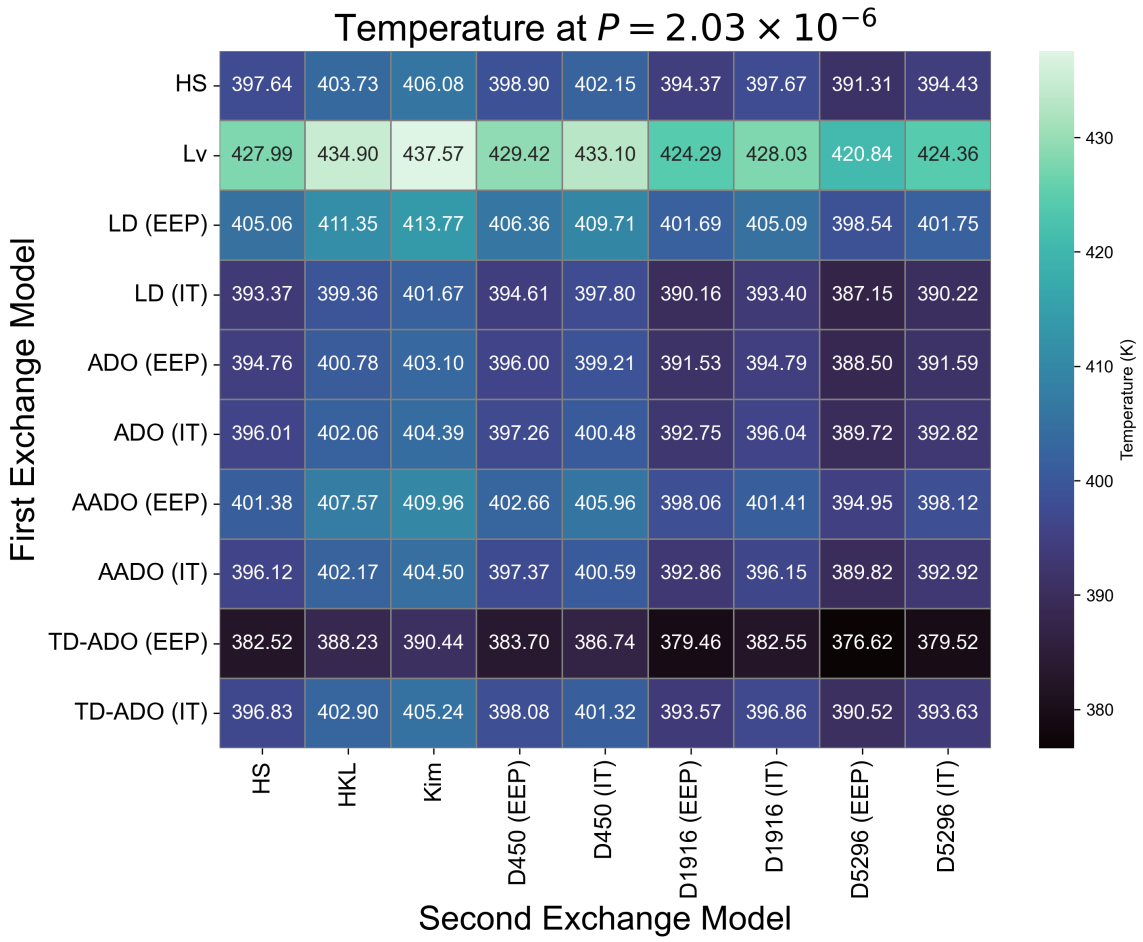

Figure 8.8: Temperature required to reach a double charge exchange probability of $P = 2.03 \times 10^{-6}$ for each model combination.

The efficiency from the models at the optimal RaF^- temperature is very high for most combinations, up to 0.9999, which clearly is not realistic and exhibits the weakness of the model where temperature steeply increases the efficiency. Additionally, the temperature that matches the highest experimental production is much cooler than the 587.41 K CEC temperature from the experiment. There was expected to be a mismatch between the experimental efficiency and the models as the models overestimate the probability of exchange before the critical distance, and do not exhibit a temperature dependence that could decrease the cross sections at higher temperatures. However, although the magnitude cannot be predicted, the trend of the probability curve can be used to find a temperature window to serve as a guide for the temperatures to scan in further experiments.

When examining Figure 8.5, it is clear that most of the model combinations start to exhibit efficiency increases in the range of 450-575 K. Based on these trends, the temperature windows for an efficiency threshold of 0.75-0.99 can be analyzed. Of the 108 possible model combinations, 81 models had temperature windows that started below 600 K for the threshold. To find the models that best matched the experimental results, the top fifteen were filtered by finding the closest temperatures where 0.99 efficiency was reached compared to the experimental

587.41 K result. The combinations that meet this requirement are shown in Figure 8.9.

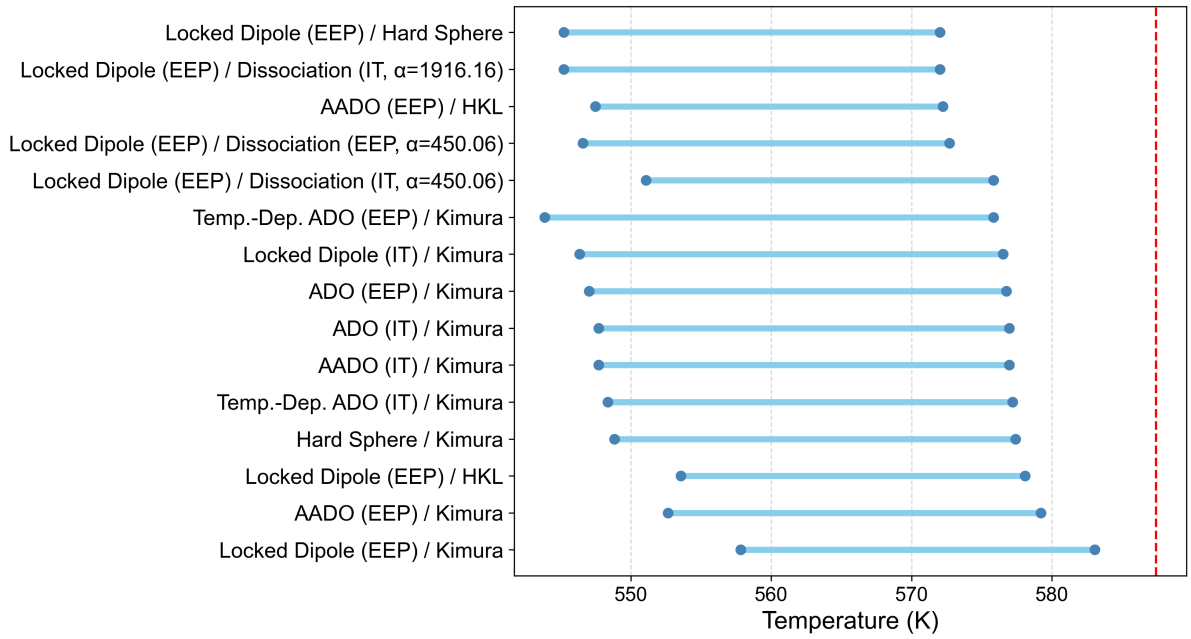

Figure 8.9: Model combinations that are closest in temperature at 0.99 efficiency to that of the target 587.41 K. The dashed red line labels the target experimental temperature. The first charge exchange model is listed first, followed by the second charge exchange model.

Given these results and the knowledge of how each model was obtained, the first charge exchange model that appears the most frequently is the locked dipole using the EEP method. As stated in Chapter 5, the EEP method was predicted to give more accurate results compared to the IT method for a given model, with the exception of the temperature-dependent ADO. The majority of the closest 15 models use the EEP method, which corroborates the projection. The model that is the most prevalent in the top fifteen for the second exchange is the Kimura model, which describes the interaction between two neutrals as a long-range polarizability potential prior to the reaction and with a Coulombic attraction after the ion-pair formation. The locked dipole (EEP) and Kimura combination had the closest temperature of 583.04 K to the experimental result of 587.35 K when at 0.99 efficiency.

Chapter 9

Conclusions

This thesis sought to elaborate on the efficiency of RaF^- production to find a way to predict optimal temperatures inside the charge exchange cell (CEC) prior to an experimental run, to know which range to focus on. Many models were used to predict cross sections for the first and second exchange, and with those, the RaF^+ dipole moment was predicted as well as ranges for the polarizability of RaF and RaF^-. While the majority of models yielded consistent results, a key limitation is the assumption that charge exchange will occur once the sodium vapor and RaF species are within a critical distance of each other. This simplification significantly overestimates the cross section and fails to capture the full behavior of the system in the absence of ab initio calculations. This assumption neglects any considerations such as non-adiabatic transitions, electronic state couplings, and Franck–Condon overlap, all of which play roles in this reaction and also could result in cross sections decreasing at higher temperatures. This discrepancy underscores the limitations of using classical or semi-classical models for such a complex reaction and suggests that more sophisticated treatments are necessary to predict negative ion production that matches experimental results. Despite such an overestimation of the cross section, optimal temperature values were identified in agreement with experimental results by focusing on the peak efficiency temperatures of the analytical models as opposed to their magnitudes. The locked dipole model with an exit-entrance potential (EEP) method to find the critical distance emerged as the most prominent of the first charge exchange models. For the second exchange, the Kimura model was the most prevalent, describing the neutral-neutral interaction by long-range polarizability prior to charge exchange and Coulombic attraction afterwards. The model that best agrees with the experimental optimal efficiency temperature of 587.41 K was the locked dipole(EEP) with Kimura combination. This combination reached 0.99 efficiency at 583.04 K, a 4.37 K difference from the experimental results.

Future work could focus on computing charge exchange cross sections using ab initio methods for simpler systems such as CaF, providing valuable benchmarks for validating analytical models. Although classical and semi-classical approaches tend to overestimate absolute cross sections, the models presented in this thesis are promising for predicting the optimal temper-

ature for RaF^- production, and can provide a benchmark for temperature scans. These predictions align with experimental data when evaluated in terms of temperature sensitivity rather than magnitude, serving valuable qualitative guidance.

The experimental campaign at ISOLDE provided crucial benchmarks for theory, enabling the first direct comparison between modeled and measured RaF^- yields under controlled thermal CEC conditions. These results emphasize the need for continued refinement of model parameters and a deeper understanding of CEC dynamics. Such efforts are essential for advancing the broader application of cold molecular ions in precision measurement experiments.

Bibliography

[1] Hai-Yang Cheng. The strong CP problem revisited. *Physics Reports*, 158(1):1–89, Jan 1988.

[2] V. Spevak, N. Auerbach, and V. V. Flambaum. Enhanced T-odd, P-odd electromagnetic moments in reflection-asymmetric nuclei. *Physical Review C*, 56(3):1357–1369, September 1997.

[3] Tanya S. Roussy, Luke Caldwell, Trevor Wright, William B. Cairncross, Yuval Shagam, Kia Boon Ng, Noah Schlossberger, Sun Yool Park, Anzhou Wang, Jun Ye, et al. An improved bound on the electron's electric dipole moment. *Science*, 381(6653):46–50, July 2023.

[4] Yohei Ema, Ting Gao, and Maxim Pospelov. Standard model prediction for paramagnetic electric dipole moments. *Phys. Rev. Lett.*, 129:231801, Nov 2022.

[5] M. G. Kozlov and L. N. Labzowsky. Parity violation effects in diatomics. *Journal of Physics B: Atomic, Molecular and Optical Physics*, 28(10):1933–1961, May 1995.

[6] P.A. Butler, L.P. Gaffney, P. Spagnoletti, K. Abrahams, M. Bowry, J. Cederkäll, G. de Angelis, H. De Witte, P.E. Garrett, A. Goldkuhle, et al. Evolution of octupole deformation in radium nuclei from coulomb excitation of radioactive ^{222}Ra and ^{228}Ra beams. *Physical Review Letters*, 124(4), January 2020.

[7] Konstantin Gaul, Ronald F. Garcia Ruiz, and Robert Berger. Stopping mass-selected alkaline-earth metal monofluoride beams of high energy via formation of unusually stable anions, May 2024. arXiv:2403.09320.

[8] Ronald F. Garcia Ruiz, Robert Berger, J. Billowes, C. L. Binnersley, M. L. Bissell, A. A. Breier, A. J. Brinson, K. Chrysalidis, T. E. Cocolios, B. S. Cooper, et al. Spectroscopy of short-lived radioactive molecules. *Nature*, 581(7809):396–400, May 2020.

[9] S. M. Udrescu, A. J. Brinson, R. F. Garcia Ruiz, K. Gaul, R. Berger, J. Billowes, C. L. Binnersley, M. L. Bissell, A. A. Breier, K. Chrysalidis, et al. Isotope shifts of radium monofluoride molecules. *Physical Review Letters*, 127(3), July 2021.

[10] S. G. Wilkins, S. M. Udrescu, M. Athanasakis-Kaklamanakis, R. F. Garcia Ruiz, M. Au, I. Belošević, R. Berger, M. L. Bissell, A. A. Breier, A. J. Brinson, et al. Observation of the distribution of nuclear magnetization in a molecule, November 2023. arXiv:2311.04121.

[11] S. M. Udrescu, S. G. Wilkins, A. A. Breier, M. Athanasakis-Kaklamanakis, R. F. Garcia Ruiz, M. Au, I. Belošević, R. Berger, M. L. Bissell, C. L. Binnersley, et al. Precision spectroscopy and laser-cooling scheme of a radium-containing molecule. *Nature Physics*, 20(2):202–207, January 2024.

[12] M. Athanasakis-Kaklamanakis, S. G. Wilkins, L. V. Skripnikov, Á. Koszorús, A. A. Breier, O. Ahmad, M. Au, S. W. Bai, I. Belošević, J. Berbalk, et al. Electron correlation and relativistic effects in the excited states of radium monofluoride. *Nature Communications*, 16(1), March 2025.

[13] R. G. Cooks. *Collision Spectroscopy*. Springer, Cham, 1978.

[14] Peter Atkins and Ronald Friedman. *Molecular Quantum Mechanics*. Oxford University Press, Oxford, 2005.

[15] Bin Shao. A crash course in quantum mechanics. https://www.binshao.info/download/tutorials/QM101.pdf, 2020. Accessed: 2025-05-01.

[16] Gordon W. F. Drake. *Springer Handbook of Atomic, Molecular, and Optical Physics*. Springer, 2023.

[17] John R. Taylor. *Scattering theory: The quantum theory of nonrelativistic collisions*. Dover Publications, 2012.

[18] B H Bransden. The theory of charge exchange. *Reports on Progress in Physics*, 35(3):949–1005, Sep 1972.

[19] Georgia State University. Elastic and inelastic collisions. http://hyperphysics.phy-astr.gsu.edu/hbase/elacol.html, 2025. Accessed: 2025-05-03.

[20] Bradford Morris. Charge-exchange collision dynamics and ion engine grid geometry optimization. *Caltech*, 01 2007.

[21] Guodong Zhang, Dandan Lu, Min Cheng, Hua Guo, and Hong Gao. Frustrated charge transfer in vibrationally inelastic $Ar^+ + N_2$ collisions via hard collision glory scattering. *Nature Communications*, 15(1), September 2024.

[22] K. B. McAfee, C. R. Szmanda, R. S. Hozack, and R. E. Johnson. Dynamics of energy transfer during charge-exchange in symmetric diatomic systems. *The Journal of Chemical Physics*, 77(5):2399–2407, September 1982.

[23] Martin Quack. Detailed symmetry selection rules for reactive collisions. *Molecular Physics*, 34(2):477–504, August 1977.

[24] Ingolf V. Hertel and Claus-Peter Schulz. *Atoms, molecules and optical physics 1. Atoms and spectroscopy*. Springer, 2015.

[25] Y. J. Wu, G. S. Khandelwal, and J. W. Wilson. Charge exchange transition probability for collisions between unlike ions and atom within the adiabatic approximation. Technical Report NASA-TM-101559, NASA Technical Memorandum, 1989.

[26] Andrew Fischer. Why go beyond Ehrenfest? Two-way energy transfer between electrons and ions. http://indico.ictp.it/event/a10164/session/37/contribution/24/material/0/0.pdf, 2010. ICTP presentation.

[27] MIT OpenCourseWare. Lecture #32: Adiabatic to diabatic – Zewail. https://ocw.mit.edu/courses/5-61-physical-chemistry-fall-2017/94b714be5ebb962ffbe5e3ecc9ea150e_MIT5_61F17_lec32.pdf, 2017. Accessed: 2025-05-03.

[28] Kenta Higuchi and Takuya Watanabe. Two-level adiabatic transition probability for small avoided crossings generated by tangential intersections, May 2024.

[29] Hans Paetz gen Schieck. *Nuclear Reactions: An Introduction*. Springer, Heidelberg, 2014.

[30] B. D. Simons. Scattering theory lecture notes (advanced quantum physics), 2021. University of Cambridge, TCM Group.

[31] Stephen T. Thornton. *Modern Physics for Scientists and Engineers*. Cengage Publishing, 4th edition, 2012.

[32] CERN-ISOLDE. Isolde targets and separators. https://isolde.cern/targets-and-separators, 2025. Accessed: 2025-05-03.

[33] M. Au, M. Athanasakis-Kaklamanakis, L. Nies, J. Ballof, R. Berger, K. Chrysalidis, P. Fischer, R. Heinke, J. Johnson, U. Köster, et al. In-source and in-trap formation of molecular ions in the actinide mass range at CERN-ISOLDE. *Nuclear Instruments and Methods in Physics Research Section B: Beam Interactions with Materials and Atoms*, 541:375–379, August 2023.

[34] R. Catherall, W. Andreazza, M. Breitenfeldt, A. Dorsival, G. J. Focker, T. P. Gharsa, T. J. Giles, J.-L. Grenard, F. Locci, P. Martins, et al. The ISOLDE facility. *Journal of Physics G: Nuclear and Particle Physics*, 44(9):094002, August 2017.

[35] Ivan Podadera-Aliseda. *New Developments on Preparation of Cooled and Bunched Radioactive Ion Beams at ISOL Facilities: The ISCOOL Project and the Rotating Wall Cooling*. PhD thesis, Universitat Politècnica de Catalunya, 2006.

[36] CERN-ISOLDE. CRIS: Collinear resonance ionisation spectroscopy. https://isolde.web.cern.ch/cris, 2025. Accessed: 2025-05-03.

[37] P. Campbell, I.D. Moore, and M.R. Pearson. Laser spectroscopy for nuclear structure physics. *Progress in Particle and Nuclear Physics*, 86:127–180, Jan 2016.

[38] A. R. Vernon, R. P. de Groote, J. Billowes, C. L. Binnersley, T. E. Cocolios, G. J. Farooq-Smith, K. T. Flanagan, R. F. Garcia Ruiz, W. Gins, A. Koszorús, et al. Optimising the collinear resonance ionisation spectroscopy (CRIS) experiment at CERN-ISOLDE. *Nuclear Instruments and Methods in Physics Research Section B: Beam Interactions with Materials and Atoms*, 463:384–389, January 2020.

[39] Jessica Warbinek. Study of RaF^- anions at CRIS. Presentation at the CRIS Collaboration Meeting, 2025. Accessed May 2025.

[40] S. G. Wilkins, H. A. Perrett, S. M. Udrescu, A. A. Kyuberis, L. F. Pašteka, M. Au, I. Belošević, R. Berger, C. L. Binnersley, M. L. Bissell, et al. Ionization potential of radium monofluoride. https://arxiv.org/abs/2408.14673, October 2024. arXiv:2408.14673.

[41] Timur Isaev, Steven Hoekstra, Lorenz Willmann, and Robert Berger. Ion neutralisation mass-spectrometry route to radium monofluoride (RaF). *arXiv: Chemical Physics*, 2013.

[42] M. Nichols, M. Athanasakis-Kaklamanakis, A. Borschevsky, T. E. Cocolios, R. Crosa-Rossa, R. P. de Groote, K. T. Flanagan, R. F. Garcia Ruiz, S. Geldhof, D. Hanstorp, et al. Investigating radioactive negative ion production via double electron capture. *Nuclear Instruments and Methods in Physics Research Section B: Beam Interactions with Materials and Atoms*, 541:264–267, August 2023.

[43] Mehdi Hamamda, Pierre Pillet, Hans Lignier, and Daniel Comparat. Universal deceleration of highly polar molecules. *New Journal of Physics*, 17(4):045018, Apr 2015.

[44] T. A. Isaev, S. Hoekstra, and R. Berger. Laser-cooled RaF as a promising candidate to measure molecular parity violation. *Physical Review A*, 82(5), Nov 2010.

[45] National Institute of Standards and Technology. Atomic data for sodium (Na). https://physics.nist.gov/PhysRefData/Handbook/Tables/sodiumtable1_a.htm, 2023. Accessed: 2025-05-05.

[46] Konstantin Gaul and Robert Berger. Toolbox approach for quasi-relativistic calculation of molecular properties for precision tests of fundamental physics. *The Journal of Chemical Physics*, 152(4):044101, January 2020.

[47] R. K. Janev and J. W. Gallagher. Evaluated theoretical cross-section data for charge exchange of multiply charged ions with atoms. III. Nonhydrogenic target atoms. *Journal of Physical and Chemical Reference Data*, 13(4):1199–1249, Oct 1984.

[48] B. H. Bransden and M. R. C. McDowell. *Charge Exchange and the theory of ion-atom collisions*. Clarendon, 2023.

[49] D.P. Almeida and M.L. Langford. Double electron capture in a Landau—zener model: A reaction window. *International Journal of Mass Spectrometry and Ion Processes*, 96(3):331–339, Apr 1990.

[50] A. Lépine-Szily and R. Lichtenthäler. Coupled channels effects in heavy ion reactions. *The European Physical Journal A*, 57(3), Mar 2021.

[51] Inga Yu. Tolstikhina, M. Imai, and V.P. Shevelko. Mechanisms of non-adiabatic charge-exchange transitions in slow collisions of w ions with he, ar and kr atoms. *Nuclear Instruments and Methods in Physics Research Section B: Beam Interactions with Materials and Atoms*, 535:241–246, Feb 2023.

[52] J. F. Harrison, R. W. Field, and C. C. Jarrold. Comparison of CaF, ZnF, CaO, and ZnO: Their anions and cations in their ground and low-lying excited states. *ACS Symposium Series*, page 238–259, Aug 2002.

[53] Hans-Joachim Werner, Peter J. Knowles, Gerald Knizia, Frederick R. Manby, and Martin Schütz. Molpro: A general-purpose quantum chemistry program package. *WIREs Computational Molecular Science*, 2(2):242–253, Jul 2011.

[54] David Feller. The role of databases in support of computational chemistry calculations. *J. Comput. Chem.*, 17:1571–1586, 1996.

[55] Karen L. Schuchardt, Brett T. Didier, Todd Elsethagen, Lisong Sun, Vidhya Gurumoorthi, Jared Chase, Jun Li, and Theresa L. Windus. Basis set exchange: A community database for computational sciences. *J. Chem. Inf. Model.*, 47:1045–1052, 2007.

[56] Renu Bala, H S Nataraj, and Malaya K Nayak. Ab initio calculations of permanent dipole moments and dipole polarizabilities of alkaline-earth monofluorides. *Journal of Physics B: Atomic, Molecular and Optical Physics*, 52(8):085101, mar 2019.

[57] J. M. de Wit. Calculated polarizabilities of baf, srf and caf using the relativistic finite-field fock-space coupled cluster method. Master's thesis, University of Groningen, 2018.

[58] NIST Computational Chemistry Comparison and Benchmark Database. List of experimental polarizabilities. https://cccbdb.nist.gov/pollistx.asp, 2025. Accessed: 2025-04-29.

[59] NIST. Calculated polarizability. https://www.nist.gov/, 2025. Accessed May 2025.

[60] J. Loreau. Simple models. *Chemistry in Motion*, lecture notes. Retrieved from https://toledo.kuleuven.be/.

[61] Manjeera Mantina, Adam C. Chamberlin, Rosendo Valero, Christopher J. Cramer, and Donald G. Truhlar. Consistent van der waals radii for the whole main group. *The Journal of Physical Chemistry A*, 113(19):5806–5812, Apr 2009.

[62] Austin M. Mroz, Audrey M. Davenport, Jasper Sterling, Joshua Davis, and Christopher H. Hendon. An electric field-based approach for quantifying effective volumes and radii of chemically affected space. *Chemical Science*, 13(22):6558–6566, 2022.

[63] Austin-Mroz. Austin-Mroz/Streusel: Surface topology recovery using sampling of electric field – calculate i) atomic/molecular volumes, ii) pore volumes and surface areas of porous materials, and iii) interaction energies.

[64] F. Neese. The orca program system. *WIRES Comput. Molec. Sci.*, 2(1):73–78, 2012.

[65] Marius Retegan. Create a .cube file of the molecular electrostatic potential using orca., 2022.

[66] Paul Langevin. Une formule fondamentale de théorie cinétique. *Annales de Chimie et de Physique, 5^e série*, 5:245–288, 1905.

[67] Daniela Ascenzi, Andrea Cernuto, Nadia Balucani, Paolo Tosi, Cecilia Ceccarelli, Luca Matteo Martini, and Fernando Pirani. Destruction of dimethyl ether and methyl formate by collisions with he+. *Astronomy Astrophysics*, 625, May 2019.

[68] Timothy Su, Elkie C.F. Su, and Michael T. Bowers. Theory of ion—molecule collisions: Effect of the induced dipole—induced dipole potential on ion—molecule capture rate constants. *International Journal of Mass Spectrometry and Ion Physics*, 28(3):285–288, Nov 1978.

[69] Thomas F. Moran and William H. Hamill. Cross sections of ion-permanent-dipole reactions by mass spectrometry. *The Journal of Chemical Physics*, 39(6):1413–1422, Sep 1963.

[70] Timothy Su and Michael T. Bowers. Theory of ion-polar molecule collisions. comparison with experimental charge transfer reactions of rare gas ions to geometric isomers of difluorobenzene and dichloroethylene. *The Journal of Chemical Physics*, 58(7):3027–3037, Apr 1973.

[71] L. Bass, T. Su, W.J. Chesnavich, and M.T. Bowers. Ion-polar molecule collisions. a modification of the average dipole orientation theory: The cos model. *Chemical Physics Letters*, 34(1):119–122, 1975.

[72] Timothy Su, Elkie C. Su, and Michael T. Bowers. Ion–polar molecule collisions. conservation of angular momentum in the average dipole orientation theory. the aado theory. *The Journal of Chemical Physics*, 69(5):2243–2250, Sep 1978.

[73] Timothy Su and Michael T. Bowers. Parameterization of the average dipole orientation theory: Temperature dependence. *International Journal of Mass Spectrometry and Ion Physics*, 17(2):211–212, Jun 1975.

[74] Winifred M. Huo, Yen Liu, Marco Panesi, Alessandro Munafo, Alan Wray, and Duane F. Carbon. Electron-impact excitation cross sections for modeling non-equilibrium gas. In *SciTech 2015*, Kissimmee, FL, USA, January 2015. NASA Ames Research Center. NASA Technical Memorandum ARC-E-DAA-TN20304.

[75] M. M. Hubers. *Ion pair formation in atom-molecule collisions*. PhD thesis, University of Amsterdam, 1976.

[76] A W Kleyn and A M Moutinho. Negative ion formation in alkali-atom-molecule collisions. *Journal of Physics B: Atomic, Molecular and Optical Physics*, 34(14), Jul 2001.

[77] M.M. Hubers, A.W. Kleyn, and J. Los. Ion pair formation in alkali-halogen collisions at high velocities. *Chemical Physics*, 17(3):303–325, Nov 1976.

[78] Xinxuan Tang, Cuilian Ding, Shiqi Yu, Cheng Zhong, Hang Luo, and Sheng Chen. Mechanism study of molecular trap in all-organic polystyrene-based dielectric composite. *Small*, 20(22), Dec 2023.

[79] Mineo Kimura. Negative-ion formation and mutual neutralization in atom–atom and ion–ion collisions below Kev energies. *Applied Surface Science*, 253(16):6641–6645, Jun 2007.

[80] Adam Kirrander, Seth Rittenhouse, Marco Ascoli, Edward E. Eyler, Phillip L. Gould, and H. R. Sadeghpour. Approach to form long-range ion-pair molecules in an ultracold Rb gas. *Physical Review A*, 87(3), Mar 2013.

[81] Madelyn Smith, Richa Khatiwada, and Pengfei Li. Exploring ion polarizabilities and their correlation with van der Waals radii: A theoretical investigation. *Journal of Chemical Theory and Computation*, 20(19):8505–8516, Sep 2024.

[82] H. S. W. Massey. Collisions between atoms and molecules at ordinary temperatures. *Reports on Progress in Physics*, 12(1):248, 1949.

[83] Ya M Fogel, R V Mitin, V F Kozlov, and N D Romashko. On applicability of Massey's adiabatic hypothesis to double charge exchange processes. *Zhur. Eksptl'. i Teoret. Fiz.*, Vol: 35, 01 1958.

[84] Gerald D. Alton. Negative-ion formation processes and sources. In Ragnar Hellborg, editor, *Electrostatic Accelerators*, Particle Acceleration and Detection, pages 241–282. Springer, Berlin, Heidelberg, 2005.

[85] L Vermeeren, P Lievens, A Buekenhoudt, and R E Silverans. Charge exchange collisions between alkaline-earth ions and alkali atoms. *Journal of Physics B: Atomic, Molecular and Optical Physics*, 25(5):1009–1019, Mar 1992.

[86] C. B. Alcock, V. P. Itkin, and M. K. Horrigan and. Vapour pressure equations for the metallic elements: 298–2500k. *Canadian Metallurgical Quarterly*, 23(3):309–313, 1984.

[87] Gianni Di Domenico and Antoine Weis. Vapor pressure and density of alkali metals. https://demonstrations.wolfram.com/VaporPressureAndDensityOfAlkaliMetals/, 2011. Wolfram Demonstrations Project.

[88] K. McCormick. *The charge-exchange cell for the neutral lithium beam probe on Pulsator, W7A and ASDEX*. Max-Plank-Institut fur Plasmaphysik, 1983.

[89] OpenAI. ChatGPT:(gpt-4o), 2025. Accessed May 26, 2025. Large language model (GPT-4o) developed by OpenAI.

Appendices

Appendix A

First appendix

A.1 Time-of-Flight

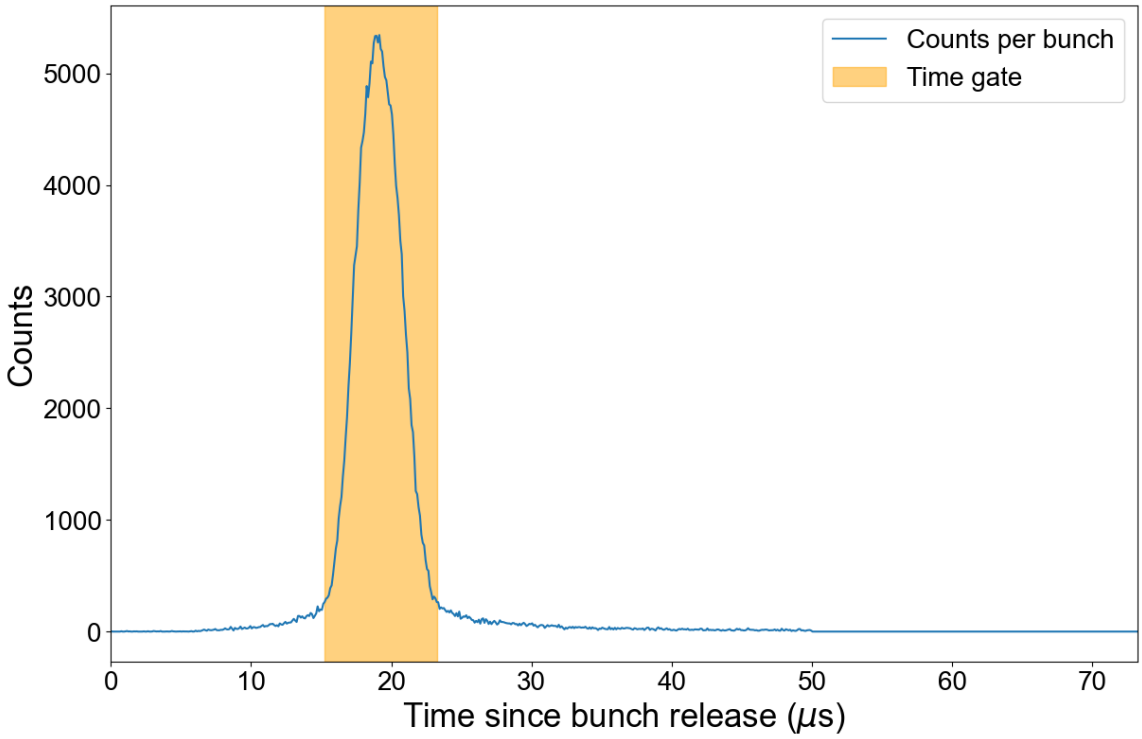

Figure A.1: Time-of-flight (TOF) profile for Scan 3130, the scan in which the experimental results pertain to. The yellow region marks the ion counts that correspond to a peak in time since the bunch was released from ISCOOL.

Appendix B

Second appendix: Calculations for the first Charge Exchange of CaF^+ with Na

B.1 Potential Energy Surface Difference between States

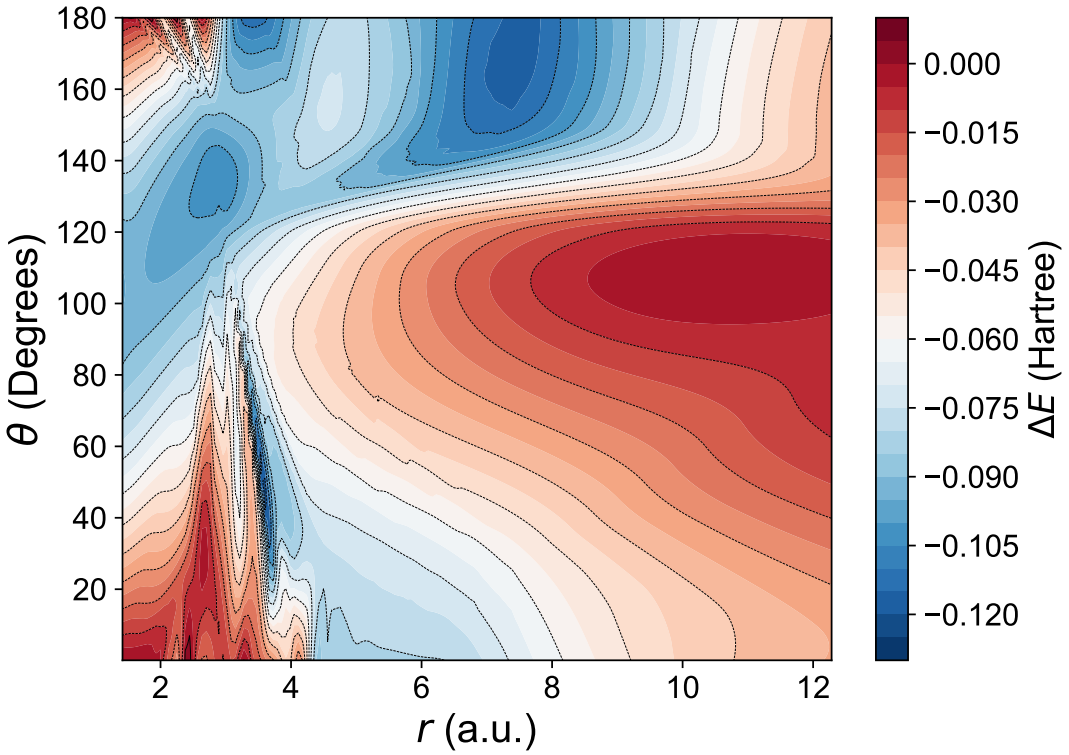

Figure B.1: Contour plot of the potential energy surface (PES) difference between states 1 and 2. State 1 corresponds to CaF + Na^+, and state 2 is CaF^+ + Na. Energies were computed using CASSCF in Molpro with a 6-31+G* basis set. The active space consists of 11 orbitals with 5 orbitals frozen, and the equilibrium bond length was fixed using the value of CaF^+.

B.2 Potential Energy Curve at 180 Degrees

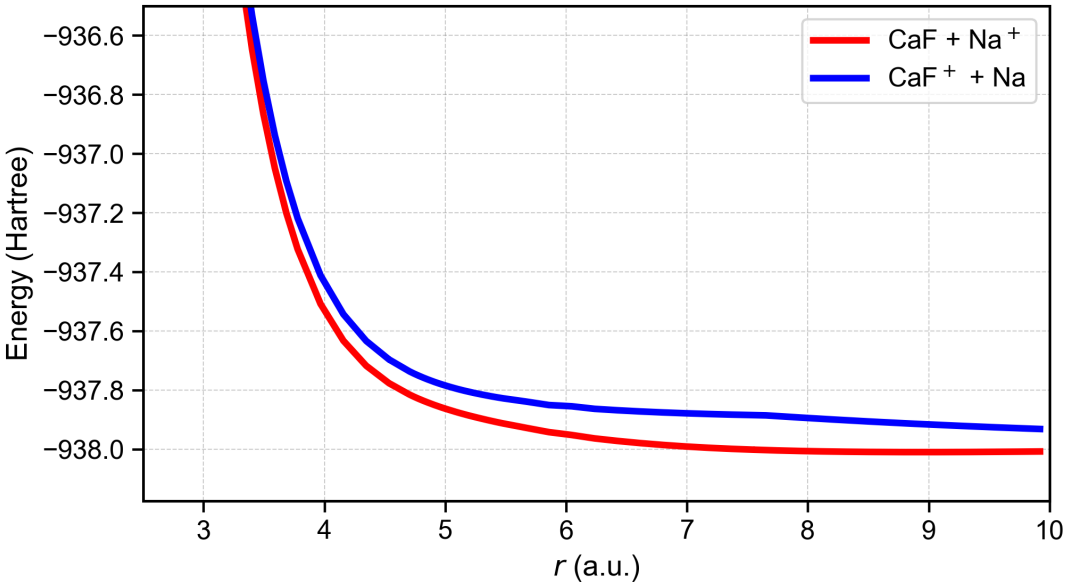

Figure B.2: Potential energy curves for the CaF + Na^+ (state 1, red) and CaF^+ + Na (state 2, blue) channels as a function of intermolecular center of mass (COM) distance at $\theta = 180°$. Energies were computed using CASSCF in Molpro with the 6-31+G* basis set. The active space consists of 11 orbitals, with 5 frozen, and the Ca–F bond length was fixed to the equilibrium geometry of CaF^+.

B.3 Mulliken Population of CaF Species at 180 Degrees

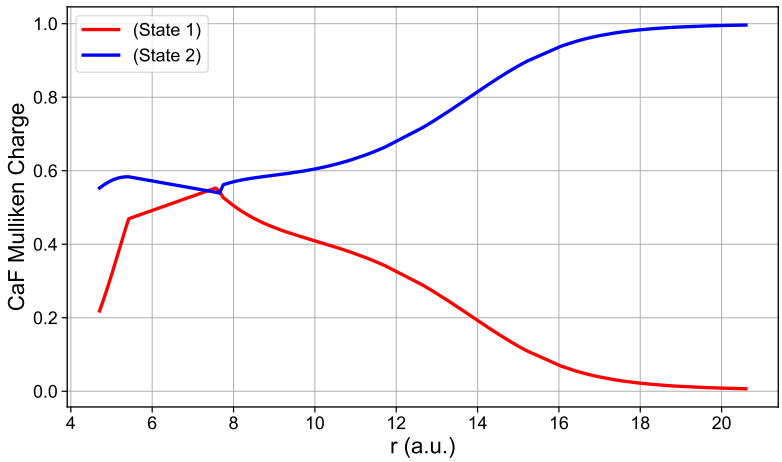

Figure B.3: Mulliken population analysis illustrating charge transfer behavior in the CaF^+ + Na system at $\theta = 180°$. The plot tracks the Mulliken charge on the CaF species as a function of COM distance in a.u. for the two electronic states. As shown by the charge at large distances, state 1 corresponds to the neutral channel (CaF + Na^+), while state 2 the channel after charge exchange. The charges intersect around 6.50 a.u., suggesting charge exchange occurs prior to this point. Energies and populations were computed using CASSCF in Molpro with a 6-31+G* basis set and a fixed Ca–F bond length at the equilibrium geometry of CaF^+.

Appendix C

Third appendix: Gen AI

Due to the time sensitivity of this project, generative AI was used to troubleshoot any code problems [89]. It was also used for aesthetic purposes in generating figures. The paper stating this, along with the model used is attached on the following page per the request of the thesis coordinator for the Department of Chemistry at KU Leuven.

Complete this form and include it in your master thesis if you made use of generative artificial intelligence (GenAI)

Specify which AI you used (e.g. ChatGPT/GPT4/...):

GPT-4o

Please indicate with "X" (possibly multiple times) in which way you were using it:

O **Assistance with the language of a text**

Code of conduct: This use is similar to using a spell checker. It also includes the use of predictive keyboards and tools like “Smart Compose” in google docs.

O **As a search engine to learn about a particular topic**

Code of conduct: This use is similar to, for example, a google search or checking Wikipedia. Be aware that the output of chatbots evolves and may change over time.

O **For a literature search**

Code of conduct: This use is comparable to, for example, a google scholar search. However, be aware that ChatGPT may output no or wrong references. As a student you are responsible for further checking and verifying the absence or correctness of references.

Ø **To let it generate programming code**

Correctly mention the use of GenAI and cite it. Note you can ask the AI how to cite it.

O **To let it generate new research ideas**

Code of conduct: Further verify in this case whether the idea is novel or not. It is likely that it is related to existing work, which should be referenced then.

O **To let it generate blocks of text**

Code of conduct: Inserting AI-generated blocks of text without quotes into the thesis **is not allowed**. According to Article 84 of the exam regulations in evaluating your work one should be able to correctly judge on your own knowledge. In case it is really needed to insert a block of AI-generated text, mention it as a citation by using quotes. **But this should be kept to an absolute minimum.**

O **Other**

Code of conduct: Contact the promotor and the master thesis coordinator. Motivate how you comply with Article 84 of the exam regulations. Explain the use and the added value of using an AI tool:

Nuclear and Radiation Physics
Celestijnenlaan 200d - bus 2418
B-3001 Heverlee, BELGIË
tel. + 32 16 32 76 80
gerda.neyens@kuleuven.be
www.kuleuven.be